Electrochemical and Spectroscopic Studies of Phospholipid Bilayers Supported on Au(111) Electrodes

by

Elena Madrid

A thesis submitted to
The University of Birmingham
For the degree of
DOCTOR OF PHYLOSOPHY

School of Chemistry
College of Engineering and Physical Sciences
The University of Birmingham
September 2011

ABSTRACT

Electrochemistry and polarization modulation infrared reflection absorption spectroscopy (PM-IRRAS) measurements were used to characterize the structure and organization of a mimetic biological membrane supported at a Au(111) electrode surface to determine the influence of molecule structure on ensemble properties.

Creation and deposition of mimetic membranes was carried out by combining Langmuir-Blodgett / Langmuir-Schaefer (LBLS) techniques. The LB-LS methodology allows the building of symmetric bilayers and more realistic systems based on a mixture of phospholipids that can be asymmetrically distributed across the bilayer.
The phospholipids that have been studied in this work are DMPC, DMPE and DMPS. They differ from each other in the headgroup. However, they are all symmetric lipids with two saturated acyl chains of 14 carbon atoms.

The electrochemical techniques have characterized the permeability of the film and have detected phase transitions of the lipids at the electrode. PM-IRRAS has provided information regarding the phase state, orientation of phospholipid acyl chains and degree of hydrogen bonding of the headgroup and glycerol region as the applied field was varied.

Results have shown that DMPE bilayers contain less solvent content than DMPC and DMPS bilayers. DMPE molecules packed more tightly due to the hydrogen bonding network between the phosphate and the ammonium group of the neighbouring DMPE molecules which hinder the bilayer from hydration. The hydrocarbon chain orientation was less tilted from the surface normal than that of DMPC but very similar to DMPS at adsorption potentials. During desorption, DMPS has increased hydration of the carbonyl groups and the acyl chains tilted, increasing the compactness between them. The headgroups of DMPS remain hydrated, which increases the capacity of the bilayer.

to my dearest parents

ACKNOWLEDGMENTS

First and foremost, I would like to express my sincere gratitude to my supervisor, Dr Sarah L. Horswell for giving me the opportunity to work within her research group and for her direction, support and encouragement throughout this research project. Without Sarah's guidance, the production of this thesis would not have been possible.

I have many people to express one's thanks to, I would like to start with my research group, especially Andrew for the development of critical software and Goy for her sincere friendship and support throughout the good and bad times.
I am also indebted to all those who I have shared time with over the past few years, without then it would have been harder to complete this work.

I would like to thank Stuart, Steve and Tony for all the technical support, they were always there for the little and not so little problems.

I would like to thank James Bowen, Cris Harling, Anna Walkiewicz for all their advice and training, with special thanks to Vlad Zamlynny for his help from overseas.

I would like to thank to Dr. Jim Tucker and Professor Richard Nichols for accepting being examiners of this work.

Finally I would like to sincerely thank my family and friends who from far away, always were felt very close. My warmest and sincerest thanks to my boyfriend Danny, for all his love, support, understanding and patience.

TABLE OF CONTENTS

CHAPTER 1: INTRODUCTION

1.1 Preface

All living creatures are made of cells and every cell contains specialized structures surrounded by a limiting and selectively permeable biological membrane. These structures play a crucial role in almost all the cellular biochemistry by regulating the entry and exit of specific molecules and ions, transfer information and aid in energy storage [1, 2]. The functions of a cell membrane are very diverse and are determined by the physical properties of the individual lipids and proteins. In order to understand many important biological processes, it is necessary to have a complete description of the organization and dynamics of such membranes [3].

The cell membrane is characterized by its fundamental structure, the lipid bilayer. This bilayer configuration was first deducted by Gorter and Grendel in 1925 [4] and was improved by Singer and Nicolson in 1972, who proposed a fluid mosaic model for the gross structure of proteins and lipids in biological membranes in which proteins are integrated or partially embedded in a complex matrix of lipids [5]. The major difficulty in the study of biological membranes arises from this extreme complexity, thus simple models based on lipid bilayer structures have been used for a long time to provide relevant information of specific membranes or processes [6].

In this chapter an overview of the membrane structure will introduce some important aspects of the bilayers formed by phospholipids. Secondly, a description of the different techniques used for the creation of lipid bilayers on solid substrates is given. An introduction of the concept of the electric field across the membrane leads to a description of how this can be manipulated and reproduced using solid electrodes as substrates for the bilayer deposition. At the end of this chapter a brief description of some techniques that allow the study of the organization and characterization of lipid bilayers as biomimetic membranes are mentioned.

1.2 Components of Cell Membranes

The fundamental construction unit of all biological membranes is the lipid bilayer. Lipids present in membranes are very diverse in quantity, function and shape. Some lipids play an important role in enabling more stable packing while others, perform regulatory and biosynthetic functions. Despite these differences, all

lipids have something in common: they are amphipathic molecules; that is, they have a polar (hydrophilic) headgroup and apolar (hydrophobic) tail. All lipids go through a self assembly structure in an aqueous solution; this is the result of the hydrophobic effect, whereby the hydrophobic tail tends to be squeezed away from the aqueous phase to expose hydrophilic "head" regions [2]. Some of the different structures that the phospholipids can form in aqueous solutions are shown in Figure 1.1.

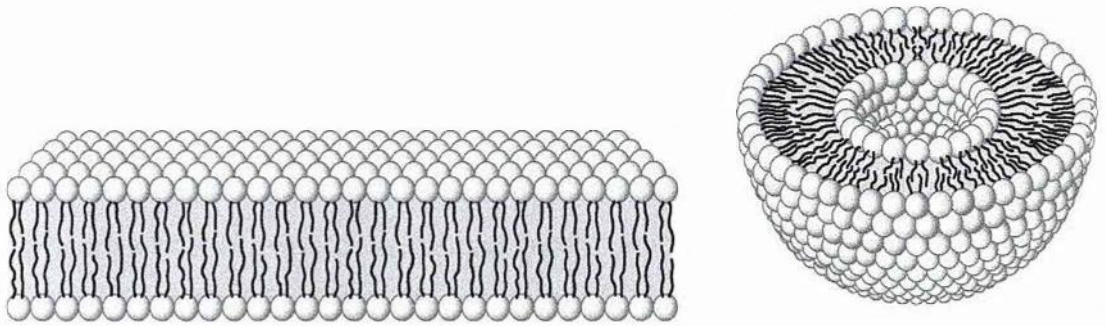

Figure 1.1: Cross-sectional view of two structures formed by lipids in polar solutions [2].

A typical biomembrane is composed of three primary lipid components: phosphoglycerides or phospholipids, sphingolipids and steroids.

Although different cellular membranes vary in lipid composition, phospholipids are the most abundant class of lipids in most membranes. There exist more then 100 phospholipids that are different in their polar headgroups and the composition of their hydrophobic chains. A typical phospholipid molecule (Figure 1.2) consists of a hydrophobic tail composed of two fatty acyl chains esterified to the two hydroxyl groups in glycerol phosphate (glycerol backbone), in the positions *sn1*- and *sn2*- and a polar headgroup attached to the phosphate group such as ethanolamine, serine, choline or glycerol.

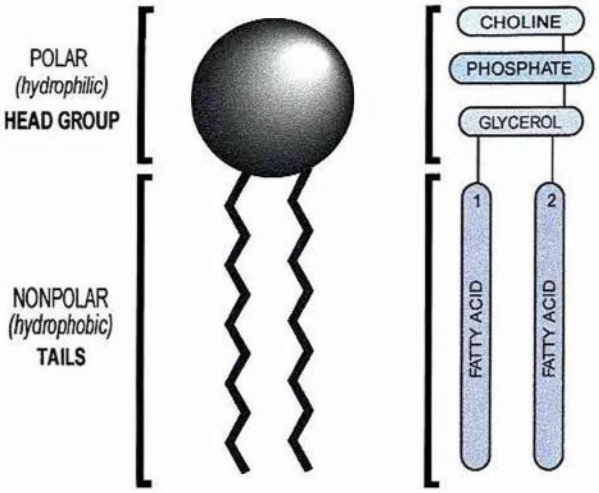

Figure 1.2: Schematic representation and structure of a PC phospholipid.

The four most abundant classes of lipids in animal cell membranes are phosphatidylcholine (PC), phosphatidylethanolamine (PE) and phosphatidylserine (PS) and sphingomyelins (SM). Some examples of these phospholipids are shown in Figure 1.3. These examples consist of two 14-carbon saturated acyl chains, a glycerol backbone and negatively charged phosphate group to which the specific group is bound.

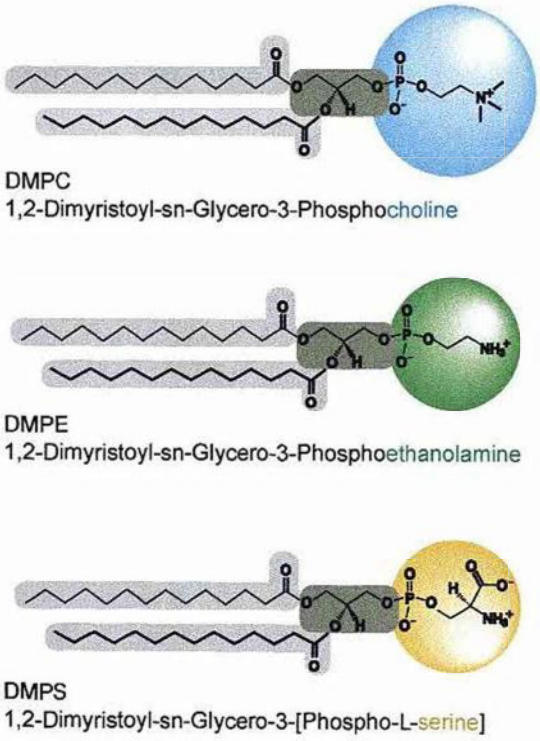

Figure 1.3: Lipid structure for DMPC, DMPE and DMPS.

Phosphatidylcholine is the most common headgroup of the lipid molecules that forms the plasma membrane. PC headgroups are zwitterionic, with negatively charged phosphate and positively charged choline moieties. Because PC headgroups are the most numerous on the plasma membranes, model membranes are commonly constructed solely of PC lipids without any other molecules.

Another major phospholipid is PE, which has a zwitterionic headgroup with an ethanolamine as its moiety. Because the volume of the PE headgroup is 30% smaller than PC, bilayers formed by PE are more rigid and more laterally compressed than those of PC [7]. Many phosphatidylethanolamines are cone-shaped, (Figure 1.4) which means that they are usually located in the inner leaflet of the cell membrane.

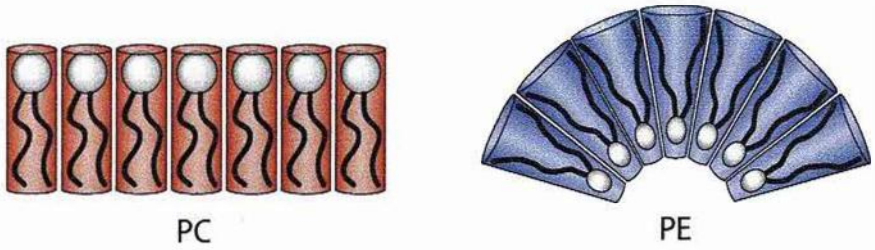

Figure 1.4: Cylindrical and Cone shaped phospholipids [2].

In mitochondrial membranes, PC and PE are also the major phospholipids present [8]. There is also a special type of phospholipid which is mainly present in mitochondria membranes; the four-chains lipid, cardiolipin (CL).

CL is a quadruple-chained anionic amphiphile composed of two 1, 2-diacyl phosphatidate moieties esterified to the *sn1*- and *sn3*- hydroxyl groups of a single glycerol molecule. The CL polar headgroup contains two phosphodiester moieties, which are negatively charged under physiologically relevant conditions [9]. Another important phospholipid, which is negatively charged, is PS. The charge held by these lipids plays an important role, triggering the cell activity. These phospholipids require further study due to the lack of information concerning phospholipids with negatively charged headgroups.

One of the most unusual changes in the surface of plasma membranes that is not fully understood is the translocation of PS and CL, from their normal location on the inner plasma membranes to the outer [10]. This translocation appears to occur in

apoptosis. Some studies using pulsed electric fields have demonstrated that the externalization of PS can be forced [11, 12].

The complex cell processes require substantial differences between the inner and outer membrane leaflets, thus the distribution of the lipids in biological membranes is highly asymmetric. Membrane structural properties depend critically on this asymmetric distribution and, at the same time, in the asymmetry between headgroup moieties and acyl chains of the different phospholipids.

Phospholipid acyl chains undergo a characteristic phase transition when the temperature increases. The temperature at which the main phase transition takes place is denoted as T_m and is different for each phospholipid. These phase transitions are due to the increase in the motion of the C-C bonds. The lowest rotational energy is attributed to *trans* conformation (anti-periplanar) where the acyl chain are fully extended and closely packed. When most of the chains have all-*trans* conformation, the state is known as the gel phase [13]. As the temperature increases, the rotation around C–C bonds of an angle ±112° forms *gauche* (anti-clinal) conformations, increasing the randomness and fluidity of the bilayer. This phase is called a liquid crystalline phase. When an acyl chain has gauche conformers and there is at least one trans bond between them then such a configuration is labelled as kink [14]. At usual physiological temperatures, the hydrophobic interior of natural membranes generally has a low viscosity and a fluid like consistency allowing the lipids to diffuse laterally for a better interaction with molecules.

1.3 Formation of Supported Lipid Bilayers

There have been several different methods employed for the preparation of supported lipid bilayers onto solid substrates. The first method involves the creation of vesicles, usually by ultrasonic irradiation of a phospholipid solution [15, 16]. These vesicles adsorb to the substrate surface where they open and fuse to form the lipid bilayer. The second method uses the Langmuir-Blodgett and/or Langmuir Schaefer techniques. These techniques are based on the double deposition of a compact monolayer formed at the gas/liquid interface onto a solid substrate [17]. The first leaflet is transferred by pulling a substrate through the gas/liquid interface in a Langmuir trough on which a lipid monolayer is spread. The second leaflet is deposited by

pushing the substrate coated with the first leaflet, vertically or horizontally (Langmuir-Schaefer deposition) through the gas/liquid interface [18, 19]. The combination of the Langmuir-Blodgett and the Langmuir-Schaefer techniques was found to be the best strategy to deposit lipid bilayers onto solid substrates, allowing better control of the bilayer structure [20].

Other techniques such as spin coating [21] or the formation of a covalent linkage between the self-assembled molecules and the solid support are also used [22, 23]. In the case of non covalent bonds, the adsorption of the phospholipids onto the gold has the character of a weak chemisorption involving overlap between molecular orbitals of the adsorbate, and electronic states in the metal [24].

1.4 Electric Field Across the Membrane

The lipid bilayer in biological membranes acts as a selective barrier that allows certain materials to pass through. A few gases such as O_2 and CO_2 and small uncharged molecules can diffuse across the membrane without requiring any energy. The transport of most molecules in or out requires the assistance of specialized membrane proteins. Plasma membranes contain channel proteins that allow the principal cellular ions to move through them at different rates down their concentration gradient. Ion gradients across membranes can be used to synthesize ATP, to drive the transmembrane movement of selected solutes, or, in nerve and muscle cells, to produce and transmit electrical signals [25].

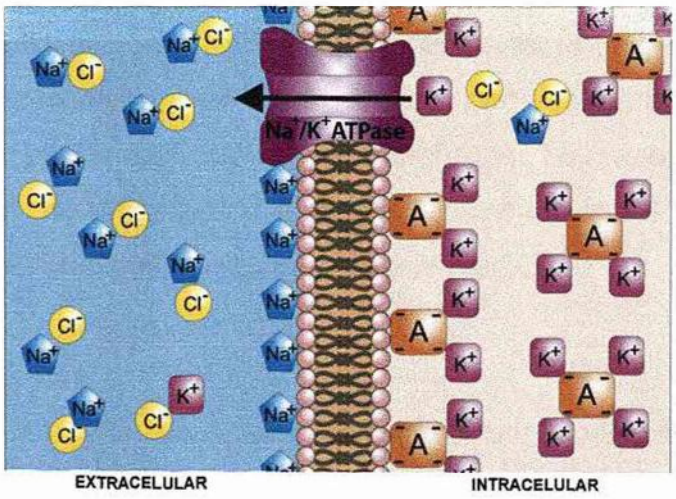

Figure 1.5: Ion concentration difference in plasma membrane [26].

An ionic difference between the inside of the cell from the surroundings creates a difference in the electrical charge on the two sides of the membrane, producing a voltage across the membrane (Figure 1.5). This voltage acts as a specific stimulus for the protein channels to open or close in response to it, allowing the ions to flow in or out of the cell (voltage-gated channels).

The most fundamental example of an ion channel is found in the plasma membrane of almost all animal cells; this is the protein known as Na^+/K^+ ATPase which pumps Na^+ ions from the inside of the cell to the outside, keeping the intracellular concentration of Na^+ low. Actively, the Na^+/K^+ ATPase pumps into the cell K^+ ions, which balances the charge carried by the cell's fixed anions. When the concentration of K^+ is high inside the cell and low outside, K^+ tends to leave the cell by its concentration gradient using the K^+ leak channels. The interior of the cell becomes negatively charged as K^+ moves out, creating an electrical field, which balances net efflux of K^+. The electrical potential across the membrane in plants, fungi and mitochondria is generated by electrogenic H^+ pumps, which generate most of the electrical potential.

The Nernst equation makes it possible to predict the theoretical voltage across the membrane, if the ratio of internal and external ion concentrations is known. The magnitude of the electric field across the biological cell membranes is of the order of 10^7 to 10^8 V m^{-1} [27]. These very high fields are a consequence of applying very modest potential differences (10-100 mV) over very small distances (bilayer thickness). The electric field experienced in biological membranes can be mimicked by supporting the bilayers on an electrode surface and varying the applied electric potential. This methodology provides a better understanding of the structural rearrangement and permeability of the cell membrane. This approach constitutes a step in the study of the organization and dynamics of biological membranes with a potential application in biology, biotechnology and medicine [28, 29].

1.4.1 Electrodes

Many studies of films have been performed on phospholipids deposited on mercury electrodes by extruding the drop of mercury through a monolayer spread on the gas-solution interphase [30-32] or by vesicle fusion [33]. The first use of a

biomembrane model on a coated mercury electrode was proposed by Miller [34]; a modified version of this one by Nelson and Benton followed [35]. Mercury has an atomically smooth and free of defect surface that makes it the ideal electrode material for the study of the barrier properties and charge transfer across the film. Films deposited on mercury electrodes have shown a defect-free self-sealing structure that avoids the permeability of ions [36]. As a result of this, mercury electrodes have been extensively used as a support to study models of biological membranes. A disadvantage of these electrodes is their hydrophobic nature, which makes the lipids acyl chains orient themselves towards the metal surface to minimize their adsorption Gibbs energy, obtaining an inverted film which is not a very good model of a membrane. In addition, if further structural investigations are needed, such as spectroscopy or scanning probes microscopies, these cannot be done with a liquid electrode and for those cases solid metal electrodes seem the best electrodes to choose.

Metal electrodes such as Pt, Au, Ag, Cu, Ni or stainless steel have been employed to support lipid films. These metals are more hydrophilic than mercury and the minimum adsorption Gibbs energy is achieved when the headgroup of the lipid is turned toward the metal surface, the repulsion between the acyl chain and the solution is avoided by depositing a second lipid monolayer with the hydrocarbon tails in contact with those of the inner monolayer and, the polar heads turned toward the aqueous solution [31] . The most used metal electrode has been the gold single crystal electrode, Au(111). The (111) plane of a gold single crystal is energetically the most stable plane and the charge from an electric field distributes homogenously across the surface. The surface of the Au(111) is easily reconstructed due to the lateral movement of the atoms that minimize surface energy by annealing methods. The Au(111) reconstruction consists of a slight compression of the surface atoms by about 4% in one of the three <110> directions which causes characteristic parallel corrugation lines. The surface contains atomically flat (111) terraces as the one shown in Figure 1.6. Well prepared electrodes usually show a single reconstruction domain per terrace [37]. These terraces are atomically smooth and the steps between terraces are just monoatomic steps and they do not increase substantially the bilayer defects [38].

Figure 1.6: STM image showing the area around a monoatomic high step [37].

1.5 Techniques

A wide range of physical techniques has been used in order to understand the structure and organization of lipid bilayers. Some examples of these techniques are calorimetry [39], neutron [40, 41] and X-ray diffraction [42], atomic force microscopy [43, 44] and infrared spectroscopy.

FT-IR spectroscopy in particular has made significant contributions in this research area. This successful tool has been used for studying the orientation of molecules at a surface and the degree of order within the thin organic film. The use of polarization modulation infrared reflection-absorption spectroscopy (PM-IRRAS) has the advantage, over classical infrared spectroscopy, of direct high quality measurement of the absorbance of adsorbed species [45-47]. Infrared-active groups are often present in the headgroup, the interfacial, and in the hydrophobic regions of most lipid molecules. To determine the degree of ordering of the acyl chains, C-H stretching mode frequencies and bandwidth were studied, providing some information concerning the packing arrangement and mobility of the chains. If PM-IRRAS is studied in conjunction with electrochemical techniques, potential-controlled transformation of the tilt angle of the chains with respect to the surface can be determined by using the band intensities of the stretching and bending modes of the methyl groups [16, 48-50]. Bands in other regions of the PM-IRRA spectra such as the C=O stretching region and PO_2^-, are indicative of the degree of hydrogen bonding/hydration of the headgroup and the glycerol region [51].

Electrochemical techniques such as cyclic voltammetry, differential capacitance, chronocoulometry are also techniques that have increased their popularity for study

of biological systems and processes such as electroporation [28, 52], translocation [53] or proteins voltage-gate channels [54, 55]. These techniques are also used for the film development into electrochemical sensors [56].

1.6 Aims and Objectives

In order to study the function of proteins and barrier properties of the biological membranes, a knowledge of the basic structural framework of biological membranes is needed and therefore phospholipid bilayers.

The application of similar voltages to those measured in real cells are performed on phospholipid bilayers to study the effect of the static electric field on their orientation and conformation. This thesis integrates electrochemical methods and polarization modulation infrared reflection absorption spectroscopy (PM-IRRAS) to study potential-induced changes in structure, orientation and hydration of a model of a biological membrane supported on Au(111).

The main advantage of using PM-IRRAS is the direct measurement of the absorbance of adsorbed species. Bands of the generated spectra are easy to interpret and quantitatively analysed.

The phospholipids used in this thesis are DMPC, DMPE and DMPS (Figure 1.3). They have different headgroups which will provide information on how the packing and the hydration of the bilayer is influenced when a small headgroup ($-NH_3$ for a DMPE) is used in comparison with a bulky one ($-N(CH_3)_3$ for a DMPC). A negatively charged DMPS is used to monitor the strong influence of the electric field in the bilayer organization. The length of the acyl chains for these phospholipids is C14 for easy comparison, and because at room temperature they are in all-*trans* conformation, which allows the quantitative determination of the tilt angle.

The first part of this thesis characterizes the physical state of phospholipid bilayers using isotherms, spectroscopic ellipsometry and PM-IRRAS. The second part describes the use of electrochemical techniques to study symmetric, asymmetric and mixed bilayers on Au(111). In the third part, DMPE and DMPS bilayers are studied in-depth by *in situ* PM-IRRAS in which the position and bandwidth of C-H stretching bands will be used to describe the mobility of the chains. Band intensities in other regions of the PM-IRRA spectra (C=O and PO_2^-) are used to follow the

hydration/hydrogen bonding progress at the headgroups and the interface region at different electric potentials.

Lipkowski's group has extensively developed the use of PM-IRRAS and a brief review of their work is given below.

The first time that *in situ* PM-IRRAS was used to study the orientation and packing of supported molecules was in 2002, when Horswell *et al.* achieved the calculation of the tilt angles for DMPC vesicles in Au(111) by using the relative method. At this time, no corrections of the PEM response function were made [48]. The corrections of the measured PM-IRRAS signal for the PEM response function were introduced one year later by Zamlynny in the studies of potential-induced reorientations of a 4-pentadecyl pyridine film, where the absorbance of a Langmuir film deposited on gold was calculated for the first time. The simulated spectrum of randomly orientated molecules of 4-pentadecyl pyridine was calculated by measuring its optical constants. The tilt angle of the pentadecyl chain and the pyridine moiety were then determined using the absolute method [57]. The methodological foundations for posteriori studies of monolayers and bilayer by PM-IRRAS are based on this first work with 4-pentadecyl pyridine films.

Quantitative *in situ* PM-IRRAS has been employed since to investigate orientation and transformation created by an electric field on a monolayer and bilayer of different molecules, such as n-octadecanol [58, 59]. The use of this technique in biomimetic research has been a very powerful tool to study changes in models of biological membranes supported at metal electrodes. In bilayers created by DMPC vesicles fusion for example, the vesicle spread on electrode ($-0.4 < E < 0.4$ V) showed higher frequencies and broad bands, indicating that the bilayer is less ordered than at desorption potentials. The calculated tilt angle of the acyl chains in this region is ≈55° which decreases to ≈35° towards negative potentials. Bilayers deposited by LBLS method have reduced the chain tilt angle from ≈25° at adsorbate potentials to ≈17° at desorption potentials, indicating that the structure of the film, with higher packing densities is much better controlled using LBLS method [20].

In a short period of time, supported models have increased their complexity [60-62] and the scope of their applications, such as corrosion protection, opens up a new world of possibilities.

References:

1. P. N. Bartlett, *Bioelectrochemistry: Fundamentals, Experimental Techniques and Applications*, John Wiley and Sons, Chichester, 2008.

2. H. Lodish, A. Berk, P. Matsudaira, C. A. Kaiser, M. Krieger, M. P. Scott, S. L. Zipursky and J. Darnell., *Molecular Cell Biology*, W. H. Freeman, New York, 2000.

3. R. Lipowsky and E. Sackmann, *Structure and Dynamics of Membranes*, Elsevier, 1995.

4. E. Gorter and F. Grendel, *J. Exp. Med.*, 1925, **41**, 439-443.

5. S. J. Singer and G. L. Nicolson, *Science*, 1972, **175**, 720-731.

6. H. T. Tien and A. L. Ottova, *J. Membr. Sci.*, 2001, **189**, 83-117.

7. H. I. Petrache, S. Tristram-Nagle, K. Gawrisch, D. Harries, V. A. Parsegian and J. F. Nagle, *Biophys. J.*, 2004, **86**, 1574-1586.

8. G. Daum and J. E. Vance, *Prog. Lipid Res.*, 1997, **36**, 103-130.

9. R. N. A. H. Lewis and R. N. McElhaney, *Biochim. Biophys. Acta, Biomembr.*, 2009, **1788**, 2069-2079.

10. A. Yamaji-Hasegawa and M. Tsujimoto, *Biol. Pharm. Bull.*, 2006, **29**, 1547-1553.

11. M. Langner and K. Kubica, *Chem. Phys. Lipids*, 1999, **101**, 3-35.

12. S. Sodin-Semrl, B. Rozman, A. Iglic and V. Kralj-Iglic, *Chapter 4: Antiphospholipid Syndrome: Mechanisms Revealed in Erythrocyte and Liposome Studies*, Academic Press, 2008.

13. N. R. Pallas and B. A. Pethica, *Langmuir*, 1985, **1**, 509-513.

14. M. Kotulska and K. Kubica, *Chapter 1 Random Processes in the Appearance and Dynamics of an Electropore in a Lipid Membrane*, Academic Press, 2008.

15. Y. Barenholz, D. Gibbes, B. J. Litman, J. Goll, T. E. Thompson and F. D. Carlson, *Biochemistry*, 1977, **16**, 2806-2810.

16. I. Zawisza, A. Lachenwitzer, V. Zamlynny, S. L. Horswell, J. D. Goddard and J. Lipkowski, *Biophys. J.*, 2003, **85**, 4055-4075.

17. V. Erokhin, *Langmuir-Blodgett films of biological molecules*, Academic Press, Burlington, 2002.

18. M. C. Petty, *Langmuir-Blodgett Films-An Introduction*, Cambridge University Press, Cambridge, 1996.

19. A. P. Girard-Egrot and L. J. Blum, *Langmuir-Blodgett Technique for Synthesis of Biomimetic Lipid Membranes*, Springer US, 2007.

20. I. Zawisza, X. M. Bin and J. Lipkowski, *Langmuir*, 2007, **23**, 5180-5194.

21. L. Perino-Gallice, G. Fragneto, U. Mennicke, T. Salditt and F. Rieutord, *Eur. Phys. J. E*, 2002, **8**, 275-282.

22. A. L. Plant, *Langmuir*, 1993, **9**, 2764-2767.

23. F. T. Buoninsegni, R. Herrero and M. R. Moncelli, *J. Electroanal. Chem.*, 1998, **452**, 33-42.

24. J. Lipkowski and L. Stolberg, *Adsorption of molecules at metal electrodes*, Wiley-VCH, New York, 1992.

25. B. Alberts, D. Bray, J. Lewis, M. Raff, K. Roberts and J. D. Watson, *Molecular Biology of the Cell*, Garland Science, New York, 1994.

26. *www.wikipedia.org*.

27. T. Y. Tsang and R. D. Astumian, *Ann. Rev. Physiol.*, 1988, **50**, 273-290.

28. M. P. Rols, *Biochim. Biophys. Acta, Biomembr.*, 2006, **1758**, 423-428.

29. J. Teissie, M. Golzio and M. P. Rols, *Biochimica et Biophysica Acta (BBA) - General Subjects*, 2005, **1724**, 270-280.

30. A. Nelson and N. Auffret, *J. Electroanal. Chem. Interfac.*, 1988, **244**, 99-113.

31. R. Guidelli, G. Aloisi, L. Becucci, A. Dolfi, M. Rosa Moncelli and F. Tadini Buoninsegni, *J. Electroanal. Chem.*, 2001, **504**, 1-28.

32. A. Nelson, *Curr. Opin. Colloid Interface Sci.*, 2010, **15**, 455-466.

33. V. Stauffer, R. Stoodley, J. O. Agak and D. Bizzotto, *J. Electroanal. Chem.*, 2001, **516**, 73-82.

34. I. R. Miller, *Topics in Bioelectrochemistry and Bioenergetics*, Wiley, Chichester, 1981.

35. A. Nelson and A. Benton, *J. Electroanal. Chem. Interfac.*, 1986, **202**, 253-270.

36. D. Bizzotto and A. Nelson, *Langmuir*, 1998, **14**, 6269-6273.

37. D. M. Kolb, *Prog. Surf. Sci.*, 1996, **51**, 109-173.

38. J. Lipkowski, *Phys. Chem. Chem. Phys.*, 2010, **12**, 13874-13887.

39. R. N. A. H. Lewis and R. N. McElhaney, *Biophys. J.*, 1993, **64**, 1081-1096.

40. I. Burgess, M. Li, S. L. Horswell, G. Szymanski, J. Lipkowski, J. Majewski and S. Satija, *Biophys. J.*, 2004, **86**, 1763-1776.

41. A. R. Hillman, K. S. Ryder, E. Madrid, A. W. Burley, R. J. Wiltshire, J. Merotra, M. Grau, S. L. Horswell, A. Glidle, R. M. Dalgliesh, A. Hughes, R. Cubitt and A. Wildes, *Faraday Discuss.*, 2010, **145**, 357-379.

42. A. Watts, K. Harlos and D. Marsh, *Biochim. Biophys. Acta, Biomembr.*, 1981, **645**, 91-96.

43. M. Li, M. Chen, E. Sheepwash, C. L. Brosseau, H. Li, B. Pettinger, H. Gruler and J. Lipkowski, *Langmuir*, 2008, **24**, 10313-10323.

44. S. Xu, G. Szymanski and J. Lipkowski, *J. Am. Chem. Soc.*, 2004, **126**, 12276-12277.

45. W. G. Golden and D. D. Saperstein, *Fourier Transform Infrared Reflection-Absorption Spectroscopy of Surface Species*, Elsevier, 1983.

46. I. Zawisza, G. Wittstock, R. Boukherroub and S. Szunerits, *Langmuir*, 2007, **23**, 9303-9309.

47. I. Zawisza, G. Wittstock, R. Boukherroub and S. Szunerits, *Langmuir*, 2008, **24**, 3922-3929.

48. S. L. Horswell, V. Zamlynny, H.-Q. Li, A. R. Merrill and J. Lipkowski, *Faraday Discuss.*, 2002, **121**, 405-422.

49. X. Bin, I. Zawisza, J. D. Goddard and J. Lipkowski, *Langmuir*, 2005, **21**, 330-347.

50. X. Bin, S. L. Horswell and J. Lipkowski, *Biophys. J.*, 2005, **89**, 592-604.

51. R. N. A. H. Lewis and R. N. McElhaney, *Chem. Phys. Lipids*, 1998, **96**, 9-21.

52. J. C. Weaver and Y. A. Chizmadzhev, *Bioelectrochem. Bioenerg.*, 1996, **41**, 135-160.

53. P. Thomas Vernier, Y. Sun, L. Marcu, C. M. Craft and M. A. Gundersen, *Biophys. J.*, 2004, **86**, 4040-4048.

54. H. Terlau and W. Stuhmer, *Naturwissenschaften*, 1998, **85**, 437-444.

55. S. W. Jones, *J. Bioenerg. Biomembr.*, 1998, **30**, 299-312.

56. E. Sackmann, *Science*, 1996, **271**, 43-48.

57. V. Zamlynny, I. Zawisza and J. Lipkowski, *Langmuir*, 2003, **19**, 132-145.

58. I. Zawisza, I. Burgess, G. Szymanski, J. Lipkowski, J. Majewski and S. Satija, *Electrochim. Acta.*, 2004, **49**, 3651-3664.

59. I. Zawisza and J. Lipkowski, *Langmuir*, 2004, **20**, 4579-4589.

60. C. L. Brosseau, X. Bin, S. G. Roscoe and J. Lipkowski, *J. Electroanal. Chem.*, 2008, **621**, 222-228.

61. D. Matyszewska, J. Leitch, R. Bilewicz and J. Lipkowski, *Langmuir*, 2008, **24**, 7408-7412.

62. T. Laredo, J. R. Dutcher and J. Lipkowski, *Langmuir*, 2011, **27**, 10072-10087.

CHAPTER 2: THEORY AND TECHNIQUES

2.1 Introduction

The objective of this chapter is to introduce the reader to the operational methodology of the techniques used for this research and to outline the theory behind them.

First the Langmuir-Blodgett (LB) technique, the technology that allows building up organized lipid bilayers onto Au, is described. This is followed with a review of the principles and the methodology for spectroscopic ellipsometry measurements. An overview of the electrochemical techniques is followed by a brief introduction to electromagnetic radiation and an explanation of the physical optics at interfaces. The last part of this chapter provides a review of the PM-IRRAS theory and technique, including a description of the experimental setup and the acquisition of IR spectra.

2.2 Langmuir-Blodgett Technique

2.2.1 Surface Energy

In order to understand the LB technique it is necessary to introduce some background in surface chemistry.

Molecules present in a bulk of a liquid experience balanced interactions by attractive forces in all directions. At the gas/liquid interface, the equilibrium of forces is disrupted and a molecule is surrounded by fewer molecules, creating a larger attraction torwards the liquid phase. The effect of this situation is the increase of free energy at the air/water interface, which means that the interface spontaneously minimizes its area and contracts. The linear force associated with this free energy and acting on the surface molecules is called surface tension (γ). The direction of the force relative to the interface is shown in Figure 2.1.

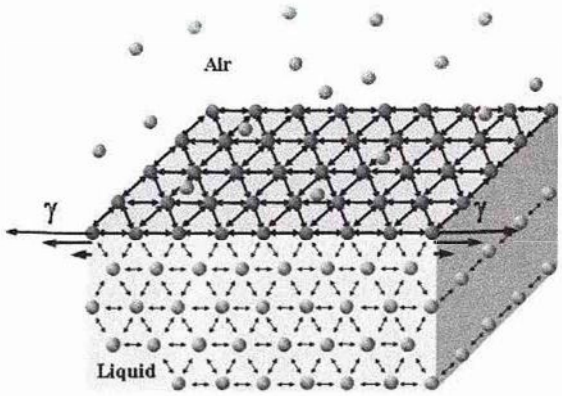

Figure 2.1: Surface tension at the air-water interface [1].

The surface tension of a gas/liquid interface can be equated to the specific surface energy. This can be expressed as the partial derivative of the free energy of the system (*G*) with respect to the surface area (*A*) as in Eq. 2.1

$$\gamma = \left(\frac{\partial G}{\partial A}\right)_{T,P,n_i}$$

Eq. 2.1

In Eq. 2.1, *G* is the total Gibbs free energy of the system, while temperature *T*, pressure *P* and amounts of all components n_i are held constant [1, 2].

Amphiphilic biomolecules such as phospholipids self-assemble at the gas/liquid interface, spontaneously forming a monolayer. The presence of a monomolecular film on a liquid surface invariably results in a reduction of the free energy of the system due to the creation of interactions between the hydrophilic polar group and the water surface molecules, thus reducing the surface tension. The resulting effect of the reduction of the surface tension leads to an expansion of an air/water interface in the presence of surfactants. If the available surface area of the monolayer is reduced by a barrier system the molecules start to exert a repulsive effect on each other. This two-dimensional analogue of a pressure is called surface pressure and is given by the following relationship:

$$\pi = \gamma_0 - \gamma$$

Eq. 2.2

where γ_0 is the surface tension of the pure liquid and γ is the surface tension of the film-covered surface [1].

2.2.2 Surface Pressure (π) - Area (A) Isotherm

When a monolayer at the gas/liquid interface is compressed, the amphiphilic molecules self-organize and the monolayer undergoes several phase transformations analogous to the three-dimensional gaseous, liquid and solid states to finally form a floating monolayer perfectly ordered at the liquid surface. These phase transformations are easily identified by the measurement of the change in the surface pressure as a function of the area available to each molecule. Two examples of isotherms are presented in Figure 2.2. When the available area is large, the molecules are widely separated with hydrophobic chains distributed near the interface; there are no interactions with each other. They move independently like a two-dimensional gas. This phase is called the "Gaseous phase" (G).

If the barrier reduces by compression the surface area, a first order-transition from the "Gas" to "Liquid" (L) phase occurs. As the area is compressed a "Liquid-Expanded" (LE) phase is formed. In this stage, the molecules become closer and start to interact; the hydrocarbon chains start to lift away but are conformationally disordered with a weak chain-chain interaction; the heads of the molecules are translationally disordered.

Further compression leads to a second first-order thermodynamic transition to the "Liquid Condensed" phase (LC), marked by a plateau in the isotherm (see Figure 2.2) corresponding to the coexistence of LE and LC phases [3]. The molecules in the LC phase normally have the chains fully extended but tilted at an angle to the vertical. In this region of the isotherm, the phase is compressible but less so than in the LE phase, hence the slope of the isotherm is steeper (Figure 2.2).

Under further compression the "Solid" or "Crystalline" state is reached; this state is typically observable after a kink on the isotherm. This phase is also referred to as a mesophase, the order is not as a crystalline structure but the molecules have a greater degree of order than liquids. The molecules are closely packed and the hydrocarbon chains are fully extended. The compressibility is low and this results in a steep slope in the isotherm.

If compression is further applied to the monolayer after reaching the solid state, the molecules are forced out of the interfacial film and molecular layers ride on top of each other to form disordered multilayers; this stage is called collapse [2, 4].

π-A isotherms offer information about the monolayer properties, for example its stability, interaction of species in the subphase with the monolayer, orientation and conformational transformations of the molecules [5]. The shape of π-A isotherms is strongly influenced by many factors. Physical and chemical properties of the amphiphiles such as their polarity, size, shape and interaction with water and/or the neighbouring headgroups strongly influence the arrangement of the hydrocarbon chains [6]. The experimental conditions, for example pH, subphase composition and subphase temperature, affect the π-A isotherms and dramatic changes in the deposition process may result, thus a very careful control of these factors is needed to obtain reproducible results.

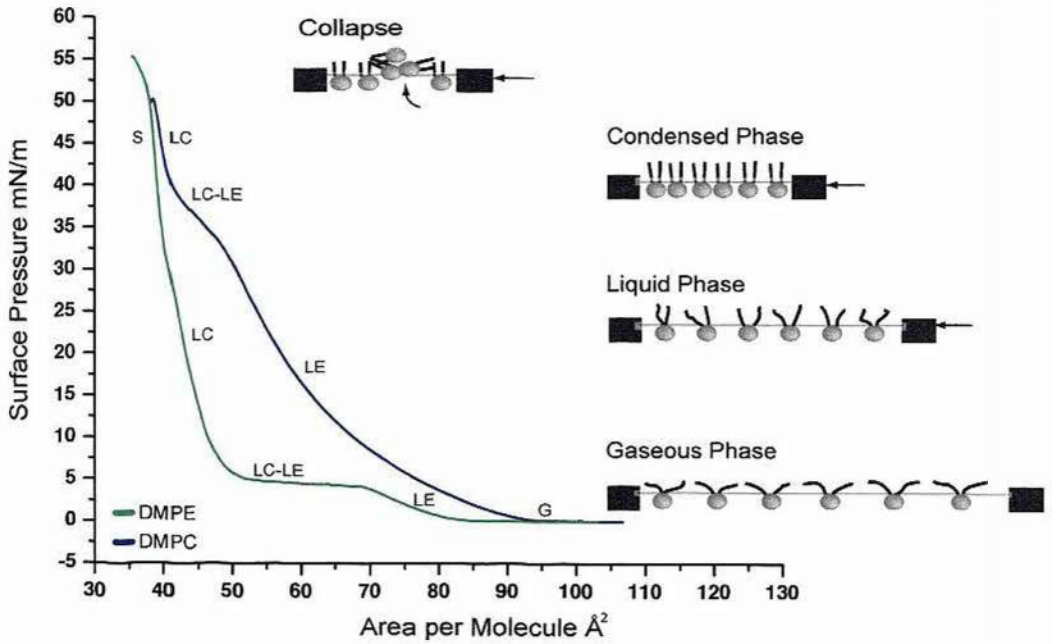

Figure 2.2: Compression isotherms for monolayers spread at the air/water interface of a Langmuir trough.

2.2.3 Monolayer Deposition

In 1917, Irving Langmuir put forward evidence for the monomolecular nature of the film as well as the orientation of the molecules at the air/water interface [7]. A few years later he showed how these monomolecular films could be transferred onto solid substrates [8]. This technique involved the vertical movement of a solid substrate through the monolayer/air interface. This technique is universally known as Langmuir-Blodgett (LB) deposition.

During deposition, surface pressure and temperature are usually controlled for a high quality floating monolayer. The LB deposition is usually carried out in the "Solid" phase. The high surface pressure ensures strong lateral cohesion and homogeneity within the interfacial film. The surface pressure is chosen depending on the monolayer's nature and is often established empirically [9]. Generally, temperatures ranging from 15 to 20°C are used. Different substrates such as mica, silica, metal, glass, quartz and silicon can be used for LB deposition. Depending on the substrate nature, the monolayer created at the air/water interface is deposited by raising the solid substrate from the subphase through the monolayer as shown in Figure 2.3. In this case the hydrophilic headgroups interact with a hydrophilic surface (*e.g.* glass, SiO_2) whereas if the solid substrate is hydrophobic (HOPG, silanized SiO_2, *etc.*) the first layer is then deposited by lowering the substrate into the subphase through the monolayer, when hydrophobic alkyl chains from the monolayer interact with the hydrophobic surface.

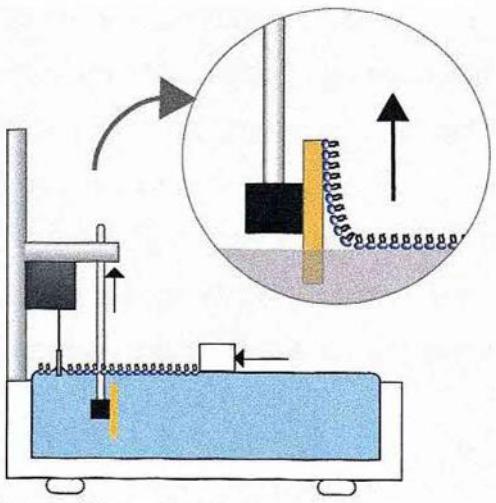

Figure 2.3: Scheme of deposition of LB films onto gold surface by withdrawing a substrate.

In 1935, Katharine Blodgett demonstrated the sequential transfer of monolayers onto the solid substrate to form multilayer films [10]. Figure 2.4 shows the different kinds of LB multilayers that can be built up by successive depositions of single layers.

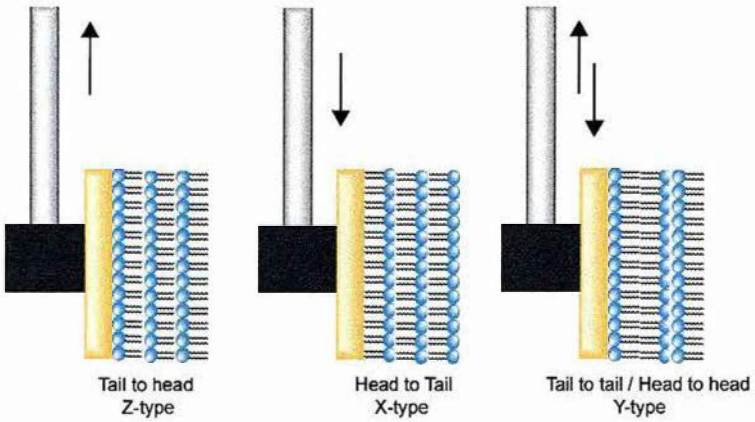

Figure 2.4: LB deposition structures onto a solid substrate.

The use of the LB technique allows the transfer the monolayer in different ways: only during the downstroke (X-type deposition), only during the upstroke (Z-type deposition) or both during down- and upstroke of the substrate through the interface. This last mode, called Y-type, is the most characteristic configuration of the biological membranes. In this deposition mode the molecules normally stack in head-to-head and tail-to-tail configuration [11, 12].

Hughes *et al.* reported in 2002 the stripping off from the solid substrate of the first monolayer at the creation of the second layer when a second immersion takes place [13]. To avoid this, Tamm and McConnell suggested a combined method for the creation of phospholipid bilayers on hydrophilic substrates. The first layer is transferred by vertical LB deposition (Z-type) and the second one by the horizontal Langmuir-Schaefer (LS) method [14]. In the LS technique, the solid substrate coated with the first monolayer is slowly brought into horizontal contact with the monolayer formed at the air/water interface allowing tail-to-tail interaction as shown in Figure 2.5.

The creation of bilayers using an LB plus LS method has been reported to produce ordered bilayers in which the chains of the phospholipids were less tilted

than in bilayers formed by fusion of vesicles [15]. The structure of these bilayers is better controlled with a higher packing density than for bilayers formed by the spontaneous fusion of vesicles [16].

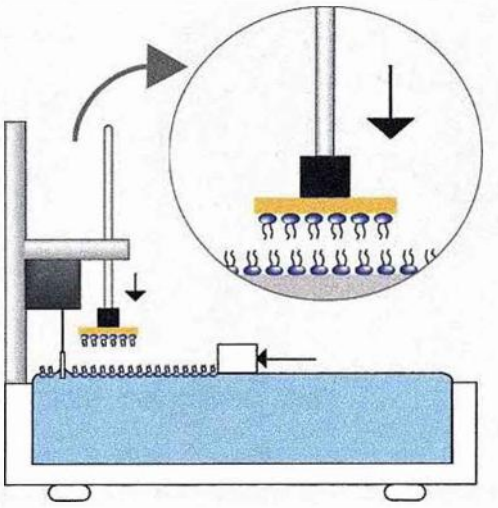

Figure 2.5: Scheme of the deposition of the second leaflet by the LS method.

2.3 Spectroscopic Ellipsometry

Spectroscopic ellipsometry is an optical measurement technique that characterizes light reflection from samples. The application area of spectroscopic ellipsometry is quite wide since it can provide understanding of thin film structures and properties such as thickness, refractive index, percentage of porosity, transparency and dielectric properties.

One of the remarkable features of spectroscopic ellipsometry is the high precision of the measurement; a very high thickness sensitivity of ≈0.1 Å can be obtained. It is a non-destructive technique and measurements are performed relatively quickly and easily [17]

2.3.1 Ellipsometry Measurements

The principle of this technique relies on the change of the polarization state of light when it is reflected from a surface. The reflection of linearly polarized light by a surface results in an elliptically polarized wave characterized by the phase difference (Δ) and amplitude ratio (Ψ). These two parameters are called the ellipsometry angles and are experimentally calculated by the ellipsometer.

When linearly polarized light is reflected from a surface, a change in Δ and Ψ of the parallel (E_{ip}) and perpendicular (E_{is}) components of the electrical field relative to the plane containing the incident and reflected beams takes place as shown in Figure 2.6 [17].

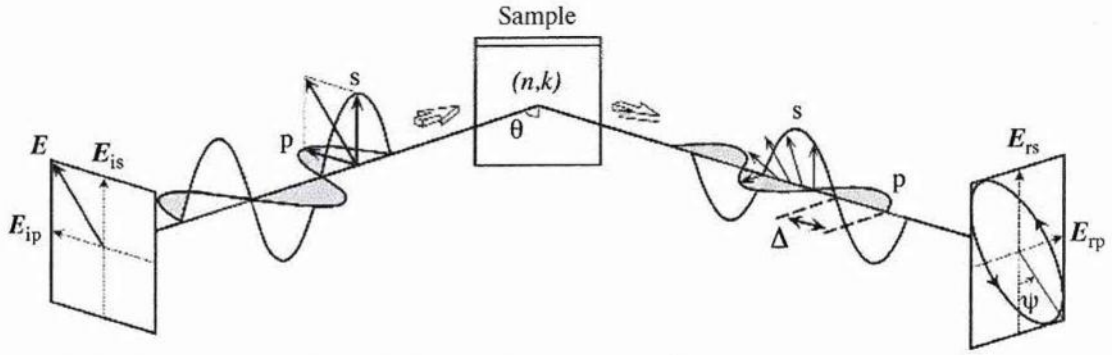

Figure 2.6: Measurement principle of ellipsometry [17].

The fundamental equation of ellipsometry relates the measurements (Δ, Ψ) by the ratio of the amplitude reflection coefficients for p- and s-polarizations, r^p and r^s, in the following way [18]:

$$\rho = \tan\Psi \exp(i\Delta) = \frac{r^p}{r^s}$$

Eq. 2.3

where Ψ represents the angle determined from the r^p and r^s, and Δ the phase difference induced by the reflection between the p- and s-polarizations as described in Eq. 2.4 and Eq. 2.5:

$$\tan\Psi = \frac{|r^p|}{|r^s|} = \left(\frac{E_{r,p}}{E_{i,p}}\right) \Big/ \left(\frac{E_{r,s}}{E_{i,s}}\right)$$

Eq. 2.4

$$\Delta = \delta_{rp} - \delta_{rs}$$

Eq. 2.5

The light transmitted through a phospholipid bilayer deposited on gold can be represented as shown in Figure 2.7.

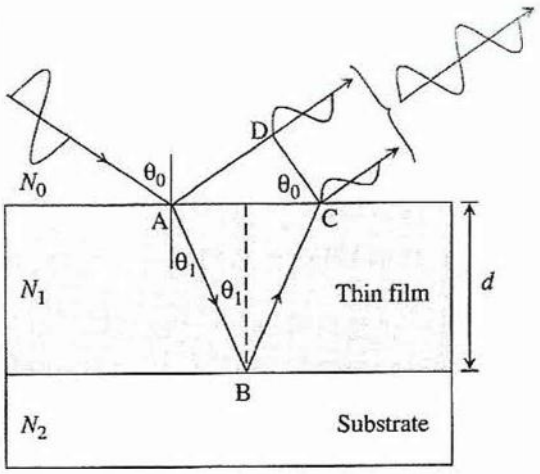

Figure 2.7: Schematic representation of the light passing through a three boundary system [17].

The incident wave is reflected at the film surface and at the film/substrate interface. In this case the light wave reflected on the surface overlaps with the light wave reflected at the film/substrate interface, optical interference occurs and the wave amplitude becomes larger by this interference effect. The total reflection coefficient for both components is:

$$r^p = \frac{r_{01,p} + r_{12,p}\exp(-i2\beta)}{1 + r_{01,p}r_{12,p}\exp(-i2\beta)}$$

Eq. 2.6

and

$$r^s = \frac{r_{01,s} + r_{12,s}\exp(-i2\beta)}{1 + r_{01,s}r_{12,s}\exp(-i2\beta)}$$

Eq. 2.7

where r_{jk} represent the amplitude reflection coefficient at each interface for s- and p-polarized light and β represents the film phase thickness expressed as:

$$\beta = 2\pi\left(\frac{d}{\lambda}\right)N_1\cos\theta_1$$

Eq. 2.8

where d is film thickness, N is the complex refractive index, θ_1 is the reflection angle and λ is the wavelength of the light.

The complex refractive index of air is given by N_0=0; λ and θ_0 are fixed by the ellipsometer. The polarized light irradiates a sample at the Brewster angle, typically 70-80°; at this θ_0, the difference between E_{rp} and E_{rs} is maximized. The values for N_1 and θ_1 are usually known in advance; if θ_1 is unknown it can be obtained by applying Snell's law. From the analysis of interference by ellipsometry, the film thickness can be estimated using Eq. 2.9.

$$\rho = \left(\frac{r^p}{r^s}\right) = \left[\frac{r_{01,p} + r_{12,p}\exp(-i2\beta)}{1 + r_{01,p}r_{12,p}\exp(-i2\beta)}\right] \Big/ \left[\frac{r_{01,s} + r_{12,s}\exp(-i2\beta)}{1 + r_{01,s}r_{12,s}\exp(-i2\beta)}\right]$$

Eq. 2.9

When the refractive index of the thin film (N_1) is not known, dielectric function modelling is required. The dielectric function can be extracted easily using a mathematical inversion, performed by using linear regression analysis. There are many dielectric function models and an appropriate model is selected according to the optical properties of the sample. For dielectric function modelling in a transparent region, the Cauchy model is used. The Cauchy equation describes the dispersion of film refractive index as a slowly varying function of wavelength λ with an exponential absorption tail [19].

$$N(\lambda) = A + B\lambda^{-2} + C\lambda^{-4} + D\lambda^{-6} + \ldots$$

Eq. 2.10

In general, when the dielectric functions of each layer are known, the thickness analysis is performed easily.

2.4 Electrochemistry

Interfacial electrochemistry involves the study of structures and processes in the region where the solution and the electrode are in contact; this region is called the interface. The electrochemistry work achieved during 1800's led to the fact that conduction of electricity by the solution is different than that by the metal, thus inherently properties between these two domains can be found at the interface.

In 1879, Helmholtz proposed the first model of the electrical double layer based on the importance of the electrical nature of a solid surface being in contact with an electrolyte. He postulated that at the interface, the charge present at the electrode surface is compensated by solvent-free ions from the solution giving rise to a notion of a fixed (rigid) double layer [20]. This rigid double layer was described as a parallel-plate capacitor, which has the following relation with the stored charge density, σ, and the voltage drop, V, between the plates [21]:

$$\frac{\partial \sigma}{\partial V} = C_d = \frac{\varepsilon \varepsilon_0}{d}$$

Eq. 2.11

where C_d is the specific differential capacitance, ε is the dielectric constant of the medium, ε_0 is the permittivity of free space, and d is the interplate spacing.

This model predicts that the interfacial capacitance should be constant, regardless of the applied potential at the electrode which is not always observed in experiments.

During 1910 and 1913, Gouy and Chapman modified the Helmholtz model, suggesting a diffuse double layer of charge composed of ions and solvent molecules where the greatest concentration of excess charge was adjacent to the electrode surface and the electrostatic forces are able to prevail over the thermal motion. At greater distances and progressively lesser concentrations, the strength of those forces became weaker. The capacitance of the interfacial region according to this model was calculated using the Eq. 2.12 [21].

$$C_d = \left(\frac{2z^2e^2\varepsilon\varepsilon_0 n^0}{\kappa T}\right)^{\frac{1}{2}} \cosh\left(\frac{ze\phi_0}{2\kappa T}\right)$$

Eq. 2.12

where C_d is the differential capacitance in the double layer, z is the charge magnitude of each ion, e is the electronic charge, ε the dielectric constant of the medium and ε_0 the permittivity of free space; n is the bulk concentration, κ the Boltzmann constant, T the absolute temperature and ϕ the electrostatic potential.

This model predicts that the capacitance plotted as a function of applied electrode potential should display a minimum and that the capacitance should vary with concentration. However, the model assumes the ions to be point charges, with no size.

In 1924, Stern combined these two model approaches developed by Helmholtz and Gouy-Chapman; Stern considered that the double layer was formed by a compact layer next to the electrode ("inner" layer or "Helmholtz" layer) followed by a "diffuse" layer that extends into the bulk solution. This model was known as the Gouy-Chapman-Stern (GCS) model. It allows for the random motion of ions and for the ions to have a finite size. Whilst it is an improvement, it still does not predict many real systems well, due to the lack of consideration of factors such as the structure of the dielectric in the double layer, the possibility of absorption on to the surface and the interaction between solvent dipole moments and the electrode [22].

In 1947, Grahame refined the Stern model by considering the specific adsorption of species from solution. Figure 2.8 shows a schematic representation of this model. Three regions constituted the Grahame model, the Helmholtz or *compact layer*, formed by the specifically and non-specifically adsorbed ions, and the *diffuse layer*. The specifically adsorbed ions are ions that have lost part of their solvation shell and can approach closer to the electrode surface, creating very strong bonds. The inner Helmholtz plane (IHP) passes through the centres of these ions. The outer Helmholtz plane (OHP) passes through the centres of the solvated and non-specifically adsorbed ions. These ions were nonspecifically adsorbed and were attracted to the electrode surface by long-range coulombic forces. The diffuse layer is

a region of scattered ions which covered the area from outside the OHP into the bulk of solution [22].

Although the Grahame model of the electric double layer has been adjusted afterwards, it remains the simplest and most accurate model for the structure of the interfacial region.

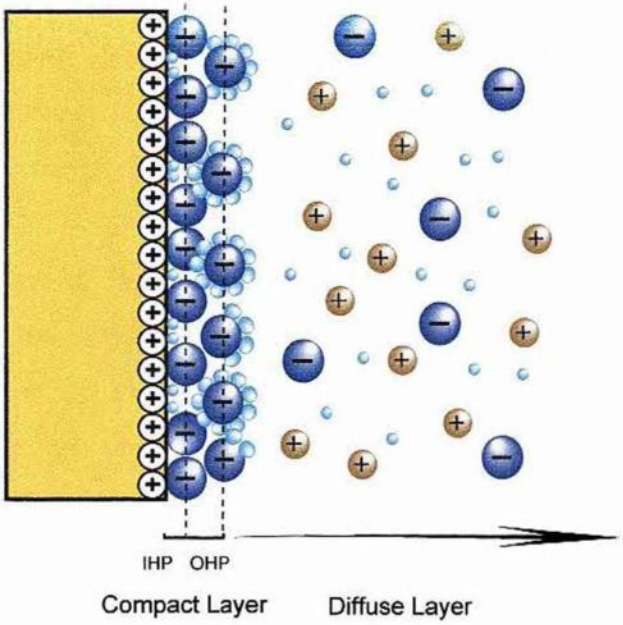

Figure 2.8: Schematic representation of Grahame model of the electric double layer.

In the absence of specific adsorption on the electrode surface, the capacitance of the inner and outer layer can be modelled as two parallel plate capacitors in series. The total double layer capacitance can be expressed by Eq. 2.13:

$$\frac{1}{C_d} = \frac{1}{C_H} + \frac{1}{C_D} = \frac{d}{\varepsilon\varepsilon_0} + \frac{1}{\left(2\varepsilon\varepsilon_0 z^2 e^2 n^0 / \kappa T\right)^{\frac{1}{2}} \cosh\left(ze\phi_0 / 2\kappa T\right)}$$

Eq. 2.13

where C_d is the differential capacitance in the double layer, C_H and C_D are the capacitance of the Helmholtz and diffuse region of the double layer.

The ratio of the two contributions in Eq. 2.13 depends on the values of the electrode charge and the electrolyte concentration, as well as on the particular type of the media in contact. The diffuse layer capacitance (C_D) grows with the increase of the absolute value of the charge and concentrated solutions of about 1 M or higher. This term ($1/C_D$) then represents a minor correction to the compact layer term, and the simple Helmholtz model is used for qualitative interpretation of the data.

On the other hand, for small absolute value of the potential drop and for diluted solutions, the diffuse layer determines the shape of the capacitance curves. C_H is independent of the concentration because in diluted electrolytes most of the charge is confined in the Helmholz plane [23].

2.4.1 Adsorption at Electrode Surfaces

Electrified interfaces are often studied for the characterisation of species that are adsorbed in between the metal/solution interface. Molecular adsorption has been studied for the past decade using various different techniques. Raman and infrared spectroscopy defined the orientation and the nature of the chemical bond. Images of the electrode surface covered by the adsorbate were acquired using scanning tunnelling microscopy and atomic force microscopy. In spite of these studies there is still much to be done in understanding how the electrode potential or charge density affects the molecular adsorption on solid electrodes.

The capacitance in the presence of adsorption relates the charge on the metal surface σ_M to the applied potential by the following equation:

$$C = \frac{\partial \sigma_M}{\partial E}$$

Eq. 2.14

The charge on the metal surface can also be expressed as a function of the Gibbs surface excess Γ and the applied potential E as:

$$d\sigma_M = \left(\frac{\partial \sigma_M}{\partial \Gamma}\right)_E d\Gamma + \left(\frac{\partial \sigma_M}{\partial E}\right)_\Gamma dE$$

Eq. 2.15

Differentiation of Eq. 2.15 with respect to the electrode potential gives capacitance of the electrode in the presence of specific adsorption:

$$C = \left(\frac{\partial \sigma_M}{\partial \Gamma}\right)_E \frac{d\Gamma}{dE} + \left(\frac{\partial \sigma_M}{\partial E}\right)_\Gamma = C_{pseudo} + C_{true}$$

Eq. 2.16

There are two contributions to the total capacitance: the true capacitance is the capacitance obtained by constant adsorbate coverage and the pseudo capacitance is the capacity given when the coverage changes depending on the applied potential. This C_{pseudo} represents the changes in the phase state of the absorbed film and is manifested in a C-E plot by a peak or step. The capacitance can be calculated when a small amplitude alternating voltage is applied to the electrode as is described in Chapter 3.

2.4.2 Chronocoulometry

It is well known that for a gold single crystal electrodes in aqueous solutions, surface reconstruction phenomena can be induced when potential is applied. The kinetics of surface reconstruction for Au(111) surface is very slow, taking from 1 to 2 minutes for the complete reconstruction of 1x1 to √3x22 reconstruction [24]. Due to the slow reconstruction, a shift of the capacity-potential curve and hysteresis is usually observed. In experiments with a specific adsorption on Au(111) surface, the overlap in the kinetics of the surface reconstruction, with the kinetics of slow heterogeneous adsorption-desorption phenomena, makes the measurement of the equilibrium capacity (zero frequency) a difficult task. In order to avoid this problem, another technique known as chronocoulometry has been developed [25].

In chonocoulometry, the charge density on solid electrodes at a potential E_i is determined. The potential is held at an initial value E_i for a period of time long enough to enable the equilibrium between the interface and the bulk of the electrolyte to be established. At this stage, no charge is measured, avoiding the problem associated with the slow kinetics of adsorption. After E_i, the potential is stepped to E_f which is a few millivolts more negative than the desorption potential of the organic species

investigated. During this very short period, the structure of the electrode surface is considered the same as that established at the initial potential. The current due to double layer charging is recorded as a function of time and digitally integrated; the difference between the charge density at a adsorption potential, E_i and desorption potential, E_f is measured as:

$$\Delta\sigma_M(E_i) = \sigma_M(E_f) - \sigma_M(E_i)$$

Eq. 2.17

The potential of zero charge (E_{pzc}) is determined from the position of the diffuse layer minimum on an independently measured differential capacity for a dilute solution of the pure supporting electrolyte. Thus, the absolute charge density at E_f is calculated with the following equation:

$$\Delta\sigma_M(E_{pzc}) = \sigma_M(E_f) - \sigma_M(E_{pzc}) = \sigma_M(E_f)$$

Eq. 2.18

The charge, σ_M, at E_f is independent of the presence of molecules in the solution because there is no adsorption at E_f. This allows the calculation of the absolute charge density as a function of the applied potential using Eq. 2.17.

The charge densities are integrated with respect to the electrode potential, E, to give:

$$\gamma(E) = -\int_{E_f}^{E_i} \sigma_M dE + \gamma(E_f)$$

Eq. 2.19

The lower integration constant, $\gamma(E_f)$, is not known; however the value is independent of the presence or absence of molecules because at E_f, there is not adsorption. Therefore the film pressure of adsorbed molecules can be calculated as:

$$\pi = \gamma_{\theta=0} - \gamma_{\theta} = \int_{E_f}^{E_i} \sigma_{M_\theta} dE - \int_{E_f}^{E_i} \sigma_{M_{\theta=o}} dE$$

Eq. 2.20

where the subscripts θ and $\theta=0$ indicate the presence and absence of organic molecules in the bulk electrolyte [26].

2.5 Polarization Modulation Infrared Reflection Absorption Spectroscopy

2.5.1 Introduction

Infrared light is a transverse electromagnetic radiation that, according to the Maxwell's classical theory of electro- and magneto- dynamics, is characterized by a perpendicular electric field $\vec{E}$ and the magnetic induction field $\vec{B}$ [27]. These two components are oscillating periodically in space and time, perpendicularly to the direction of propagation as shown in Figure 2.8 [28].

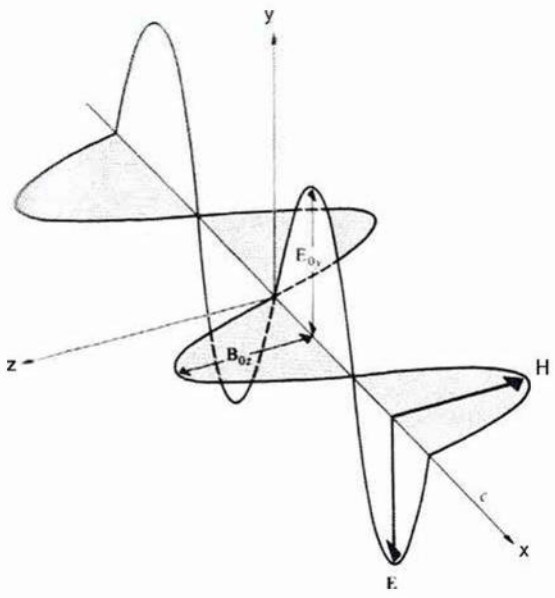

Figure 2.8: Direction of the electric and magnetic field with respect the propagation of an electromagnetic wave [29].

The electromagnetic wave is described by its intensity, its direction of propagation and its polarization state. The intensity of the beam can be described by

just one of its components due to the fact that the energy of the magnetic field is exactly the same as that of the electric field. It is convenient in our research to consider just the electric field E because only the electric field interacts with the vibrational modes of the molecules at any level of detectable strength. A planar electromagnetic wave that propagates in the vacuum is related to the electric field strength E at a moment in time t and a distance x from the origin by the following wave equation [27, 30]:

$$E = E_0 \cos\left(\frac{2\pi}{\lambda}x + \delta - \omega t\right) = \mathrm{Re}\left(E_0 \exp\left[-i\left(\frac{2\pi}{\lambda}x + \delta - \omega t\right)\right]\right)$$

Eq. 2.21

where E_0 represents the amplitude of the electric field strength and λ, ω and δ are the wavelength, the angular frequency, and the phase shift, respectively.

The wave equation in a condensed medium becomes:

$$E = \mathrm{Re}\left(E_0 \exp\left[-i\left(\frac{2\pi n}{\lambda}x + \delta - \omega t\right)\right]\exp\left(-\frac{2\pi k}{\lambda}x\right)\right)$$

Eq. 2.22

where n is the refractive index of the material that the radiation is propagated through. The absorption of the electric field by the medium is determined by the attenuation coefficient of the medium, k; in addition, n and k are components of the complex refractive index $\hat{n}$. Eq. 2.22 can be summarized by Eq. 2.24 using $\hat{n}$.

$$\hat{n} = n + ik$$

Eq. 2.23

$$E = \mathrm{Re}\left(E_0 \exp\left[-i\left(\frac{2\pi \hat{n}}{\lambda}x + \delta - \omega t\right)\right]\right)$$

Eq. 2.24

The oscillation of E in a single plane makes linearly polarized radiation; this state is essential for structural investigations because the angle between E and the transition dipole moment T_d of a vibrational mode is crucial for the intensity loss caused by an infrared absorption [31]. The energy dissipated per unit volume per unit time reaching the detector in an averaged time is called intensity I; for non-magnetic materials it is related to the amplitude of the electric field in the following way:

$$I = nk\nu \frac{E_0^2}{2} = nk\nu \left\langle E_0^2 \right\rangle$$

Eq. 2.25

where ν is the frequency and $\left\langle E_0^2 \right\rangle$ is the mean squared electric field strength (MSEFS) of the radiation incident on the detector. For a non-magnetic material the intensity can be written as [28,32]:

$$I = \varepsilon_0 c \frac{E_0^2}{2} = \varepsilon_0 c \left\langle E_0^2 \right\rangle$$

Eq. 2.26

where ε_0 is the permittivity of the vacuum.

During the absorption of the infrared radiation of selected frequencies, the molecules are excited to a higher energy state. These frequencies lie within the range of 10^{12}-10^{14} Hz. The absorption of the IR radiation involves, to a first approximation, the harmonic displacement of molecule atoms from their equilibrium position. Molecules with N atoms have 3N-6 number of ways that the atoms can vibrate. The frequency of such vibration modes is characteristic of the specific functional group and is described by Hooke's law:

$$\tilde{\nu} = \frac{1}{2\pi c}\sqrt{\frac{k}{\mu}}$$

Eq. 2.27

where c is the speed of light (in cm s^{-1}), k is the force constant and the μ is the reduced mass, given by the masses (m_1 and m_2) of the two bonded atoms:

$$\mu = \frac{m_1 m_2}{m_1 + m_2}$$

Eq. 2.28

The frequency of vibration is normally minimally affected by the nature of the other atoms within the molecule although, in some cases, vibrations may be coupled. Some shifts of absorbance are based on electronic effects due to proximal groups, hydrogen bonds, conjugation and/or ring strain, which can decrease the strength of the two bonded atoms, lowering the frequency of vibration.

2.5.2 Fourier Transform Infrared Spectroscopy

Fourier Transform Infrared Spectroscopy (FT-IR) is now considered one of the most powerful techniques for chemical analysis. FT-IR is based on the interference of radiation between two beams. This interference is produced by the interferometer that allows the controlled generation of interferograms. The interferograms are converted into a spectrum using a mathematical technique called a Fourier transform. Dispersive instruments have been displaced over the years by FT-IR spectrometers due to their multiple advantages such as simplicity, sensitivity, versatility and speed of analysis.

2.5.2.1 The Michelson Interferometer

The two-beams interferometer was designed by Albert Abraham Michelson in 1891; many others have subsequently been designed but the general theory of the Michelson interferometer is similar to those more recently fabricated.

The Michelson interferometer is a device that can divide an incident beam into two paths and then recombine the two beams after a path difference was introduced. Its basic optical layout is illustrated in Figure 2.9. The source emits a collimated beam of IR light which is partially reflected at the fixed mirror and partially transmitted to a movable mirror the after passing through the beam splitter. The movable mirror is able to move along the axis at a constant velocity, away from and towards the

beam splitter, creating a difference in distance travelled between the two beams which is called optical retardation, δ_r. When the beams return to the beam splitter, they recombine and are redirected onto the sample before being detected at the detector [33, 34].

The intensity of the signal detected (interferogram) is dependent on the retardation applied to the IR beam. If the mirrors are equidistant from the beam splitter (δ_r=0), the two beams are in phase, thus the beams interfere constructively and the intensity at the detector is the sum of the intensities and the interferogram displays a maximum in intensity, named the centreburst. If the retardation differs from 0, the two light beams from the mirrors are out of phase with each other, they interfere destructively, leading to a beam of low intensity.

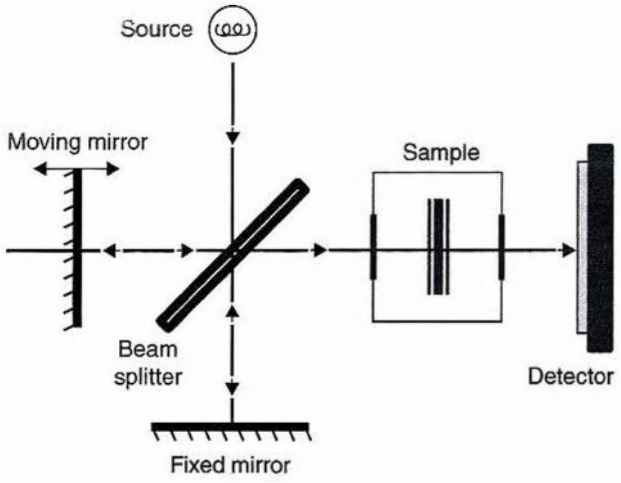

Figure 2.9: Schematic diagram of a Michelson Inteferometer [34].

The intensity of the inteferogram is dependent on the δ_r of the movable mirror and the wavenumber, $\bar{\nu}$ of the incident radiation by the following Eq. 2.29:

$$I(\delta_r) = 2\int_0^{+\infty} B(\bar{\nu})\cos(2\pi\bar{\nu}\delta_r)d\bar{\nu}$$

Eq. 2.29

where $B(\bar{\nu})$ is the intensity of the source as a function of its wavenumber after corrections from the distortions created by the beam splitter and the detector. Fourier

transformation of the Eq. 2.29 produces the IR spectrum (Eq. 2.30).

$$B(\bar{\nu}) = 2\int_0^{+\infty} I(\delta_r)\cos(2\pi\bar{\nu}\delta_r)d\delta_r$$

Eq. 2.30

2.5.3 Electromagnetic Radiation at an Interface

2.5.3.1 Introduction

The use of infrared reflection absorption spectroscopy for quantitative analysis of experimental studies requires a good understanding of the physics of reflection and refraction of the electromagnetic radiation. The behaviour of the radiation at the boundary between two phases can easily be described by the use of the Fresnel equations. The description becomes slightly more complex when three or more phases are studied. In spite of this difficulty, Hansen described these equations for a two-phase, three-phase, and *N*-phase stratified medium in a very popular paper in 1968 [32].

2.5.3.2 Reflection and Refraction of Electromagnetic Radiation at a Two-Phase Boundary

This section describes fundamentals of the reflection, refraction and absorption of the electromagnetic radiation at a system composed of a two-phase boundary. When the electromagnetic radiation is incident at a boundary between two phases, part of the beam is reflected and part of it is transmitted into the second medium. Figure 2.10 shows the incident, transmitted and refracted beam at the boundary of two dielectric materials with different refractive indices n_1 and n_2. The incident beam, shown in this figure by a dashed line, is composed by two linearly polarized orthogonal components. The electric field vector component that oscillates in the plane of incidence is known as p-polarized light and the one which oscillates in the plane perpendicular to the plane of incidence is called s-polarized light.

Using the law of reflection (Eq. 2.31) and the Snell's law of refraction (Eq. 2.32) one can calculate the angles of reflection and refraction of the electromagnetic radiation.

$$\theta_1^i = \theta_1^r$$

Eq. 2.31

$$n_1 \sin\theta_1^i = n_2 \sin\theta_2^t$$

Eq. 2.32

where n_j is the refractive index of a phase *j*.

These equations can be obtained by derivation of the Maxwell's equations for linear isotropic phases, using the conditions of continuity of the electric and magnetic field components tangential to the phase boundary.

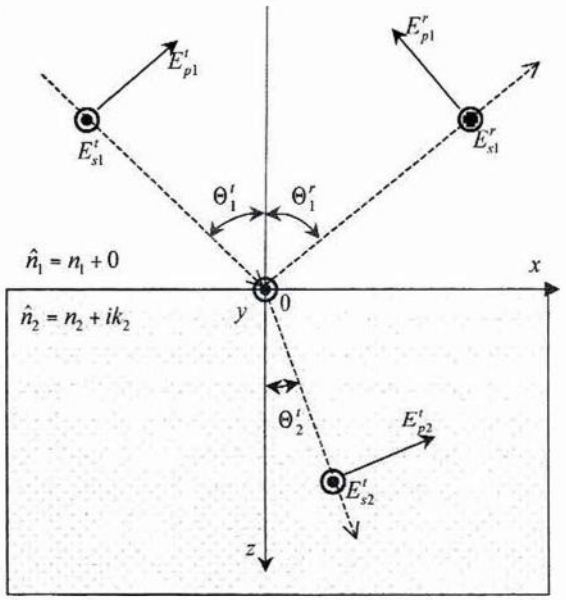

Figure 2.10: Reflection and refraction of the electromagnetic radiation at the boundary between transparent and absorbing medium [29].

Fresnel equations relate the electric field strength amplitudes of the incident, reflected, and refracted waves. These can be also derived from Maxwell's equations considering the same boundary conditions as above. For a plane boundary between two non-magnetic isotropic phases of infinite thickness, the Fresnel reflection (*r*) and transmission (*t*) coefficients are given by:

$$r_s = \frac{E_{s1}^r}{E_{s1}^i} = \frac{\xi_1 - \xi_2}{\xi_1 + \xi_2}$$

Eq. 2.33

$$r_p = \frac{E_{p1}^r}{E_{p1}^i} = \frac{\hat{n}_2^2\xi_1 - \hat{n}_1^2\xi_2}{\hat{n}_2^2\xi_1 + \hat{n}_1^2\xi_2}$$

Eq. 2.34

$$t_s = \frac{E_{s2}^t}{E_{s1}^i} = \frac{2\xi_1}{\xi_1 + \xi_2}$$

Eq. 2.35

$$t_p = \frac{E_{p2}^t}{E_{p1}^i} = \frac{2\hat{n}_2^2\xi_1}{\hat{n}_2^2\xi_1 + \hat{n}_1^2\xi_2}\left(\frac{\hat{n}_1}{\hat{n}_2}\right)$$

Eq. 2.36

where:

$$\xi_1 = \hat{n}_j \cos\theta_j^t = \sqrt{\hat{n}_j^2 - \hat{n}_1^2 \sin^2\theta_1^t} = \mathrm{Re}\,\xi_j + i\mathrm{Im}\xi_j$$

Eq. 2.37

The amplitude of the electric field for s- and p- polarized radiation oriented along the y axis is denoted as *E*; ξ_j can be calculated from experimentally available optical constants of the corresponding phase $\hat{n}_j$ and the angle of incidence θ_j^t.

The reflectance (*R*) and transmittance (*T*) are, respectively, given by the intensities of the reflected and transmitted radiation normalized by the intensity of the incident radiation, and are related to the Fresnel amplitude reflection and transmission coefficients in the following way:

$$R_{s,p} = \frac{I_{s,p1}^r}{I_{s,p1}^i} = \left|r_{s,p}\right|^2 = \hat{r}_{s,p} \cdot \hat{r}_{s,p}^*$$

Eq. 2.38

$$T_s = \frac{I_{s2}^t}{I_{s1}^i} = \frac{\mathrm{Re}(\xi_2)}{\xi_1}\left|t_s\right|^2 = \frac{\mathrm{Re}(\xi_2)}{\xi_1}\hat{t}_s \cdot \hat{t}_s^*$$

Eq. 2.39

and

$$T_p = \frac{\mathrm{Re}\left(\xi_2 / \hat{n}_2^2\right)}{\xi_1 / \hat{n}_2^2}\left|t_p\right|^2 = \frac{\mathrm{Re}\left(\xi_2 / \hat{n}_2^2\right)}{\xi_1 / \hat{n}_2^2}\hat{t}_s \cdot \hat{t}_s^*$$

Eq. 2.40

where t_p and t_s are the ratios of the amplitude of the electric field.

In addition, the determination of the phase shift of the electromagnetic wave, δ is feasible using the amplitude coefficients by the following relationship [32]:

$$\delta_{s,p}^r = Arg\left(r_{s,p}\right) = \tan^{-1}\left(\mathrm{Im}\left(r_{s,p}\right) / \mathrm{Re}\left(r_{s,p}\right)\right)$$

Eq. 2.41

At the surface, the electric field is a vectorial sum of the field of the incident and reflected wave. If the phase shift changes at reflection, the sum gives enhancement or attenuation of the electric field.

2.5.3.3 Reflection and Refraction of Electromagnetic Radiation at a Multiple-Phase Boundary

A four phase system is used when electrochemical *in situ* PM-IRRAS experiments are carried out. A film deposited on a metal surface is immersed in an electrolyte solution and pressed against an optical window. This system consists of four layers in which the first medium is an infrared transparent window that does not absorb IR light. The electrolyte, an adsorbed film and the metal are the other three phases and these are not transparent to the IR radiation.

The Fresnel equations for this system are derived considering that the phases are nonmagnetic, isotropic, homogeneous and infinitely parallel with perfectly sharp boundaries [30]. The first and the last phases are considered to be infinitely thick and all the intermediate phases j are characterized by the thicknesses h_j. The beam incident at an angle θ along the z-axis is considered a planar wave of wavelength λ.

The electromagnetic radiation at each phase boundary k, is fully described for

N phases with *N-1* boundaries by *N-1* matrices (M_j). For s- and p- polarized radiation these characteristic matrices are described by the following equations:

$$M_j^s = \begin{bmatrix} \cos\beta_j & \frac{-i}{\xi_j}\sin\beta_j \\ -i\xi_j \sin\beta_j & \cos\beta_j \end{bmatrix}$$

Eq. 2.42

$$M_j^p = \begin{bmatrix} \cos\beta_j & \frac{-i\hat{n}_j^2}{\xi_j}\sin\beta_j \\ -i\frac{\xi_j}{\hat{n}_j^2}\sin\beta_j & \cos\beta_j \end{bmatrix}$$

Eq. 2.43

where Eq, 2.37 defined ξ_j and

$$\beta_j = \frac{2\pi\xi_j h_j}{\lambda}$$

Eq. 2.44

where h_j is the thickness of a layer *j* and λ is the wavelength of the electromagnetic wave.

The matrix that characterizes the entire stratified medium (Eq. 2.45) is calculated by the multiplication of the characteristic matrices of all the phases restricted between the first and last phase.

$$M = \prod_{j=2}^{j=N-1} Mj$$

Eq. 2.45

The coefficients of the reflection and transmission are calculated using the characteristic matrix for the entire stratified medium using the following relationships:

$$\hat{r}_s = \frac{(m_{1,1} + m_{1,2}\xi_N)\xi_1 - (m_{2,1} + m_{2,2}\xi_N)}{(m_{1,1} + m_{1,2}\xi_N)\xi_1 + (m_{2,1} + m_{2,2}\xi_N)}$$

Eq. 2.46

$$\hat{r}_p = \frac{(m_{1,1} + m_{1,2}\xi_N/\hat{n}_N^2)\xi_1/\hat{n}_1^2 - (m_{2,1} + m_{2,2}\xi_N/\hat{n}_N^2)}{(m_{1,1} + m_{1,2}\xi_N/\hat{n}_N^2)\xi_1/\hat{n}_1^2 + (m_{2,1} + m_{2,2}\xi_N/\hat{n}_N^2)}$$

Eq. 2.47

$$\hat{t}_s = \frac{2\xi_1}{(m_{1,1} + m_{1,2}\xi_N)\xi_1 + (m_{2,1} + m_{2,2}\xi_N)}$$

Eq. 2.48

$$\hat{t}_p = \frac{2\xi_1/\hat{n}_1^2}{(m_{1,1} + m_{1,2}\xi_N/\hat{n}_N^2)\xi_1/\hat{n}_1^2 + (m_{2,1} + m_{2,2}\xi_N/\hat{n}_N^2)}\left(\frac{n_1}{\hat{n}_N}\right)$$

Eq. 2.49

where, the elements of the 2x2 characteristic matrix *M* are represented by m_{jk}.

Using the reflection coefficients $\hat{r}_s$ and $\hat{r}_p$ in Eq. 2.38, the reflectance for s- and p- polarized light in the entire assembly can be calculated, while the transmittance for the whole stack for s- and p- polarized light can be determined from the corresponding transmission coefficients using Eq. 2.39 and Eq. 2.40.

The matrix approach is used to model the reflectance of an experimental *in situ* PM-IRRAS experiment where the number of phases applied is four; simulation of *ex situ* PM-IRRAS is also possible. Simulated spectra allow the quantitative analysis of the adsorbed analyte films at the electrode surface.

2.5.3.4 Mean Squared Electric Field Strength

Quantitative orientational analysis of the films adsorbed on a gold electrode requires an accurate knowledge of the mean squared electric field strength (MSEFS) at the metal surface and in the bulk of the thin-layer cavity. Expressions for the calculation of the MSEFS at any point, z, within a stratified medium, have been developed recently by Zamlynny [29,30]. The derivation of these expressions leads to the final equations of the MSEFS at *k* interfaces. These expressions are given below:

For s-polarized radiation,

$$\left\langle E_{yk}^{s2} \right\rangle = \frac{1}{2}\left|U_k(z)\right|^2$$

Eq. 2.50

There are two expressions for the p-polarized radiation, one for each component of the electric field vector oriented along the x and z coordinate axes:

$$\left\langle E_{xk}^{p2} \right\rangle = \frac{1}{2}\left|V_k(z)\right|^2$$

Eq. 2.51

$$\left\langle E_{zk}^{p2} \right\rangle = \frac{1}{2}\left|\frac{n_1 \sin\theta_1^i}{\hat{n}_k^2} U_k(z)\right|^2$$

Eq. 2.52

The combination of these expressions provide the total MSEFS for p-polarized light:

$$\left\langle E_k^{p2} \right\rangle = \left\langle E_{xk}^{p2} \right\rangle + \left\langle E_{zk}^{p2} \right\rangle$$

Eq. 2.53

With the use of measurable quantities such as the wavelength and the angle of incidence of incoming radiation, thicknesses and optical constants of the different layers in the stratified media, the above equations, when manipulated by a computer program, allow the determination of the MSEFS, thus the optimization of the *in situ* PM-IRRAS experiments. If the MSEFS is calculated for a range of incident angles and electrolyte phase thicknesses for a given wavelength, the maximum value of the MSEFS can be determined and the corresponding angle of incidence and electrolyte thicknesses will give optimum signal for that wavelength region.

2.5.4 Photoelastic Modulation

When the electromagnetic wave passes through an optical element called a linear polarizer, the beam is converted into a well-defined plane polarized wave that retains the plane of polarization unless it is perturbed. In PM-IRRAS experiments, the polarization of the beam is "perturbed" by the photoelastic modulator (PEM), which modulates between p-polarized light and s-polarized light to obtain quantitative information of the adsorbed film at the metal electrode.

In order to optimize the data acquisition procedure and processing, a good understanding of the PEM principles of operation is needed. The PEM makes use of the retardation or acceleration of the electromagnetic wave and its description and demodulation techniques follow this introduction.

2.5.4.1 Principles of Operation of a Photoelastic Modulator

The PEM operates on the principle of the photoelastic effect. Some transparent crystals such as calcite show double refraction depending on their crystallographic orientation. This property is called birefringence. Isotropic materials may display birefringence if their symmetry is distorted due to mechanical stress [28]. Mechanical stress may be externally induced by a PEM; this is known as the photoelastic effect.

The PEM comprises an isotropic crystal that is periodically compressed and extended by a piezoelectric transducer, causing a synchronous variation in the refractive indices along two mutually perpendicular axes of the crystal. When the optical element is stretched and compressed, the indices of refraction of the optical element vary in a sinusoidal manner along the stress axes. This extension and compression causes the components of polarized light along the axes to be phase advanced or retarded with respect to one another. If the refractive index increases following Eq. 2.54, the wavelength of the wave ν decreases since the frequency of the radiation is invariant with respect to the refractive index.

$$n = \frac{c}{\nu}$$

Eq. 2.54

The effects of the PEM on linearly polarized beams are shown in Figure 2.11.

Prior to passing through the PEM, the polarization is 45° with respect to the main axis of the device. When the optical element of the PEM is relaxed there is no change in the polarization, whereas in compression the polarization component parallel to the main axis of the modulator E_{px} travels slightly faster than the vertical component E_{py}, the horizontal component leads the vertical component, resulting in a positive phase shift. Conversely, negative phase shift is obtained if the extension of the optical element happens.

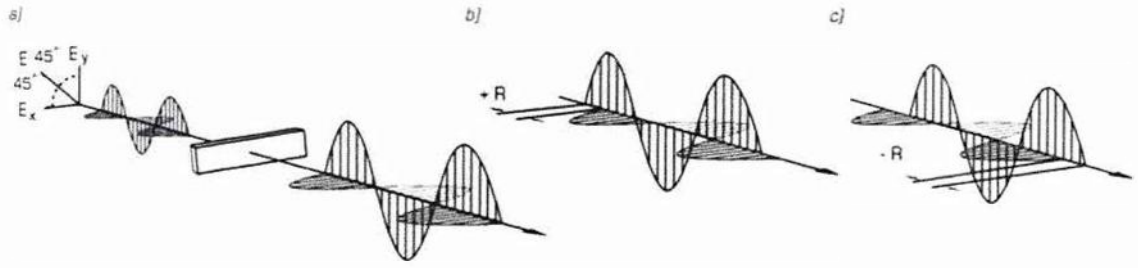

Figure 2.11: Effects of PEM on polarized beam: a) relaxed PEM b) compressed c) extended [35]

The behaviour of the output beam depends on the amplitude of the applied voltage by the piezoelectric transducer. During one modulation cycle, the optical element becomes compressed and after, stretched. The maximum phase retardation or acceleration of the component I_{px} is when it reaches one-half of the wavelength of component I_{py}, thus the polarized radiation switches sinusoidally from 0° to 90° at the extreme of the compression or extension cycle with a frequency twice that at which the optical element is being extended and compressed. This important concept of photoelastic effect can be used in reflection absorption spectroscopy as described in the following section.

2.5.4.2 Quantitative Description of PEM Operation

Figure 2.12 shows a schematic representation of the experimental settings used for polarization modulation spectroscopy.

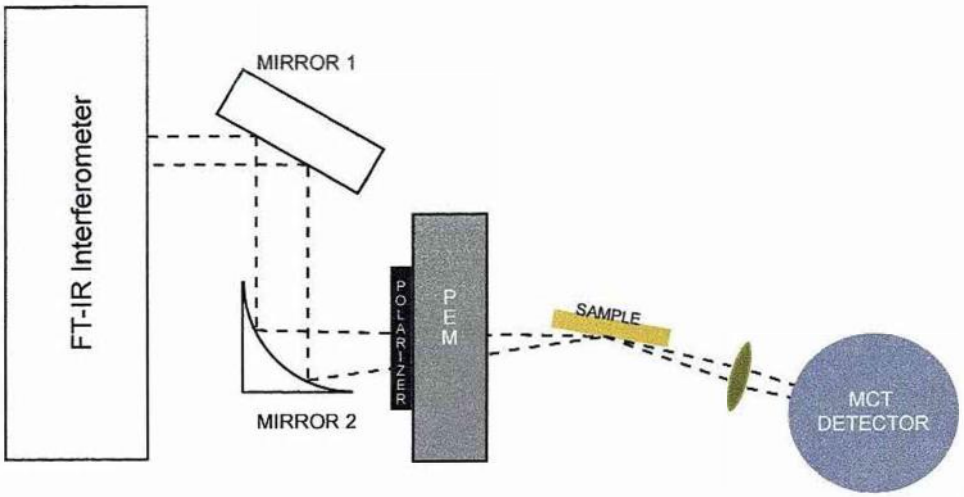

Figure 2.12: Schematic layout used in Polarization Modulation Spectroscopy.

A non-polarized infrared wave that proceeds from the interferometer passes through a linear polarizer after being focused by a parabolic mirror. The polarizer defines a linearly polarized beam in the direction parallel to the optical bench and is represented as I_1 in Figure 2.13.

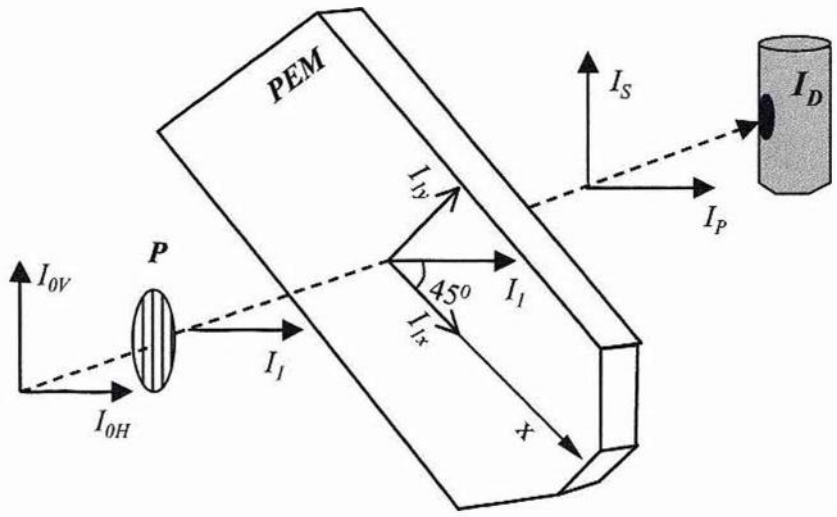

Figure 2.13: Diagram of the orientation of the electric field vector passing through the PEM [29].

The PEM is located between the polarizer and the sample and mounted at 45° with respect to the optical bench plane. As a result of this angle, the linearly polarized light I_1 can be regarded as a composition of two orthogonal components I_{1x} and I_{1y}

oriented along the main axis of the PEM and perpendicular to it, respectively (see Figure 2.13). The PEM imposes a change on the component I_{1x} while the component I_{1y} reminds unchanged. The measured signal at the detector I_D was derived by Hipps and Crosby and is given by Eq 2.55 [36]:

$$I_D(\varphi) = \frac{I_s + I_p}{2} + \frac{I_p - I_s}{2}\cos\left(\frac{\lambda_0}{\lambda}\pi\cos(\omega_m t)\right)$$

Eq. 2.55

where I_p and I_s represent the components of the beam that are oriented parallel and perpendicular to the optical bench, respectively. ω_m is the frequency that the PEM imposed to the isotropic crystal and t is the time. From Eq. 2.55 it can be demonstrated that:

1) $I_D(t) = I_p$

Eq. 2.56

when

$$\omega_m t = \frac{\pi}{2} \pm N\pi \quad \text{in which} \quad N = 0, 1, 2...$$

Eq. 2.57

2) $$I_D(t) = I_s + \frac{I_p - I_s}{2}\left(1 + \cos\left(\frac{\lambda_0}{\lambda}\pi\right)\right)$$

Eq. 2.58

when $\omega_m t = 0 \pm N\pi$ in which $N = 0, 1, 2...$

Eq. 2.59

When condition 2 is satisfied and $\lambda=\lambda_0$, the value of second term in the Eq. 2.58 becomes zero resulting in:

$$I_D(t) = I_s$$

Eq. 2.60

Thus, when the wavelength of the PEM is optimized at λ_0, the polarization of the incident bean periodically changes between p- and s- polarizer light and every 90° of a period either (I_s) and (I_p) is incident at the detector. If however, the wavelength of the PEM differs from λ_0 the beam changes at an angle different than 90° and a beam composed by both p- and s- polarized light is obtained after the PEM.

2.5.5 Polarization Modulation Spectra

The theoretical spectra obtained by using polarization modulation spectroscopy is equal to:

$$\left(\frac{\Delta I}{\langle I\rangle}\right)_{Theoretical} = \frac{I_p - I_s}{\left(I_s + I_p\right)/2}$$

Eq. 2.61

where ΔI is the intensity difference signal and $\langle I\rangle$ is the intensity average signal.

Using an optimized PEM, the signal that reaches the detector alternates between p- and s- polarized light. This signal needs to be decoded to obtain the spectrum corresponding to Eq. 2.61. The technique used for demodulation of these two signals in this thesis is based in the real-time sampling electronics using a synchronous sample demodulator (SSD). This technique was developed by Corn *et al* [37, 38] and uses sampling electronics to detect second or higher order harmonics of the modulator frequency. The measured signal becomes higher at $\lambda=\lambda_0$ approaching to the theoretical maximum given in Eq. 2.61.

The synchronous sampling demodulator technique uses a signal from the PEM controller to sample the signal at the detector when the Eq. 2.57 and Eq. 2.59 are satisfied, generating two signals:

1) The intensity average signal

$$I_D^{Ave}(2\omega_m) = \langle I\rangle + \frac{\Delta I}{2}\left[\frac{1+\cos\varphi_0}{2}\right]$$

Eq. 2.62

2) The intensity difference signal

$$I_D^{Diff}(2\omega_m) = \Delta I\left[\frac{1-\cos\varphi_0}{2}\right]$$

Eq. 2.63

The obtained spectrum using a SSD is expressed as follows:

$$\left(\frac{\Delta I}{\langle I\rangle}\right)_{Experimental} = \frac{\Delta I\left[\frac{1-\cos\varphi_0}{2}\right]}{\langle I\rangle + \frac{\Delta I}{2}\left[\frac{1+\cos\varphi_0}{2}\right]}$$

Eq. 2.64

were φ_0 is the maximum phase shift introduced by the PEM which depends on the applied voltage to the PEM and the wavelength of the polarized radiation.

The experimental absorption spectrum obtained for an investigated sample is superimposed on a periodic background caused by the cosine term but when λ approaches λ_0 Eq. 2.64 approaches Eq. 2.61.

Following demodulation, the spectrum which contains the periodic background needs to be further processed in order to perform quantitative analysis. Data processing followed a methodology described by Buffeteau and is described in detail in Chapter 3.

References:

1. A. P. Girard-Egrot and L. J. Blum, *Langmuir-Blodgett Technique for Synthesis of Biomimetic Lipid Membranes*, Springer US, 2007.

2. M. C. Petty, *Langmuir-Blodgett Films- An Introduction*, Cambridge University Press, Cambridge, 1996.

3. Y. F. Hifeda and G. W. Rayfield, *Langmuir*, 1992, **8**, 197-200.

4. V. M. Kaganer, H. Mohwald and P. Dutta, *Rev. Mod. Phys.*, 1999, **71**, 779-819.

5. P. Dynarowicz-Latka, A. Dhanabalan and O. N. Oliveira, *Adv. Colloid Interface Sci.*, 2001, **91**, 221-293.

6. N. L. Jarvis, *J. Phys. Chem.*, 1965, **69**, 1789-&.

7. I. Langmuir, *J. Am. Chem. Soc.*, 1917, **39**, 1848-1906.

8. I. Langmuir, *Trans. Faraday Soc.*, 1920, **15**, 0062-0074.

9. R. A. Hann, *Molecular structure and monolayer properties*, Plenum Press, New York, 1990.

10. K. B. Blodgett, *J. Am. Chem. Soc.*, 1935, **57**, 1007-1022.

11. H. T. Tien and A. L. Ottova, *J. Membr. Sci.*, 2001, **189**, 83-117.

12. A. Ottova and H. T. Tien, *Bioelectrochem.*, 2002, **56**, 171-173.

13. A. V. Hughes, A. Goldar, M. C. Gerstenberg, S. J. Roser and J. Bradshaw, *Phys. Chem. Chem. Phys.*, 2002, **4**, 2371-2378.

14. L. K. Tamm and H. M. McConnell, *Biophys. J.*, 1985, **47**, 105-113.

15. N. Garcia-Araez, C. L. Brosseau, P. Rodriguez and J. Lipkowski, *Langmuir*, 2006, **22**, 10365-10371.

16. I. Zawisza, X. M. Bin and J. Lipkowski, *Langmuir*, 2007, **23**, 5180-5194.

17. H. Fujiwara, *Spectroscopic ellipsometry: principles and applications*, John Wiley, Chichester, 2007.

18. H. Arwin, *Thin Solid Films*, 2000, **377-378**, 48-56.

19. H. Xie, J. Wei and X. Zhang, *J. Phys.: Conf. Ser.*, 2006, **28**, 95-99.

20. G. Jerkiewicz, *From Electrochemistry to Molecular-Level Research on the Solid-Liquid Electrochemical Interface*, American Chemical Society, 1997.

21. A. J. Bard and L. R. Faulkner, *Electrochemical Methods: Fundamentals and Applications*, John Wiley & Sons.INc, New York, 2001.

22. C. M. A. Brett and A. M. O. Brett, *Electrochemistry. Principles, Methods, and Applications*, Oxford University press, Oxford, 1993.

23. A. Kornyshev, *Electrochemical Interfaces: At the Border Line*, Wiley-Vch, 2007.

24. D. M. Kolb, *Prog. Surf. Sci.*, 1996, **51**, 109-173.

25. J. Richer and J. Lipkowski, *J. Electrochem. Soc.*, 1986, **133**, 121-128.

26. J. Lipkowski and L. Stolberg, *Adsorption of molecules at metal electrodes*, Wiley-VCH, New York, 1992.

27. B. Stuart, *Infrared Spectroscopy: Fundamentals and Applications* John Wiley & Sons, 2004.

28. E. Hecht, *Optics*, Addison Wesley, San Francisco, 2002.

29. V. Zamlynny, PhD Thesis, University of Guelph, 2002.

30. V. Zamlynny and J. Lipkowski, *Quantitative SNIFTIRS and PM IRRAS of Organic Molecules at Electrode Surfaces*, Wiley-VCH Verlag GmbH, 2008.

31. R. W. Hannah, *Sampling Techniques* Wiley, 2001.

32. W. N. Hansen, *J. Opt. Soc. Am.*, 1968, **58**, 380-388.

33. A. Subramanian and L. Rodriguez-Saona, *Fourier Transform Infrared (FT-IR) Spectroscopy*, Academic Press, San Diego, 2009.

34. P. R. Griffiths and J. A. Haseth, *Fourier Transform Infrared Spectrometry*, John Wiley & Sons, Inc., New Jersey, 2007.

35. www.hindsinstruments.com.

36. K. W. Hipps and G. A. Crosby, *J. Phys. Chem.*, 1979, **83**, 555-562.

37. M. J. Green, B. J. Barner and R. M. Corn, *Rev. Sci. Instrum.*, 1991, **62**, 1426-1430.

38. B. J. Barner, M. J. Green, E. I. Saez and R. M. Corn, *Anal. Chem.*, 1991, **63**, 55-60.

CHAPTER 3: MATERIALS AND METHODS

3.1 Introduction

This chapter describes pretreatment procedures, materials and methods that were used in this research. The deposition technique for supported lipid bilayers, electrochemical procedures as well as *ex situ* techniques such as ellipsometry and PM-IRRAS are described in detail in this chapter. Electrochemical PM-IRRAS is also explained. Data acquisition, corrections and manipulations have been developed and described previously elsewhere [1-4] and are only discussed briefly in this following chapter.

3.2 Reagents and Solutions

1,2-dimyristoyl-sn-glycerol-3-phosphocholine (DMPC), 1,2-dimyristoyl-sn-glycerol-3-phosphoethanolamine (DMPE) and 1,2-dimyristoyl-sn-glycerol-3-phospho-L-serine (DMPS) were used for the creation of lipid bilayers supported on gold substrates. These phospholipids are all symmetric lipids with two saturated acyl chains of 14 carbon atoms. The absence of double bonds makes them resistant to the oxidation in the presence of O_2 at the air/solution interface. Comparisons of these phospholipids have also been made with 1,3-bis[1,2-dimyristoyl-sn-glycerol-3-phospho]-sn-glycerol (cardiolipin, CL) which was chosen to represent a mobility-restricted phospholipid.

For the study of electrochemical PM-IRRAS, per-deuterated 1,2-dimyristoyl-D54-sn-glycerol-3-phosphoethanolamine ($DMPE_{D54}$), in which all the hydrogen atoms in the hydrocarbon chains are deuterated, was also needed. All the phospholipids were acquired from Avanti Polar Lipids, Inc (US,via Instruchemie, NL).

Solutions were prepared with no further purification of the phospholipids. These compounds were dissolved with chloroform (HPLC grade, Fisher) to give 2 mg mL^{-1} stock solutions; around 10% of methanol (99.93%, Sigma-Aldrich) was used to solubilise DMPE and DMPS. All water used in this work was purified with a tandem Elix Milli-Q Gradient A10 water system (resistivity > 18 MU cm, TOC < 5 ppb, Millipore, France). Electrolytes were prepared from Suprapur grade sodium fluoride (VWR) and a concentration of 0.1 mol dm^{-3} was used.

3.3 Cleaning Procedures

Very clean glassware was required every time an experiment was carried out. The use of not completely clean glassware may give erroneous results; thus a mixture of concentrated acids was employed for a deep cleaning glass procedure.

Before commencing cleaning with the concentrated acid, the glassware was washed with laboratory detergent to eliminate all traces from previous experiments. The glassware was raised thoroughly with water and dried in an oven. A hot mixture of concentrated acids [1:1 mixture of concentrated H_2SO_4 and HNO_3 (Analytical Reagent Grade, Fisher)] was used for removing all organic contamination. The acids were mixed very carefully in a Pyrex container. The container was placed on a hot plate and the glassware to be cleaned was added to the mixture. The concentrated acid mixture was heated gently, using a watch glass cover to reduce the escape of vapours. After approximately 1 hour, heating was stopped and the acid bath was allowed to cool to room temperature. When the mixture was cool, the material being cleaned was removed and rinsed thoroughly with ultrapure water. If dry glassware was required, it was dried in a dedicated oven where only the very clean glassware was dried, to prevent contamination. Some material was soaked overnight in water to make sure that all the acid was rinsed from the glassware.

The spectroelectrochemical cell also contained several Teflon and Kel-F parts. These were cleaned using a 1:1 NH_3 (Fisher Scientific) and H_2O_2 (AnalaR Normapur 30%) cleaning solution during minimum of an hour. After that period of time, the Teflon/Kel-F parts were removed from the solution and rinsed thoroughly with ultrapure water. As before, some pieces were kept in ultrapure water to make sure the cleaning solution was rinsed from the material being cleaned.

3.4 Langmuir-Blodgett Trough

3.4.1 Preparation of the Langmuir-Blodgett Trough

The equipment used for the formation of monolayers was a Nima 611 Langmuir-Blodgett (LB) trough equipped with a movable PTFE barrier lying across the trough. The surface pressure was measured by the Wilhelmy plate-method. A filter paper was used as standard Wilhelmy plate. The trough was controlled by a computer using Nima TR 7.8 software.

The shallow trough and the barrier were cleaned with chloroform soaked wipes prior to being filled with ultrapure water. The plate was then moved towards the interface until the meniscus connected with it. In this method measurement was made by determining the vertical pull of surface tension on the wetted Wilhelmy plate suspended though the surface via a surface pressure sensor. The result was reported as surface pressure (π).

The temperature of the interface was kept constant (usually 20°C) by passing water from a thermostatic water bath (Grant RC1400G) through channels underneath the trough, heating or cooling down the subphase. The interface was checked for cleanliness by closing the barrier and monitoring the surface pressure. If it remained zero while the barrier was closed, the interface was considered to be completely clean. The barrier was opened and the phospholipid stock solution (Section 1) was spread by dropping the solution over the air/water interface using a microsyringe (SGE). The barrier was opened until the maximum area was available; in this stage there is no interaction between the molecules and the surface pressure was set up to zero. The solvent was allowed to evaporate during a period of 15 min. As the barrier was compressing the molecules at a barrier speed of 25 cm^2 min^{-1}, the computer generated graph showed the *(π)-(A)* isotherm of the added lipid. A scheme of the LB trough is shown in Figure 3.1.

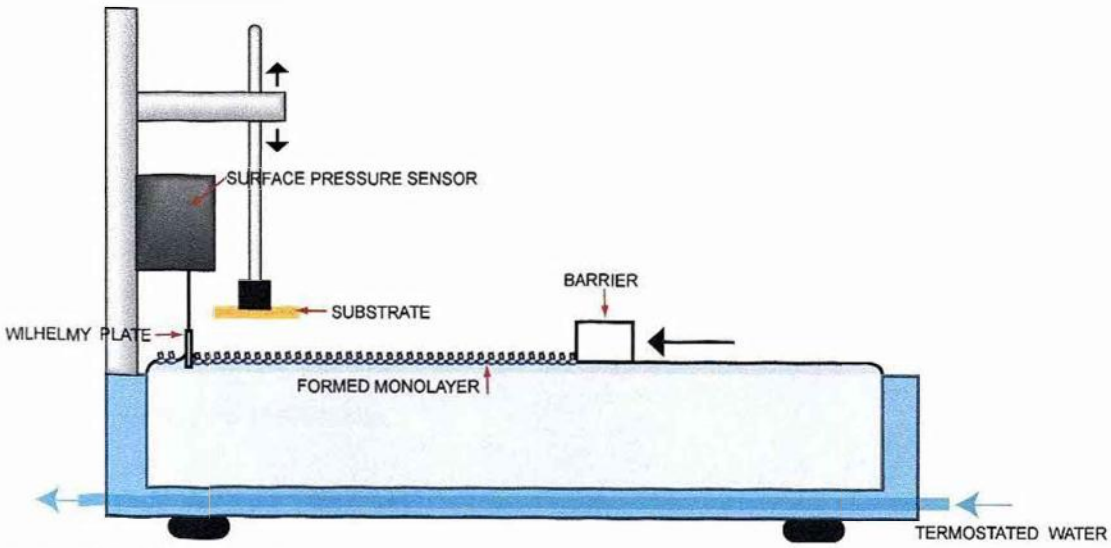

Figure 3.1: Schematic representation of the Langmuir-Blodgett trough.

3.4.2 Langmuir-Blodgett Deposition

The first leaflet of the bilayer was formed using the LB technique. For ellipsometry measurements and *ex situ* PM-IRRAS, Au/Cr/glass slides with 250 nm thickness of gold (Arrandee, Germany) were used as a solid support; the gold was flame annealed with a Bunsen Burner before deposition to ensure the cleanliness of the surface.

The gold substrate was immersed in the ultrapure water and then lipids were spread as described previously. The monolayer was then compressed to a desired transfer pressure at a barrier speed of 25 cm^2 min^{-1}. Once the target pressure was reached, the monolayer was stabilized at this pressure for a few minutes. A surface pressure between 40-50 mN m^{-1} was normally used. The monolayer was transferred to the gold from the air/water interface at a surface pressure of 40 mN m^{-1} when DMPC and CL were deposited and 50 mN m^{-1} when DMPE and DMPS; the speed used for dipping out the gold substrate was 2 mm min^{-1}. The gold covered with the monolayer was dried for about 30 min under argon atmosphere before transferring the second layer.

3.4.3 Langmuir-Schaefer Deposition

After transferring and drying off the first lipid layer, the monolayer formed on the gold was horizontally brought into contact with the preformed monolayer at the air/water interface resulting in the so-called symmetric bilayer.

If asymmetric bilayers were built, the subphase surface was cleaned by vacuum suction, the trough was refilled with ultrapure water and the cleanliness of the subphase was checked, then the new phospholipid was added. The deposition then proceeded as described previously. The second bilayer was also allowed to dry completely before measurements of the bilayer were done.

Figure 3.2 shows the formation of an asymmetric bilayer by using LB and LS deposition on a gold substrate.

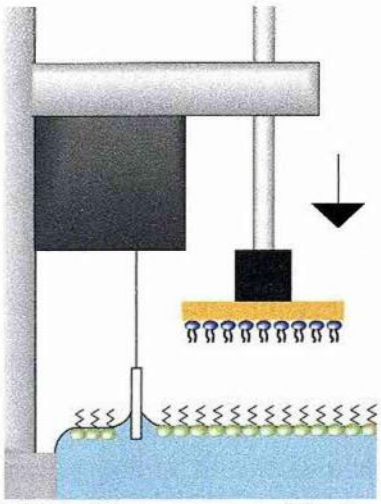

Figure 3.2: Schematic representation of an asymmetric deposition on gold substrate.

3.5 Ellipsometry

The ellipsometer used for the determination of the film thickness was a Horiba Jobin Yvon Uvisel model M200 with a spectral range of 240-850 nm. The light source was a 75 W Xenon arc source set up at an angle of incidence of 70°. The Data Analysis was performed using DeltaPsi2 ellipsometry software.

The substrate used for the deposition of the film was described in section 3.4.2. The sample was placed on the ellipsometer stage, making sure that the beam was incident onto the sample. Looking through the autocolumnator, the crosshairs were aligned by turning the two knobs underneath the stage; this process assures that the sample is perpendicular to the autocolumnator. The height of the stage was adjusted by turning the knob underneath the stage until the light reflected off the sample into the detector reached a maximum. By maximising the intensity of the light, the effect of electronic noise or shot noise (fluctuation in the light intensity) is minimized.

The ellipsometry gave a mean film thickness over a spot area of 1 mm diameter. A minimum of two different areas were measured over at least three different samples and the results were averaged.

A fast acquisition routine was employed to measure the thickness of the film. This routine applied a wavelength step size of 10 nm for a 250-800 nm acquisition range.

A medium of approximation was used to model the optical properties of the film. A single layer model was created using gold as a substrate and an isotropic dispersive material as the deposited film. The wavelength-dependent value of the

complex refractive index is known for the gold substrate. For a description of the organic film, the calculated value of the thickness and refractive index were fitted to the experimental data using the Cauchy transparent dispersion equation model. The iterative fitting was performed using multiple starting values of the film thickness, over the range 0.01 to 10 nm. The optimum value of the thickness was obtained by progressive fittings via a Marquadt algorithm until the error between calculated values and experimental data was minimized.

3.6 Electrochemical Measurements and Instrumentation

The electrochemical instrument used for differential capacitance consisted of a Heka 590 PG potentiostat / galvanostat (Digitimer) and a 7265 DSP lock-in amplifier (Ametek, Germany). All the data were digitized via a plug-in acquisition board (National Instruments) and processed by an in-house software called $SEGM_{suite}$[1].

The experiments were carried out in an all-glass three-electrode cell, using a Au single crystal (MaTeck, Germany of diameter 5 mm and thickness 6 mm) as the working electrode in a hanging meniscus configuration; this ensured that only the (111) face was in contact with the electrolyte. The counter electrode was an Au wire (99.999%, Alfa Aesar, UK); the reference electrode was a saturated calomel electrode (SCE) (Radiometer Analytical), and was connected to the cell via a salt bridge filled with the same supporting electrolyte solution as that of the cell, as shown in Figure 3.3.

The counter electrode and working electrode were cleaned by flame annealing prior to any deposition or electrochemical experiments. The gold single crystal was annealed at dark red heat in the small flame of a Bunsen Burner for a certain amount of time, usually around 7 min was necessary (due the size of the Au(111) [diameter 12 mm and thickness 5 mm] used in electrochemical PM-IRRAS this procedure was longer). During the annealing, the room was darkened for a better assessment of the temperature colour; the flame was moved in and out of the crystal, restricting the heating period to a few seconds to avoid the danger of melting [5, 6]. The hot crystal was covered with a glass Petri dish and cooled in air for around 2 min to minimize the

[1] I wish to express my acknowledge to Dr. Alexei Pinheiro who wrote this software for us.

heat shock. A droplet of ultrapure water was used to protect the surface from any contamination by the air.

The chosen supporting electrolyte solution was 0.1 M NaF (Merck, Suprapur, Germany) because this salt does not show adsorption on gold electrodes. The electrolyte solution was deaerated by purging argon for a minimum of 30 min before commencing measurements, meanwhile and during all the experiment argon was allowed to flow over the solution. The temperature of the cell was maintained at 20°C with a water jacket supplied with water from a thermostatically controlled water bath.

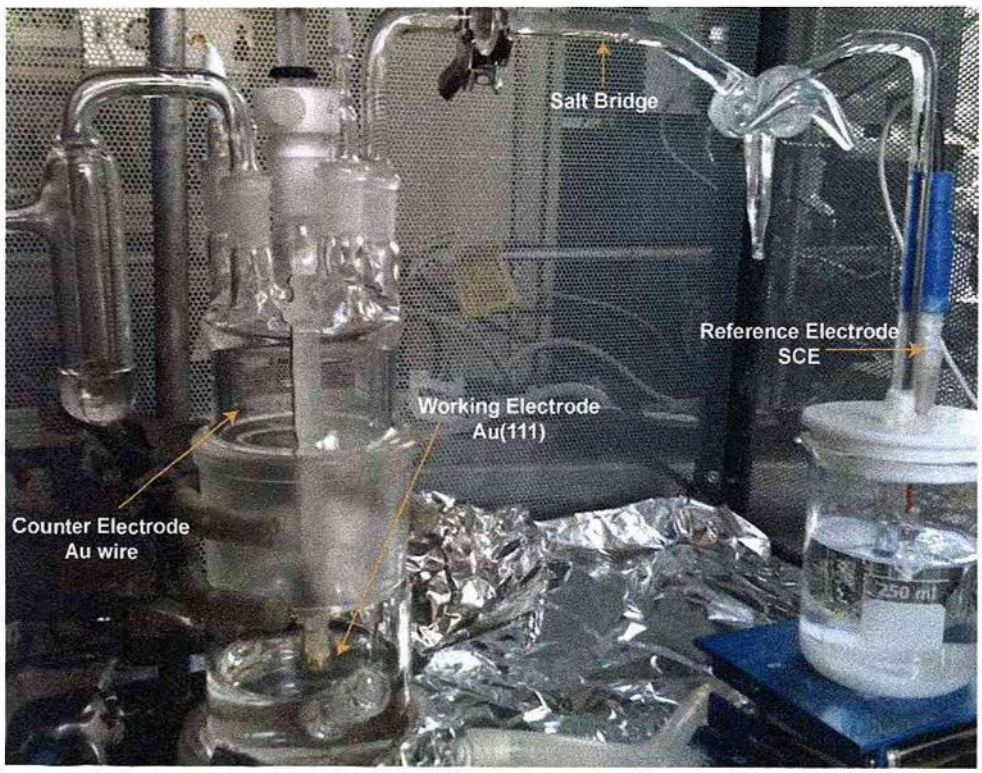

Figure 3.3: Photograph of the electrochemical cell.

The cleanliness of the solution and electrode roughness were checked by the measuring of the cyclic voltammetry and differential capacitance of the supporting electrolyte. If the interface was clean and the electrode showed a smooth surface, the electrode was withdrawn from the electrochemical cell, rinsed and immersed in the water interface of the LB trough for deposition of the bilayer.

Differential capacity (DC) curves were determined using a scan rate of 5 mV s^{-1} and imposing a small sinusoidal perturbation of 5 mV r.m.s. at a frequency of 20 Hz.

A lock-in amplifier was used to measure the in-phase and out-phase components of the alternating current. Differential capacity was calculated assuming a simple series RC equivalent circuit as the model of the electrode-solution interface, according to the equation:

$$C = \frac{i_Q}{E_{ac}\omega}\left[1+\left(\frac{i_R}{i_Q}\right)^2\right]$$

Eq. 3.1

where C is the differential capacity and i_R and i_Q are the real and quadrature (imaginary) components of the measured current, respectivaly. E_{ac} is the root-mean-square voltage and ω is the angular frequency of the applied alternating current perturbation [7].

In chronocoulometry the experimental points correspond to an average of three independent experiments, performed using freshly prepared bilayers. The error bars represent the standard deviation of these three independent measures.

During measurements, the potentiostat was controlled by the computer, which measured the current transients that were used to determine the charge density at the metal/solution interface. Figure 3.4 shows a schematic diagram of chronocoulometry experiments. The gold electrode was held at a base potential E_b = -0.1 V for 60 s. The potential was then stepped to a variable potential of interest E_i, where the electrode was held for a time t_i = 180 s to ensure that maximum adsorption had taken place. Next, the potential was stepped to E_{des} = -1.2 V where the film was totally desorbed from the electrode surface. The current transient corresponding to this desorption process was recorded as a function of time for 150 ms. Finally, the potential was stepped back to E_b for 60 s prior to a new potential step to a different E_i and from E_i to E_{des}.

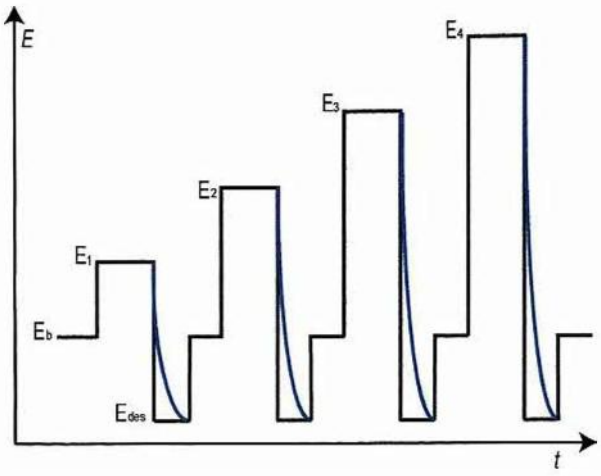

Figure 3.4: Schematic diagram of the chronocoulometric experiment.

The integration of the current transients gives the difference between charge densities at potentials E_i and E_{des}. The current-time curve was integrated using Igor software to give the relative charge density on the metal surface as a function of the adsorption potential. The absolute charge densities were then calculated using the independently determined potential of zero charge (E_{pzc}) value of E_{pzc} = +0.275 V versus SCE. The pzc was determined from differential capacitance measurements in a diluted solution of 5 mM NaF.

For the studies of transmembrane migration of phospholipids in asymmetric bilayers, the bilayer was remade for the next step potential.

3.7 Transmittance Measurements

In order to assist with the quantitative analysis of the bilayers' spectra on Au(111) electrode surfaces, the transmission spectra of randomly distributed molecules in solvents was measured.

A transmission optical cell was employed to obtain the isotropic optical constants of DMPC, DMPE and DMPS in NaF solutions (0.1 M in H_2O and in D_2O). The optical constants of DMPS and DMPE in $CDCl_3$ (Acros Organic) with 10% CD_3OD (isotopic purity 99.8% at% D, Acros) were also calculated. The aqueous solutions were prepared as follows. First, a few millilitres of phospholipid solution were dried by vortexing under argon flow. After a few minutes, complete evaporation of the solvent was achieved. The dry phospholipids were then placed in a vacuum dessicator overnight to remove residual solvent. The dry lipids were resolubilized in

NaF 0.1 M in H_2O or D_2O by sonicating (Branson. Model 1510) the mixture at 40°C until the solution became clear. A slightly alkaline pH was necessary to dissolve DMPE.

Once the lipids were resolubilized, the transmission cell was filled with the solution. The transmission cell was composed of two BaF_2 discs, which were used as windows, and a 25 μm thick Teflon ring was used as a gasket in between them (Figure 3.5). The windows were washed in methanol and then cleaned for 10 min in an ozone chamber (UVO-cleaner, Jetlight Company, Inc. Model 342-220). They were placed in a Teflon housing and clamped between two aluminum brackets. The cell was then mounted in the holder inside the main compartment of the Vertex 80v FT-IR spectrometer (Bruker optics, Germany).

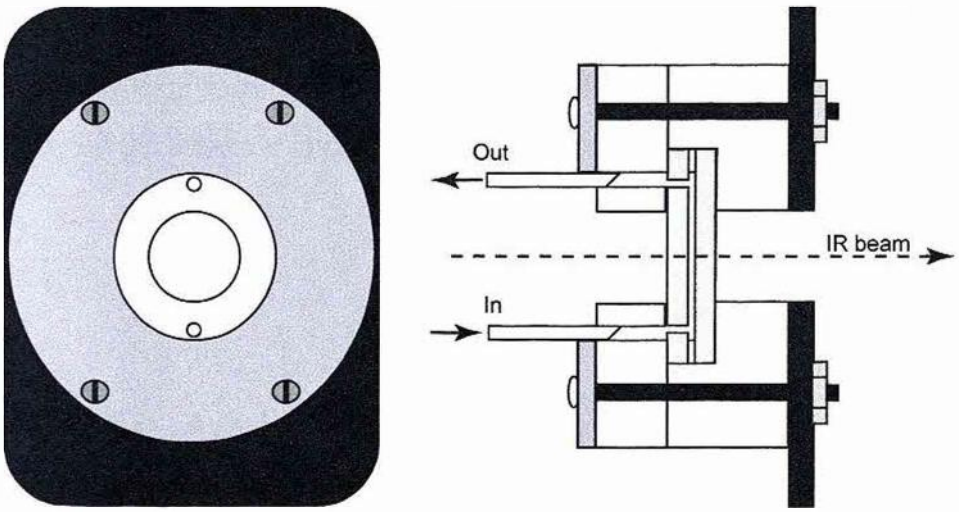

Figure 3.5: Schematic representation of the transmission cell used to determine the optical constants of an analyte in aqueous solution. Adapted from ref [1]

The precise distance between the optical windows was determined by the number of the interference fringes in the spectrum recorded when the transmission cell was empty. An interference pattern arises from the multiple reflections of the bean within the internal walls. Figure 3.6 shows the transmittance of an empty cell (n_∞=1) equipped with BaF_2 windows and a 25 μm thick Teflon spacer.

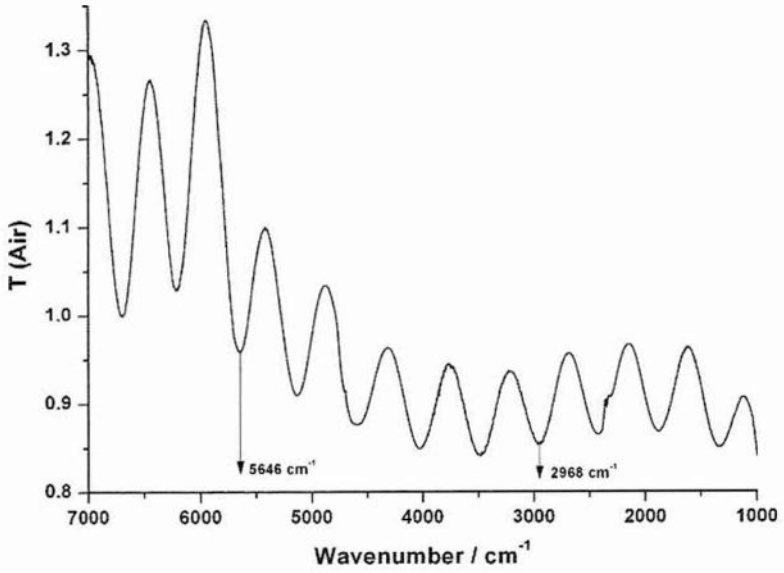

Figure 3.6: Transmittance of the empty transmission cell.

The number of interferences fringes ΔN in in the frequency range $\bar{\nu}_1 - \bar{\nu}_2$ is related to the cell thickness *d* according to the following equation:

$$d = \frac{\Delta N}{2n_\infty(\bar{\nu}_1 - \bar{\nu}_2)}$$

Eq. 3.2

where the n_∞ is the refractive index of the medium within the cell (for air, n_∞=1). In Figure 3.6, the arrows point to an interval that includes 5 full interference fringes. Using Eq. 3.2, one can calculate that the exact thickness of the cell is equal to 9.34 μm.

In order to calculate the optical constants, the cell was first filled with pure solvent (NaF 0.1 M in H_2O or D_2O). A syringe connected to a Teflon tube was used for this purpose. Once the cell was filled, two stopcocks were closed restricting the flow of the solution in or out of the transmission cell, the spectrum was then recorded. In order to minimize the error in the measurement, the same procedure was repeated at least three times and the averaged spectrum was used. The same procedure was followed when the phospholipid solutions were analysed. The exact concentration for each solution was known for later calculations.

To obtain the transmission spectra of the lipid studied, the averaged spectra of a known concentration of the analyte was divided by the averaged spectra of the pure solvent (Eq. 3.3).

$$T = \frac{I}{I_0}$$

Eq. 3.3

Figure 3.7 shows the transmittance of DMPC in NaF 0.1 M in D_2O as an example. The arrows point to an interval between 6804 cm^{-1} and 6135 cm^{-1} that includes 2 fringes; using the previously calculated value of d = 9.34 μm , the average refractive index of DMPC in D_2O could be determined, n_∞ = 1.59.

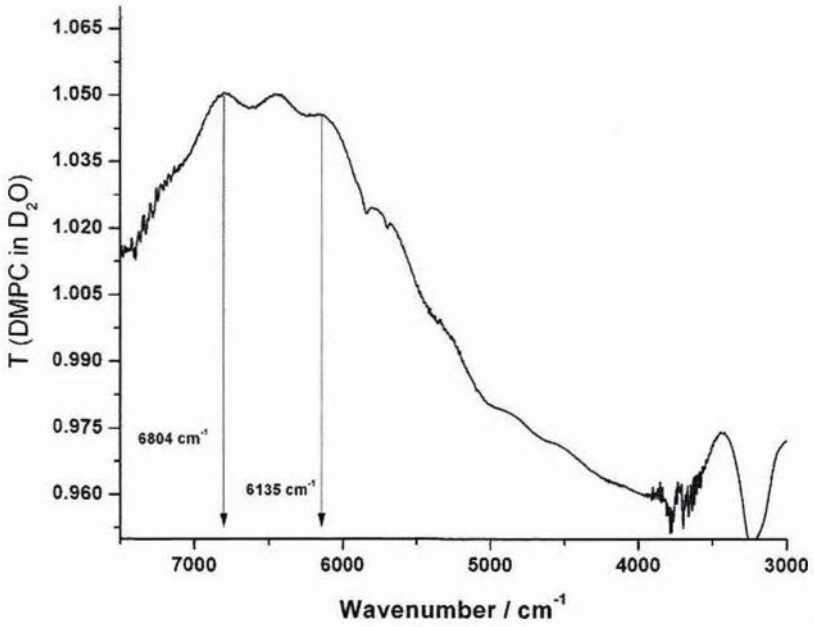

Figure 3.7: Transmittance spectrum of DMPC in 0.1 M NaF in D_2O

The isotropic optical constants were calculated using the transmittance spectra (Eq 3.3), concentration and average refractive index of the lipid of interest, gap thickness of the cell, optical constants of the solvent (D_2O or H_2O) and the BaF_2

windows. Software written by Vlad Zamlynny [2] performed the calculations of the isotropic constants. The calculations consisted of a few steps; these have been described previously [1, 4] and are mentioned below:

1. Approximate values of the attenuation coefficient of the analyte k_i were first calculated from the measured values of the two transmittance spectra using a modified Beer-Lambert law:

$$\frac{I}{I_0} = \exp\left(\frac{-4\pi f_i k_i d}{\lambda}\right)$$

Eq. 3.4

where I and I_0 are the intensities of the radiation transmitted through the thin-layer cell filled with the analyte solution and the pure solvent, d is the thickness of the thin-layer cell, λ is the wavelength of the incident infrared radiation in vacuum and f_i is the volume fraction of the analyte in the sample, which can be calculated by using:

$$f_i = C_i \frac{M_i}{\rho_i}$$

Eq. 3.5

where C_i is the molar concentration, M_i is the molar mass and ρ_i is the density of the analyte in the solution.

2. Approximate values of the refractive index of pure analyte n_i were calculated from the initial estimation of k_i values through the Kramers-Krönig equation:

$$n_i(\bar{\nu}_0) = n_\infty + \frac{2}{\pi} P \int_{\bar{\nu}_1}^{\bar{\nu}_2} \frac{\bar{\nu} k_i(\bar{\nu})}{\left(\bar{\nu}^2 - \bar{\nu}_0\right)} d\bar{\nu}$$

Eq. 3.6

where n_∞ is the average refractive index in the mid-infrared region that represents the contribution to the refractive index of regions removed from any absorption band. P

[2] We are grateful to Vlad Zamlynny for providing us with his software. Inquiries concerning the software should be addressed to vlad.zamlynny@acadiau.ca

indicates that the Cauchy principal value of the integral must be taken because of the singularity at $\bar{\nu} = \bar{\nu}_0$ and $\bar{\nu}_1$ and $\bar{\nu}_2$ are the lower and the upper limits of the spectrum of k, respectively.

3. The following equations Eq. 3.7 and Eq. 3.8 were used for the calculation of the refractive index and attenuation coefficients of the solution

$$\frac{\sum x_i M_i}{\rho} \frac{n^2 - 1}{n^2 + 2} = \sum x_i \frac{M_i}{\rho} \frac{n_i^2 - 1}{n_i^2 + 2}$$

Eq. 3.7

$$\sum x_i \frac{M_i}{\rho} k = \sum x_i \frac{M_i}{\rho} k_i$$

Eq. 3.8

where ρ and ρ_i denote the densities of the solution and the pure component of the i solution, n, k and n_i, k_i are the corresponding refractive indices and attenuation coefficients, x_i is the mole fraction, and M_i is the molar mass of component i.

4. The approximate values of the refractive index and the attenuation coefficient were used as a starting point in the Fresnel equation to calculate the theoretical transmittance spectrum, which was calculated as the ratio of the simulated spectrum corresponding to the analyte solution, and the simulated background spectrum of the pure solvent. Both spectra were calculated using a thin layer of solution, situated between the two optical windows, as the model of the transmission cell. In one case, the layer was represented by the optical constants of the pure solvent and in the other case it had the optical constants of the solution, calculated using Eq. 3.7 and Eq. 3.8.

5. For each wavelength, the attenuation coefficient was perturbed and used to calculate the refractive index, n_i according to Eq. 3.6. Both of these optical constants were then used to calculate the optical constants of the solution using Eq. 3.7 and Eq. 3.8. The attenuation coefficients of the solution were later used to calculate

another theoretical transmittance spectrum using the approach described in Step 4.

6. The theoretical transmittance spectra obtained from step 4 and 5 were compared with the experimental one and a refined spectrum of the attenuation coefficient, k_i was obtained.

7. The refined attenuation coefficients determined in step 6 were used to calculate the improved refractive indices, n_i, using Eq. 3.6 and steps 4 to 7 were repeated, using the refined values of k_i and n_i , until the theoretical spectra deviated from the experimental transmittance by no more than a specified value of precision. The procedure was highly convergent, and two iterations were sufficient to obtain the final set of optical constants (Figure 3.8), yielding the theoretical spectrum within a 1% deviation from the measured transmittance.

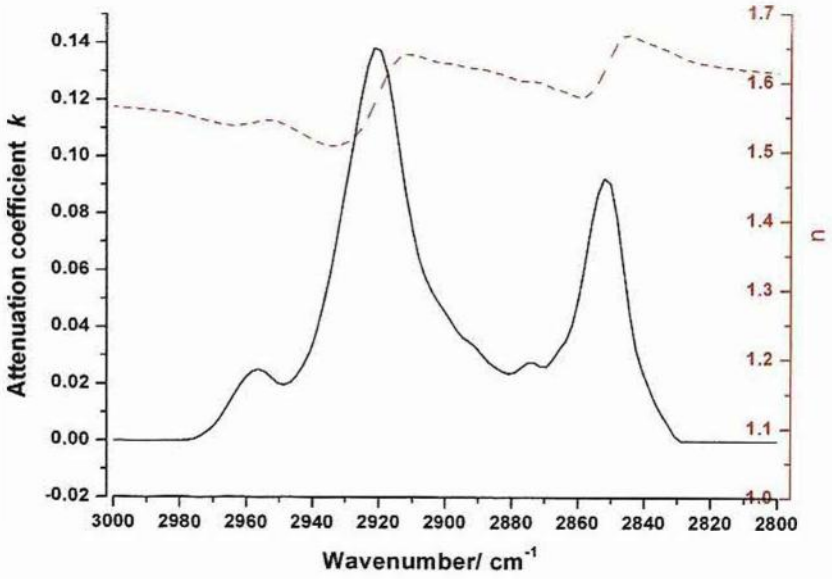

Figure 3.8: Optical constants of DMPC (0.675%) in NaF 0.1 M in D_2O.

3.8 Simulation of PM-IRRA Spectra

The isotropic optical constants obtained for DMPC, DMPE and DMPS in the transmittance experiments can be used to model a film of randomly oriented molecules on gold. This convenient approach was used for the calculation of the simulated polarization modulation spectra because all the transition dipoles of the analyte molecules assume no preferential orientation in space.

The conditions for the simulation (the angle of incidence and the thin cavity thickness in the case of electrochemical PM-IRRAS) were kept the same as PM-IRRAS experiments. The configuration used for the calculation of the reflectivity for the s- and p- polarized light (R_p and R_s) was Au/Phospholipid bilayer/Air2/Air1 at a selected angle of 80° for *ex situ* PM-IRRAS. For electrochemical PM-IRRA spectra, the configuration was Au/Phospholipid bilayer/D_2O[H_2O]/BaF_2 using the predetermined angle of incidence and thin cavity thickness from the actual experiment performed.

The optical constants of the BaF_2 window, Au and the electrolyte were acquired in conjunction with the Fresnel1 software. The author of the software referenced the optical constants from the literature [8-11].

Using Eq. 3.9 the simulation of the theoretical spectra was obtained. How these spectra were integrated and used for the determination of the orientation of organic molecules was explained later in this thesis.

$$\frac{\Delta R}{\langle R \rangle} = \frac{|R_s - R_p|}{(R_s + R_p)/2}$$

Eq. 3.9

3.9 PM-IRRAS

3.9.1 Spectrometer Characteristics

The components of the spectrometer in this research were similarly mounted to that described by Corn *et al.* [12, 13]. The collimated infrared radiation from the spectrometer (Vertex 80v, Bruker Optics) entered a port of an external tabletop optical module (TOM) where the beam was deflected using a flat mirror and was focused using a parabolic mirror. The beam then passed through a static polarizer (Bruker Optics) and a photoelastic modulator (PEM-100, Hinds Instruments, US)

which contained a ZnSe optical head. The PEM and the synchronous sampling demodulator (SSD) (GWC Technologies, US) are the other components of the external modified PMA50 module.

The beam was then reflected by the gold substrate and was refocused by an aspheric ZnSe lens onto the liquid N-cooled MCT-A detector that was fixed to a resolution of 2 cm^{-1}. The detector was rotated along a rail in an angular range of 0-90° in order to set the specific angle necessary for the experiments.

The detector sent the signal to the SSD and simultaneously, a signal double in frequency was sent from the PEM controller which was used as a reference signal and input to the SSD. An oscilloscope was used to phase the SSD with the PEM. The signal was demodulated by the SSD, the outputs being the average and difference signals of the p- and s- polarized radiations which were input into the computer.

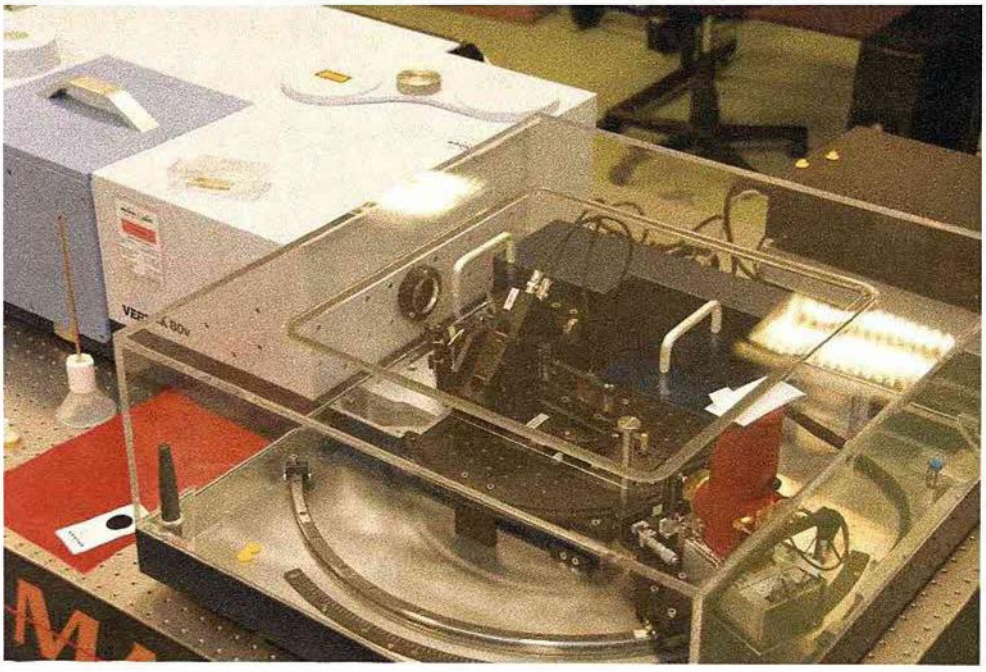

Figure 3.9: PM-IRRA Spectrometer.

3.9.2 Spectroelectrochemical Cell

As mentioned previously, both *ex situ* and *in situ* PM-IRRAS experiments were utilized for the study of films on Au substrates. A phospholipid bilayer deposited on a Au/Cr/glass slide was used to obtain the *ex situ* PM-IRRA spectra. The PEM was set

to half-wave retardation at 2900 cm^{-1} for the C-H stretching region and 1600 cm^{-1} for the C=O stretching region. The angle of incidence employed was 80°.

For *in situ* electrochemical studies, a custom-made spectroelectrochemical cell was used instead of the gold slide. Similar cell designs have been proposed by Seki *et al.* [14], Roe *et al.* [15], Bae *et al.* [16] and Lipkowski *et al.* [4].

The body of the spectroelectrochemical cell comprised a glass tube provided with a water jacket to maintain the electrolyte solution at a constant temperature. The tube was sandwiched between two KelF flanges, each with a circular incision. The flanges fitted with viton square section o-rings and were clamped together with bolts to seal the cell. The optical window was clamped to the front flange with an aluminium block, cushioned with a Teflon insert fitted with a v-shaped groove to match the edge of the prism-shaped window. The block fitted to a guiding groove on a base-plate which facilitated cell alignment.

The working electrode was a 12-mm disc-shaped Au(111) single crystal. This was inserted into a Teflon tube, which was drilled with a hole to connect the gold single crystal to the potentiostat clip with a piece of gold wire. This tube was inserted inside the glass tube by using the hole in the KelF flange situated at the back of the cell body. This allowed the working electrode to be held in place and to be pushed parallel to the optical window. The counter electrode was a gold wire coiled into a ring concentric to the working electrode. A thin tube was used to connect by capillarity a saturated Ag/AgCl reference electrode. All potentials for *in situ* PM-IRRAS experiments were referred to this reference electrode.

The electrode potentials were applied with a potentiostat (Princeton Applied Research 363) controlled by an in-house macro developed by Andrew Burley, a colleague in our research group. This macro used the Opus software to control an output voltage, connected to the external input of the potentiostat, and synchronized the spectral collection with a sequence of desired applied potentials.

The optical window used to focus the incoming laser beam onto the working electrode surface was a BaF_2 equilateral prism (Crystran Limited, Poole, UK). It was washed in ultra pure water and methanol and then cleaned in an ozone UV chamber for 10 min before being assembled in the cell. The prism was held on the centre of the front KelF flange by the aluminium block and the prism was in contact to the

inside of the cell body through a hole in the KelF flange. The working electrode holder fitted through this hole to forma cavity between the electrode and the window, which decreased when the electrode was pushed against the optical window. To ensure the prism did not move and the cell was tightly sealed, four screws were used. Figure 3.10 shows the arrangement of the spectroelectrochemical cell.

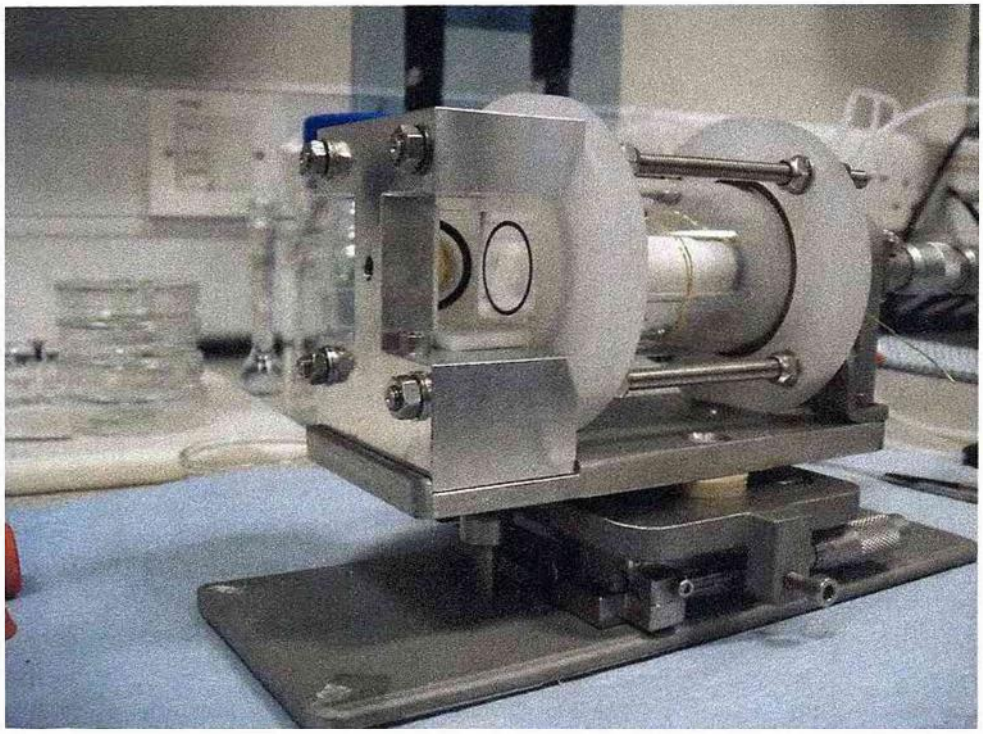

Figure 3.10: Photograph of the Spectroelectrochemical Cell.

The cell was mounted onto a base-plate that contained a micrometer and a screw that regulated the position of the cell in the x-y axes. The base-plate was fixed to the optical table using a pivoting axis that coincided with the focal point of the parabolic mirror. The rotation around this axis was used to set the angle of incidence of the IR beam. Once the intensity of the beam was maximized at the desired angle, the cell was clamped to avoid any change in its position.

The supporting electrolyte was 0.1 M NaF in H_2O or D_2O. The supporting electrolyte was purged for around 1 hour before it was used to fill the cell. In order to fill the cell, the supporting electrolyte was pushed inside the cell using an Argon flow through the reference electrode holder.

3.10 Experimental Conditions Used in PM-IRRAS

3.10.1 Solvent Selection

The supporting electrolyte solution used in electrochemical PM-IRRAS experiments shows very intense absorption bands of the infrared radiation. Based on the positions of these absorption bands, the solvent (either D_2O or H_2O) for each wavenumber region of interest has to be chosen to minimize background absorption. Figure 3.11 shows the major absorption bands of D_2O or H_2O in the mid-infrared region:

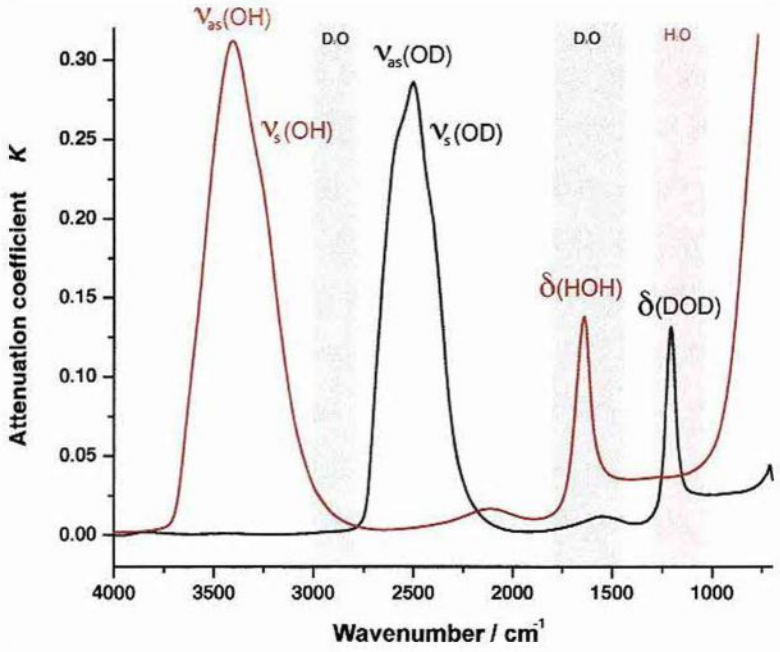

Figure 3.11: Major IR absorption bands for H_2O (red line) and D_2O (black line) and solvent chosen for wavenumber regions studied.

The symmetric and asymmetric O-H stretching vibrations are prominent in the region between 3700 cm^{-1} to 2800 cm^{-1}. The O-D stretching vibrations are shifted to 2700 cm^{-1} - 2100 cm^{-1}. The H-O-H and D-O-D appear at 1600 cm^{-1} and 1200 cm^{-1}, respectively. D_2O was chosen as electrolyte solvent for the following studied infrared regions: C-H stretching vibrations (centred at 2900 cm^{-1}) and C=O ester and amide stretching vibrations (centred at 1600 cm^{-1}). H_2O was used in the spectral region of 1100 cm^{-1} for the study of the asymmetric phosphate stretching vibration and C-O ester stretching vibration (centred at 1200 cm^{-1}) and the symmetric phosphate stretching vibrations (centred at 1000 cm^{-1}).

3.10.2 Angle of Incidence and thin cavity thickness

The intensity of the signal for molecules adsorbed on the metal surface is proportional to the mean squared electric field strength (MSEFS) of p-polarized light [17]. The MSEFS is a function of the incident angle, the convergence angle of the incident beam, the thickness of the thin layer of electrolyte between the electrode and the optical window and the optical constants of all the components of the interface. The convergence angle used in this project was ±5°. The incident angle and the cavity thickness were optimized to obtain the maximum MSEFS at the Au electrode surface.

The MSEFS of p-polarized light can be calculated from the Fresnel equations as outlined in Chapter 2. Using a stratified medium composed by BaF_2, D_2O and Au as the optical window, electrolyte and electrode surface, respectively, the optimum MSEFS was calculated (the example shown are for a C-H stretching region centred at 2900 cm^{-1} and C=O ester stretching vibrations centred at 1600 cm^{-1}). During these calculations, the incident angle was varied from 0° to 90° and the cavity thickness *d* was varied from 0 to 10 μm. In these examples, shown in Figure 3.12 and Figure 3.13, the global maximum of the MSESF is observed at a thin cavity thickness of 2.4 μm and incident angle of 51° for 2900 cm^{-1} and 3.4 μm and incident angle of 61° for 1600 cm^{-1}.

For each wavenumber region studied, the optimum conditions were calculated and are given in Table 3.1.

Table 3.1: Optimum values of the angle of incidence and the thin cavity thickness for each wavenumber studied in this research.

Wavenumber region	*Solvent*	*Angle of Incidence*	*Thin Cavity Thickness*
2900 cm^{-1}	D_2O	51°	2.4 μm
1600 cm^{-1}	D_2O	61°	3.4 μm
1100 cm^{-1}	H_2O	56°	2 μm

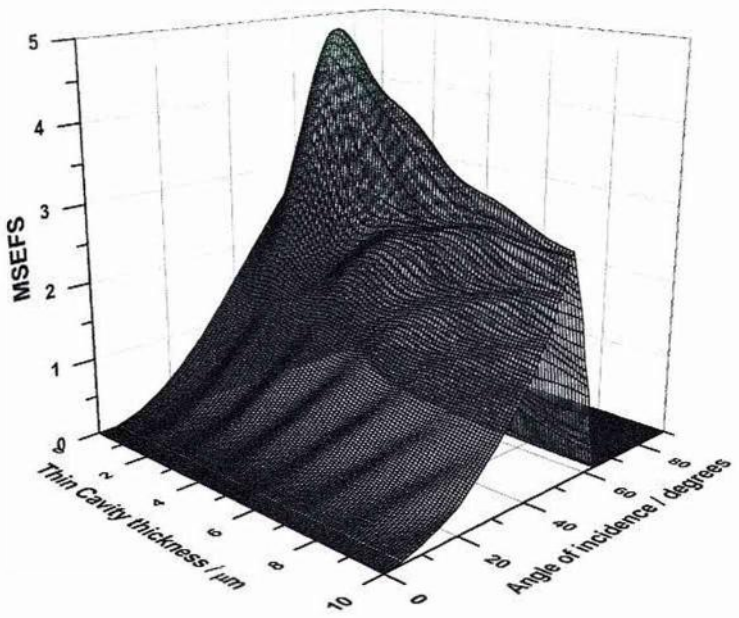

Figure 3.12: MSEFS for p-polarized light at the metal surface as a function of the thin cavity thickness and the angle of incidence for a stratified medium of $BaF_2/D_2O/Au$. Calculated for a convergence beam ±5° at 2900 cm^{-1}.

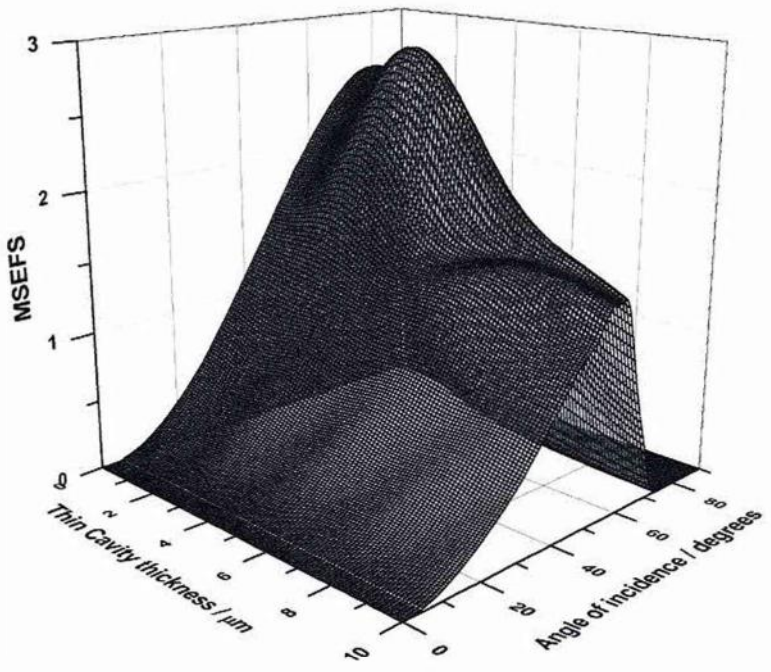

Figure 3.13: MSEFS for p-polarized light at the metal surface as a function of the thin cavity thickness and the angle of incidence for a stratified medium of $BaF_2/D_2O/Au$. Calculated for a convergence beam ±5° at 1600 cm^{-1}.

In practice, the achievement of the optimum incident angle is not very difficult; however, the measurement of the thin cavity thickness with a precision on the order of a fractions of a micrometer is complicated. A procedure developed by Vlad Zamlynny [1, 18] allows the measurement of the thin cavity thickness and the exact angle of incidence using the reflectivity spectra. An overview of this methodology is described below.

This method consists of the comparison of the experimental reflectivity curve with the theoretical reflectivity curve. For the measurement of the experimental reflectivity, first one has to measure the reflectivity R_0 of the empty (dry) cell. The IR beam is totally reflected from the window/air interface thus, R_0 is a good measure of the intensity of the incident beam. After, the cell is filled with the electrolyte and the electrode is pushed against the optical window, forming a thin layer of electrolyte. The reflectivity that is measured now is the reflectivity R of a beam that is transmitted through the BaF_2/solution interface, travels through the thin layer of the electrolyte and is reflected from the electrode surface. The experimental reflectivity is taken as the ratio of R/R_0. Initially the electrode was slightly pushed and the experimental reflectivity was calculated in order to know the relative position of the electrode. Consecutively this procedure was repeated a few times until the final value of the thickness was close to the theoretical value desired.

The theoretical reflectivity $(R/R_0)_T$ is calculated by using the Fresnel equations for a system consisting of three homogeneous phases, BaF_2/D_2O/Au. The thickness of the thin layer cavity (thickness of D_2O layer) and the angle of incidence are the two adjustable parameters. Initial approximate values of the thickness and the angle of incidence, are input into the software, which then determines the values of these parameters that give the best fit to the experimental R/R_0. Although the incident angle is allowed to vary it can be set up quite precisely at the beginning of the experiment. Usually the final value is quite similar to the initial value given.

The reasonably good comparison of the experimental and theoretical reflectivity curve provides the values of the thin cavity thickness and angle used in the experiment. These values if all has been set up correctly, should correspond to the calculated value for the global maximum of the MSEFS.

3.10.3 Additional parameters

For all the IR analysis, the PEM was set to half wave retardation (0.5 λ) and the spectra were collected with a resolution of 2 cm^{-1}. The PM-IRRA spectra were processed using the OPUS program (Bruker, Germany). The aperture of the beam was typically set at 3 mm and 1 mm for the measurement of the spectra and of the reflectivity for the calculation of the cavity thickness, respectively. The signal was checked for the average and difference (R_s-R_p) outputs of the SSD. A gain was set on the SSD to match these signals as close as possible. The gain was typically set to 25.

An open high pass filter and a low pass filter of 10 kHz were used. The zerofilling factor was set to 2, the phase resolution was 16 and the apodization function used was Blackman-Harris 3-term with a Mertz as the phase correction.

In the electrochemical study of bilayers, the initial potential was set initially to E_i = 0.4 V *vs* Ag/AgCl and was stepped in the cathodic direction by 0.1 V increments until the final potencial E_f = -1 V was applied. Each potential was recorded at 4000 scans. The potential was left for 2 min prior to collecting a spectrum, to allow the system to stabilise.

3.11 Spectra Processing

The absorbance $\Delta S(\omega)$ of the infrared beam by the film adsorbed onto a substrate is described by Eq. 3.10:

$$\Delta S(\omega) = \frac{2(I_s - I_p)}{I_s + I_p} \approx 2.3\Gamma\varepsilon = 2.3A$$

Eq. 3.10

where Γ is the surface concentration of the adsorbed species, ε is the decimal molar absorption coefficient of the adsorbed species and A is its absorbance [19].

The spectra obtained from PM-IRRAS analysis using Eq. 3.10 need to be modified due the fact that several artifacts were present. The first is a variation in the retardation that the PEM slowly imposes to the wavelength away from the optimum wavelength set. Secondly, there is a difference in the optical throughput for s- and p-

polarized radiation which must be considered in order to do quantitative analysis. Finally, there is a gradual variation in the background for *in situ* measurements due to the absorption of the infrared radiation by the aqueous electrolyte. The methodology development for the removal of these artifacts from the raw PM-IRRA spectra was introduced for the first time in the studies of the potential-induced reorientation of a film formed by 4-pentadecyl pyridine [19] and these are presented in the following sections.

3.11.1 Removal of PEM artifact

Two signals are obtained after synchronous sampling demodulation from PM-IRRAS measurements: the intensity average $I_A(\omega)$ and the intensity difference $I_D(\omega)$ [12]. These two signals are described by Eq. 3.11 and Eq. 3.12.

$$I_A(\omega) = \frac{\left(I_S(\omega) + I_p(\omega)\right)}{2} + \frac{\left(I_p(\omega) + I_s(\omega)\right)}{2} J_0(\phi_0)$$

Eq. 3.11

and

$$I_D(\omega) = \left|I_S(\omega) - I_p(\omega)\right| J_2(\phi_0)$$

Eq. 3.12

where I_p and I_s are the intensities of p- and s- polarized light, ϕ_0 is the maximum retardation of the incidence radiation imposed by the PEM and $J_0(\phi_0)$ and $J_2(\phi_0)$ are the PEM response functions which are dependent on the slow variation of the retardation imposed by the PEM.

A modification of the method described by Buffeteau *et al.* [20] was used to correct the intensity average $I_A(\omega)$ and difference signals $I_D(\omega)$ for the response of the PEM in order to obtain $\Delta S(\omega)$[19]. This method was used to calculate the cosine J functions. A second static polariser was inserted after the PEM and set to transmit only p-polarized light, thus identical settings as that of the first polariser. The PEM was switched off and the reference spectrum was saved. This spectrum calculated the intensity of the p-polarised light $I_p(\omega)^{cal}$ that passed through the whole optical

bench. Next, the PEM was switched on and polarization modulation spectra were acquired. After demodulation two calibration signals $I_A(\omega)^{cal}$ and $I_D(\omega)^{cal}$ were recorded. Knowing that $I_s(\omega)^{cal}$ in this case is zero Eq. 3.11 and Eq. 3.12 can be rewritten as:

$$I_A(\omega) = \frac{I_p(\omega)^{cal}}{2} + \frac{I_p(\omega)^{cal}}{2} J_0(\phi_0)$$

Eq. 3.13

and

$$I_D(\omega) = I_p(\omega)^{cal} J_2(\phi_0)$$

Eq. 3.14

Hence the response of the PEM can be calculated with Eq. 3.15 and Eq. 3.16:

$$J_0(\phi_0) = 2\frac{I_A(\omega)^{cal}}{I_p(\omega)^{cal}} - 1$$

Eq. 3.15

and

$$J_2(\phi_0) = \frac{I_D(\omega)^{cal}}{I_p(\omega)^{cal}}$$

Eq. 3.16

If the response functions are known, the measured signals $I_A(\omega)$ *and* $I_D(\omega)$ can be corrected as:

$$\langle I(\omega) \rangle = \frac{I_s(\omega) + I_p(\omega)}{2} = I_A(\omega) - \frac{I_D(\omega)}{2}\left(2\frac{I_A(\omega)^{cal}}{I_D(\omega)^{cal}} - \frac{I_p(\omega)^{cal}}{I_D(\omega)^{cal}}\right)$$

Eq. 3.17

and

$$\Delta I(\omega) = I_s(\omega) - I_p(\omega) = I_D(\omega)\frac{I_p(\omega)^{cal}}{I_D(\omega)^{cal}}$$

Eq. 3.18

The spectrum $\Delta I(\omega)/\langle I(\omega)\rangle$ has been corrected from the PEM artifact and is ready for further corrections steps.

3.11.2 Optical Throughput Difference Correction for p- and s- polarized Radiation

Another correction to the raw spectra has to be done due to the induced error of the differential throughputs of the s- and p- polarized radiation [21]. The relation of the difference $\Delta I(\omega)$ and the average $\langle I(\omega)\rangle$ signals with respect the intensities of the s– and p– polarized light is defined in the following way:

$$\Delta I(\omega) = \left|I_s - \gamma I_p\right|$$

Eq. 3.19

$$\langle I(\omega)\rangle = \frac{\left(I_s + \gamma I_p\right)}{2}$$

Eq. 3.20

where $\gamma = C_p/C_s$ is the radio of the throughput of the experimental set up for s- and p-polarized radiation. If Eq. 3.19 and Eq. 3.20 are rearranged, one can obtain:

$$I_s = \frac{\Delta I(\omega)}{2} + \langle I(\omega)\rangle$$

Eq. 3.21

$$I_p = -\frac{1}{\gamma}\left(\frac{\Delta I(\omega)}{2} + \langle I(\omega)\rangle\right)$$

Eq. 3.22

Then, the corrected polarization modulation spectra can be represented as:

$$S(\omega) = \frac{|I_s - I_p|}{\frac{I_s + I_p}{2}} = 2\frac{(\gamma+1)\Delta I(\omega) + 2(\gamma-1)\langle I(\omega)\rangle}{(\gamma-1)\Delta I(\omega) + 2(\gamma+1)\langle I(\omega)\rangle}$$

Eq. 3.23

The value of γ was calculated experimentally by performing the ratio of the spectra recorded when the static polarizer was set to s- and p- polarized light. In this research the value of used for γ was 1.01.

3.11.3 Background subtraction

During electrochemical PM-IRRAS experiments the broad absorption band of the infrared radiation by the aqueous electrolyte slowly varies with the applied potential or time due to small changes within the thin layer cavity. This condition makes the PM-IRRA spectra to be superimposed on top of a large and not always similar background for in *in situ* measurements.

To remove the background, a similar procedure to that published by Barner *et al.* [12] was developed by Zamlynny [1]. In this method, a baseline is created using OriginPro8.5 software for the experimental spectra using the spline interpolation. It is necessary for the correct interpolation the knowledge of the position of the vibrations band caused by the analyte. Usually the same number of points were chosen and snapped into the spectra to avoid errors from the background correction.

Once the background was subtracted from the spectra, as shown in Figure 3.14, the PM-IRRA spectra were integrated to calculate the peak areas, which were used for the calculation of the orientation of the phospholipids on the Au(111) surface.

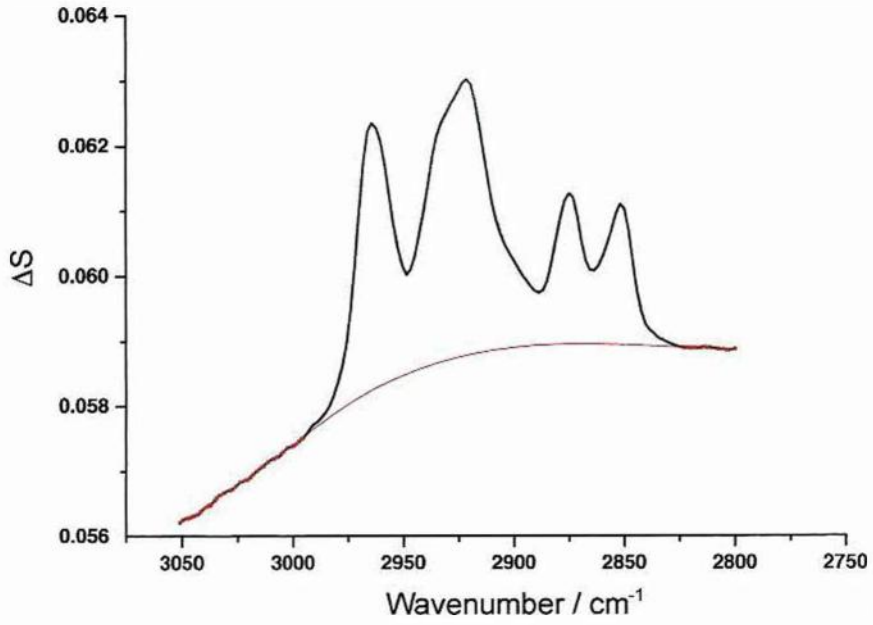

Figure 3.14: Spline interpolation (dash line) method on a raw PM-IRRA spectrum of a DMPC bilayer on a Au(111) surface.

3.11.4 Modelling the Infrared Spectra

After removal the background of the PM-IRRA spectra, modelling was necessary in order to extract quantitative information for molecular orientation determination. OriginPro8.5 software was used for this propose. The auto-find peak option within the peak analyser was used as an initial guess in the location of the peaks. Manual editing was also used to localize some bands such as Fermi resonance bands.

Once the number and position of the band were obtained an algorithm that varies the parameters of the chosen model was used to fit the model within the minimum error. For a very good fit, R-squared was approximately 1.

Usually, the infrared spectra of liquids has been modelled using a Lorentzian function by different authors but the Voigt function was used in this research. This profile takes into account some induced Gaussian character (broader bands) in the sample when the disorder within the bilayer is increased [22].

Once the spectra are modelled or deconvoluted (as some authors called this procedure), the integrated peak intensity is used to calculate the angle between the surface normal and the transition dipole of that specific vibration.

3.11.5 Molecular Orientation

Determination of the molecular orientation on substrates from processed spectra involved the comparison of the experimental spectra with the simulated spectra of those molecules using the isotropic optical constants determined from transmission experiment.

The integrated intensity of the absorption band of linearly polarized light of molecules on a reflective substrate is proportional to the square of the absolute value of the product between the transition dipole momentum μ and the electric field E of the photon. This can be expressed as:

$$\int A d\nu \propto |\mu \cdot E|^2 = \cos^2\theta |\mu|^2 \langle E^2 \rangle$$

Eq. 3.24

where θ is the angle between the directions of the electric field of the photon and the absolute value of the transition dipole of a vibration in the molecule, $|\mu|^2$ is the absolute value of the transition dipole moment and $\langle E^2 \rangle$ is the mean squared electric field strength of the photon.

The direction of the p-polarized radiation at the metal surface is always normal to the surface thus, the surface normal and the transition dipole moment describes the angle θ. The orientation of molecules adsorbed at the interface can be determined using the methodology known as the absolute method. It is based on the calculation of the spectrum for randomly oriented molecules for the same angle of incidence and cavity thickness as the values used for the experimental spectra (section 3.8). For randomly oriented molecules it is known that $cos^2\theta$ =1/3, thus using Eq. 3.25 one can calculate the experimental orientation of the molecules at the interface.

$$\cos^2\theta = \frac{1}{3}\frac{A_{exp}}{A_{calc}}$$

Eq. 3.25

where A_{cal} is the integrated intensity of the band from the simulated spectrum obtained for randomly oriented molecules using the optical matrix method and A_{exp} is the integrated intensity of a band from *ex situ* or *in situ* PM-IRRAS experiments.

When the hydrocarbon chains are fully extended as in trans-conformation, the direction of the transition dipole of the symmetric and asymmetric methylene stretch are in the plane of the methylene group that is perpendicular to the line of the fully extended all-trans hydrocarbon chain. Because these 3 directions are perpendicular, the knowledge of $\theta_{\nu as}$ and $\theta_{\nu s}$ leads one to the calculation of the tilt formed by the hydrocarbon chains using the equation [23]:

$$\cos^2\theta_{\nu_{as}} + \cos^2\theta_{\nu_s} + \cos^2\theta_{Chain} = 1$$

Eq. 3.26

It is important to comment that Eq 3.26 is only applicable when the hydrocarbon chains are fully extended; if the bilayer contains many gauche conformers, this equation can be used only as approximation.

References:

1. V. Zamlynny, PhD Thesis, University of Guelph, 2002.
2. X. Bin, PhD Thesis, University of Guelph, 2005.
3. C. L. Brosseau, PhD Thesis, University of Guelph, 2007.
4. V. Zamlynny and J. Lipkowski, *Quantitative SNIFTIRS and PM IRRAS of Organic Molecules at Electrode Surfaces*, Wiley-VCH Verlag GmbH, 2008.
5. N. Batina, A. S. Dakkouri and D. M. Kolb, *J. Electroanal. Chem.*, 1994, **370**, 87-94.
6. D. M. Kolb, *Prog. Surf. Sci.*, 1996, **51**, 109-173.
7. D. Pletcher, R. Greef, R. Peat, L. M. Peter and J. Robinson, *Instrumental Methods in Electrochemistry*, Horwood Publishing, Chichester, 2001.
8. E. D. Palik, *Handbook of Optical Constants of Solids*, Elsevier, London, 1998.
9. M. A. Ordal, L. L. Long, R. J. Bell, S. E. Bell, R. R. Bell, J. R. W. Alexander and C. A. Ward, *Appl. Opt.*, 1983, **22**, 1099-1119.
10. A. N. Rusk, D. Williams and M. R. Querry, *J. Opt. Soc. Am.*, 1971, **61**, 895-903.
11. J. E. Bertie, M. K. Ahmed and H. H. Eysel, *J. Phys. Chem.*, 1989, **93**, 2210-2218.
12. B. J. Barner, M. J. Green, E. I. Saez and R. M. Corn, *Anal. Chem.*, 1991, **63**, 55-60.
13. M. J. Green, B. J. Barner and R. M. Corn, *Rev. Sci. Instrum.*, 1991, **62**, 1426-1430.
14. H. Seki, K. Kunimatsu and W. G. Golden, *Appl. Spectrosc.*, 1985, **39**, 437-443.
15. D. K. Roe, J. K. Sass, D. S. Bethune and A. C. Luntz, *J. Electroanal. Chem.*, 1987, **216**, 293-301.
16. I. T. Bae, X. Xing, E. B. Yeager and D. Scherson, *Anal. Chem.*, 1989, **61**, 1164-1167.
17. M. Moskovits, *J. Chem. Phys.*, 1982, **77**, 4408-4416.
18. N. Li, V. Zamlynny, J. Lipkowski, F. Henglein and B. Pettinger, *J. Electroanal. Chem.*, 2002, **524-525**, 43-53.

19. V. Zamlynny, I. Zawisza and J. Lipkowski, *Langmuir*, 2003, **19**, 132-145.

20. T. Buffeteau, B. Desbat and J. M. Turlet, *Appl. Spectrosc.*, 1991, **45**, 380-389.

21. T. Buffeteau, B. Desbat, D. Blaudez and J. M. Turlet, *Appl. Spectrosc.*, 2000, **54**, 1646-1650.

22. J. Chalmers and P. Griffiths, *Sample Characterization and Spectral Data Processing* Wiley, 2001.

23. J. Umemura, T. Kamata, T. Kawai and T. Takenaka, *J. Phys. Chem.*, 1990, **94**, 62-67.

CHAPTER 4: ISOTHERMS, ELLIPSOMETRY AND EX SITU PM-IRRAS

4.1 Phase Behaviour of Pure Phospholipids

4.1.1 DMPC

The π-A isotherm of DMPC at 20°C, presented in Figure 4.1, shows that the molecules exist predominantly in the liquid state. A phase transition from liquid expanded (LE) to liquid condensed (LC) was observed at a surface pressure below $\pi \approx 40$ m Nm^{-1}. At higher surfaces pressures than 40 mN m^{-1} the molecules are in a LC phase. DMPC collapses at a surface pressure of 50 mN m^{-1}. The limiting surface area per molecule is derived from an extrapolation of the very steep part of the isotherm to zero pressure. For DMPC this gave a limiting area per molecule of 49 $Å^2$, in agreement with previous studies [1, 2]. The discrepancy, within 1-3% in the limiting area per molecule in different experiments is typical and due to uncertainties in solution concentration and deposited volume.

The thermostatic water bath was set to 15°C, 17°C, 20°C and 24°C for temperature effect studies on DMPC. 30 μL of phospholipid stock solution was added to the interface when it had reached the required temperature. The solvent was allowed to evaporate and a compression isotherm was obtained. The isotherm was stopped before the collapse to avoid lipid losses. The barrier was then opened and the next temperature was set. A waiting time was necessary for the interface to reach the new temperature. A comparison of isotherms of DMPC at different temperatures is given in Figure 4.2. Increases in the area per molecule of DMPC were induced by higher temperatures due to changes in the fatty acyl chain. When the temperature increases, lipid molecules exhibit changes in the hydrocarbon chain indicating the presence of some type of phase transition. This transition involves disordering of the hydrocarbon chains. At the melting transition temperature (T_m = 24°C for DMPC), the lipids change from a more ordered gel state to a more fluid disordered state. Heimburg in 2000 described a lipid pre-transition below this chain-melting transition, clearly visible for phosphatidylcholines [3, 4]. This pre-transition was associated with the formation of periodic ripples on the membrane surface. In the transition regime the lipids could increase their area by about 24% (for DPPC [5]). This area increase was due to the disruption of the lattice order in a bilayer when lipids melt independently.

The isotherms shown in Figure 4.2 support the idea that during the pre-transition, some degree of chain melting of DMPC has taken place. This chain melting was coupled with changes in the limiting area per molecule and thus different isotherms can be observed when DMPC is studied at different temperatures.

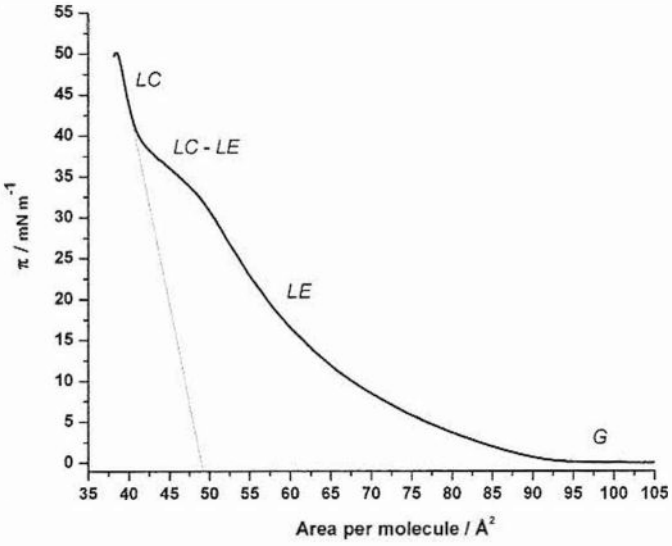

Figure 4.1: π - *A* isotherm of DMPC at 20°C; 30 μL (0.01011 g in 5 mL); barrier speed of 25 cm^2 min^{-1}.

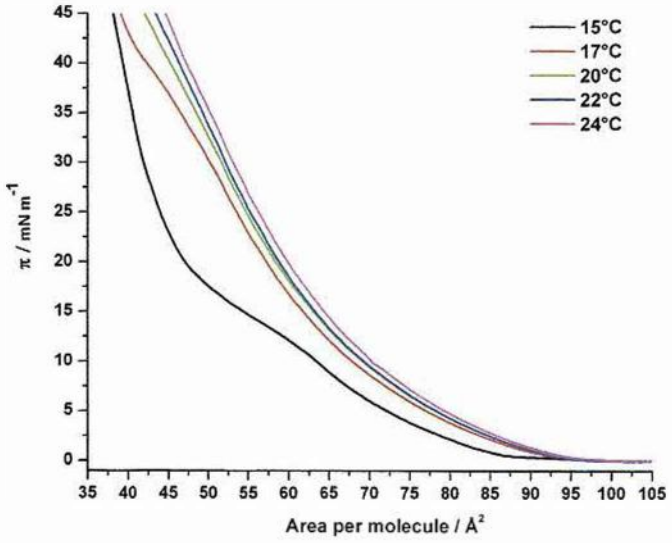

Figure 4.2: π - *A* isotherm of DMPC of DMPC at different temperatures. 30 μL (0.01011 g in 5 mL); barrier speed of 25 cm^2 min^{-1}.

4.1.2 DMPE

The isotherm of DMPE at 20°C, presented in Figure 4.3, shows that the surface pressure started increasing at around 80 Å^2, reaching a surface pressure of 4 mN m^{-1} at ~70 Å^2. The plateau at $\pi \approx 5$ mN m^{-1} is a phase transition from the LE to the LC state. There is a large range of surface pressure in which DMPE exists in a LC state. The molecules in this phase have the chains fully extended but tilted at an angle; a decrease of the surface area can be observed at surfaces pressures higher than 30 mN m^{-1}, which is caused by a decrease of the tilt angle. DMPE collapses at a surface pressure of 55 mN m^{-1}. The limiting area per molecule of DMPE after extrapolation is 43 Å^2, in agreement with previous studies [6].

The thermostatic water bath was set to similar temperatures as DMPC to compare the behaviour of DMPC with a phospholipid with higher T_m. In this comparison, DMPE was used due to its $T_m = 47.7$°C [7]. Figure 4.4 shows π - A isotherms of DMPE at different temperatures. At low temperatures (15°C) the LE state disappears and a direct transition from G to S state takes place; no phase transition between LE and LC is observed. With an increase in the temperature, the LE state is more noticeable and the π at which the LC-LE phase transition occurs increases. This effect may be understood by considering the forces between the molecules in the floating monolayer. At temperatures of 17°C or greater, the fluidity of the monolayer increases, thus different molecule conformations can be visible. A decrease in the temperature leads to less thermal motion in the monolayer, tending to condense the film from the G phase without observing any transitions to the LC phase [8].

The transition from the LE to a LC is connected with an inflection point at a lateral pressure π_c followed by a pronounced plateau, which becomes shorter at higher temperatures. As the temperature increases the slope of the plateau increases slightly so that it is not exactly zero. Theoretical models for two dimensional phase transitions such as LC-LE were generated by Marcelja in 1974; a qualitative agreement is found between them and our experimental data [9].

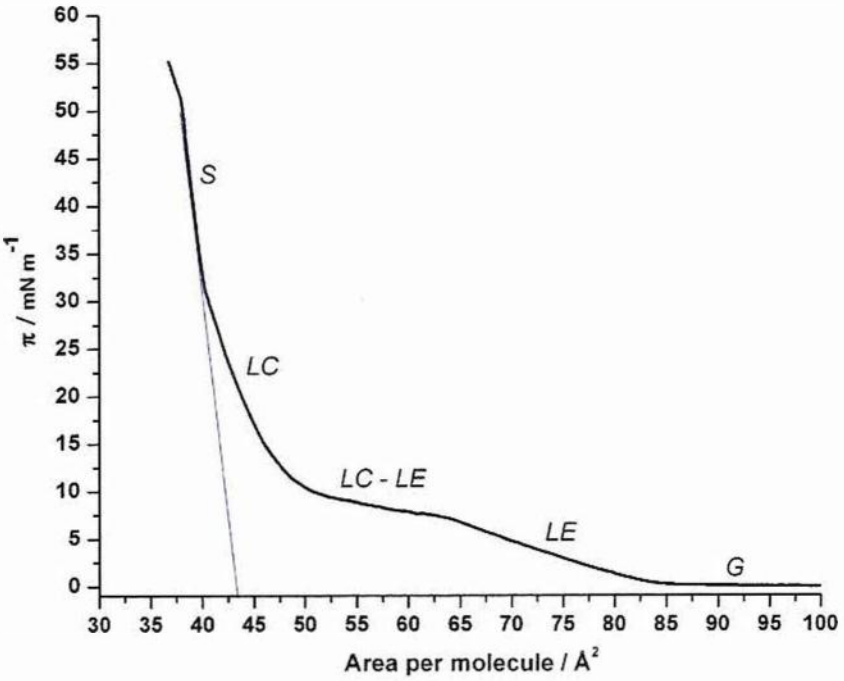

Figure 4.3: π - A isotherm of DMPE at 20°C; 30 μL (0.01009 g in 5 mL); barrier speed of 25 cm^2 min^{-1}.

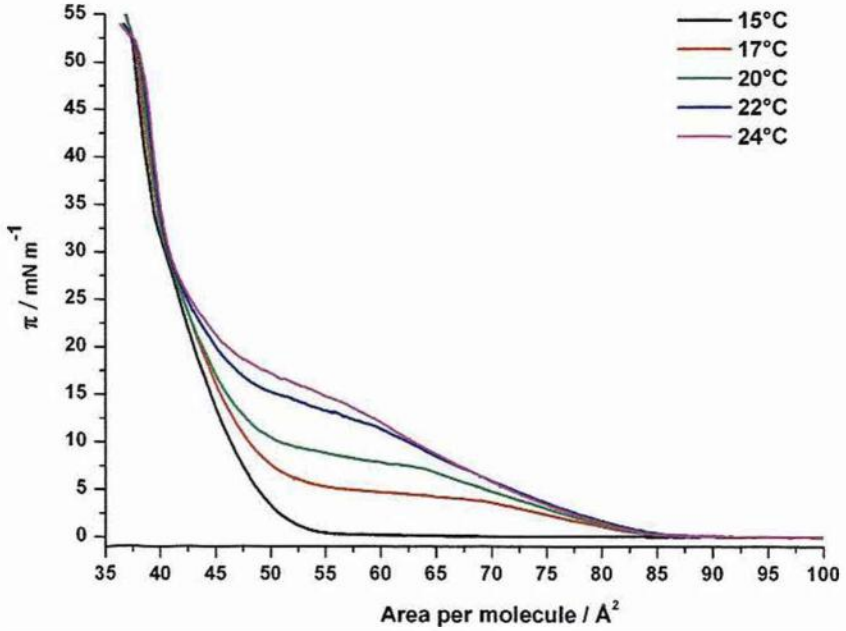

Figure 4.4: π - A isotherm of DMPE at different temperatures. 30 μL (0.01009 g in 5 mL); barrier speed of 25 cm^2 min^{-1}

4.1.3 DMPS

The π-*A* isotherm of DMPS is shown in Figure 4.5. In the compression DMPS shows the G, LC and S phases but an LE phase seems to be absent. Similar behaviour is shown by DMPE at 15°C. Upon compression, DMPS reached the smallest limiting area per molecule with a value of 41 $Å^2$. This indicates that DMPS is more compressible than DMPC, in contrast to the intuitive notion that repulsive interactions between neighboring charged headgroups should expand the area per DMPS molecule. The formation of direct hydrogen bonds between the PO_4^- and the NH_3^+ of adjacent lipid molecules and the bond of COO^- with a remaining Na^+ counterion from the original lipid could explain the reduction of the electrostatic repulsions and the increase in the attractive force between headgroups, giving an area per molecule for DMPS smaller than DMPC [10-13].

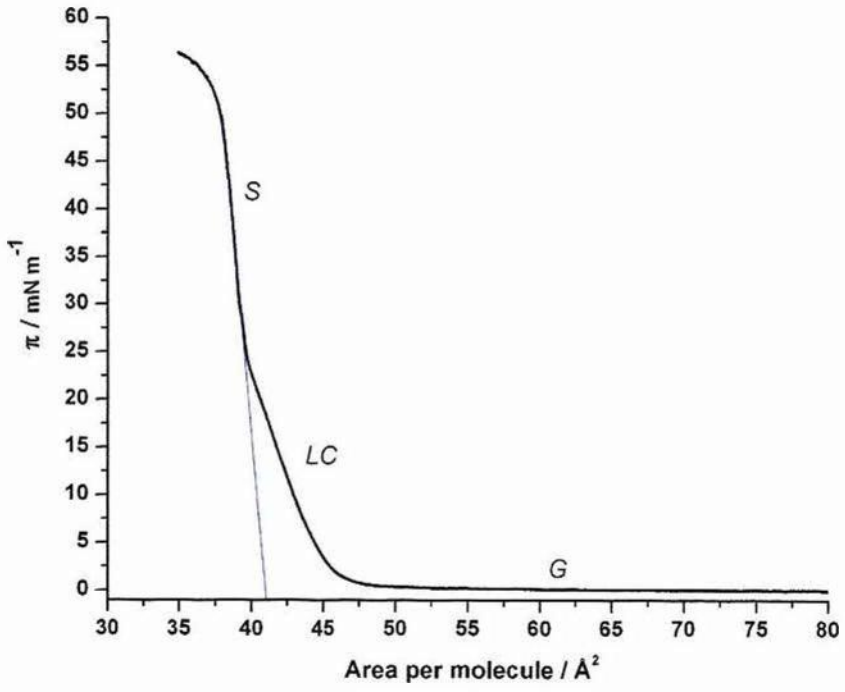

Figure 4.5: π - *A* isotherm of DMPS at 20°C; 40 μL (000996 g in 5 mL); barrier speed of 25 cm^2 min^{-1}.

4.1.4 Cardiolipin

Cardiolipin (CL) exists in a S state over a large range of surface pressures. The isotherm for CL is presented in Figure 4.6. A pronounced plateau similar to that of DMPE and characteristic of the LC-LE transition is also observed in the compression isotherm of CL at about 1 mN m^{-1}. Upon further compression a kink around 11 mN m^{-1} appears in the isotherm, indicating different compressibility above and below this surface pressure. It can be interpreted as a second order phase transition from the LC phase to S phase. At such surface pressures, grazing incidence X-ray diffraction studies confirmed that the CL monolayer is in the S phase, described as untilted and hexagonal. The limiting area per molecule of CL is 81.3 $Å^2$, in agreement with previous studies [14]. This value is higher than the quantified values for DMPC and DMPE due to the large tail region comprising four fatty acids. Due to the small size, the single glycerol headgroup barely accounts for this surface area [15].

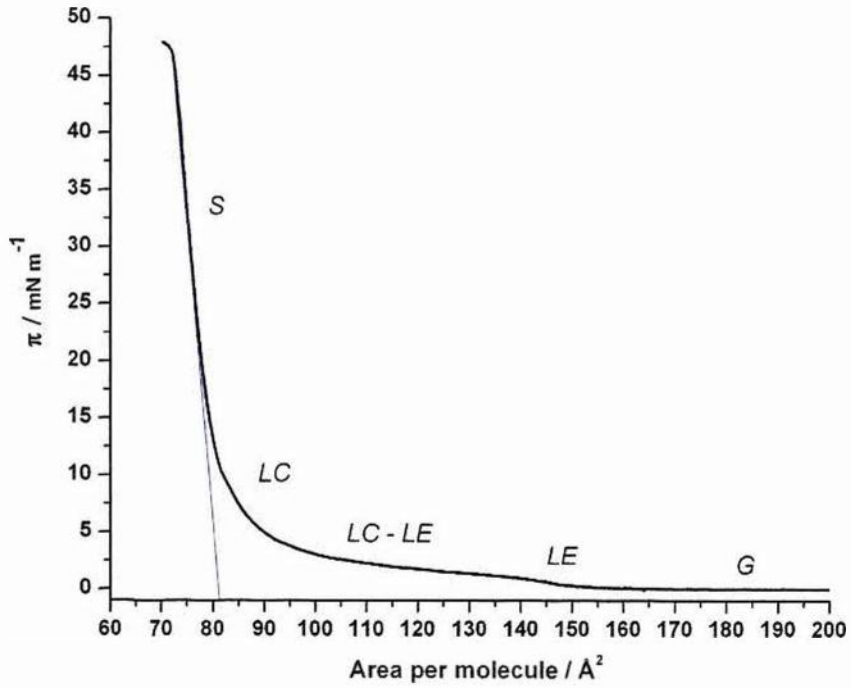

Figure 4.6: π - A isotherm of CL at 20°C; 60 μL (0.00205 g in 2 mL); barrier speed of 25 cm^2 min^{-1}.

4.2 Film Thickness

Depending on the molecular structure of the phospholipid, different thickness values were observed. The data from the thickness of LB monolayers and LBLS bilayers are presented in Table 4.1.

Table 4.1: Thicknesses of phospholipid monolayers and bilayers.

	DMPC	*DMPE*	*DMPS*	*CL*
Monolayer on Au / nm	2.4 ± 0.3	2.6 ± 0.5	2.7 ± 0.5	3.6 ± 0.9
Bilayer on Au / nm	5.7 ± 0.2	7.4 ± 0.4	7.4 ± 0.6	8.2 ± 0.7

The data measured by ellipsometry for CL showed a maximum film thickness of 3.6 ± 0.9 nm for a monolayer, in agreement with reported AFM studies [16] and a 8.2 ± 0.7 nm for a deposited bilayer on Au substrate at 40 mN m^{-1}.

If the phospholipids are organised in an upright standing configuration, the next largest monolayer thickness would be expected for DMPC, owing to its larger headgroup. The DMPC headgroup has volume 319 $Å^3$, compared with 246 $Å^3$ for DMPE and 244 $Å^3$ for DMPS; the volume of the chain is the same for all of them ~732 $Å^3$ [11]. In order to accommodate the hydrocarbon chains to a very large headgroup, which is the case for DMPC, it is required for the DMPC molecules to tilt the chains with respect to the plane in which the molecule is adsorbed. The hydrocarbon chains could tilt at different angles, which would have an effect on the thickness of the film: the more the DMPC molecules are tilted the thinner the film is. For DMPE and DMPS, the hydrocarbon chains are perpendicular to the headgroup, thus the thickness values for DMPS and DMPE films are practically the same due to their similar molecular volume.

The thickness of DMPE and DMPS bilayers are higher than a double monolayer. This effect may be explained by the different conformations assumed by the lipids in contact with the gold and those in contact with the air due to the different interactions of the polar head group with the different environments. It has been reported how a bilayer can assume a spontaneous curvature, increasing the thickness and minimizing its free energy; this could be the case in bilayers which the thickness is not that expected by the thickness of its monolayer [17].

4.3 *Ex Situ* PM-IRRAS Studies

The methylene groups of phospholipid hydrocarbon chains were analysed to obtain structural information of the bilayers supported on Au. The C-H symmetric and asymmetric stretching vibrations give rise to bands in the spectral region of 3100 - 2800 cm^{-1}. These bands are the strongest in the spectra and are considered conformation-sensitive; any increase in the hydrocarbon chain conformational disorder is accompanied by increases in their frequencies. This property can be used to monitor changes in conformational order of the lipids' hydrocarbon chains. Depending on the band position and the full-width at half-maximum (FWHM) different phases, such as gel state (L_α), liquid crystalline state (L_β) or even the intermediate phase transition, can be assigned for a particular phospholipid.

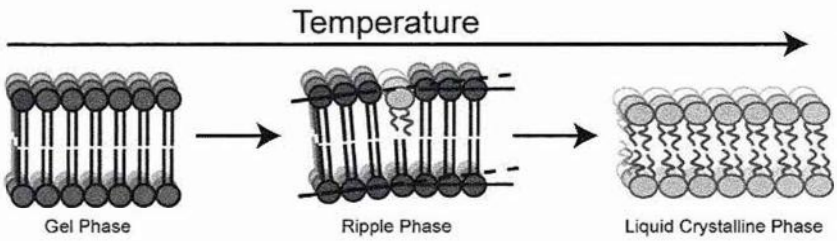

Figure 4.7: Phase transitions of the lipids.

The *ex situ* PM-IRRA spectra of phospholipid bilayers are shown in Figure 4.8. The asymmetric and symmetric methyl stretching modes for the studied phospholipids are located at ≈2963.5 ± 0.2 cm^{-1} and ≈2875.4 ± 0.5 cm^{-1}. Bilayers in a liquid crystalline state had previously been shown to have vibrations at 2925.5 cm^{-1} for $\nu_{as}(CH_2)$ and 2853.4 cm^{-1} for $\nu_s(CH_2)$ [18, 19]. In this state, the bandwidths become broader due to the increase in the molecules' motion and the changes in the conformational states of the hydrocarbon chains. Bilayers in the gel state have been reported to show band frequencies lower than 2920 cm^{-1} for $\nu_{as}(CH_2)$ and lower than 2850 cm^{-1} for $\nu_s(CH_2)$; in this state the acyl chains are fully stretched and assume an all-*trans* conformation [19-21].

The positions of the methylene stretching modes for the DMPC bilayer at the Au(111) are situated at 2923.7 cm^{-1} for $\nu_{as}(CH_2)$ and 2852.9 cm^{-1} for $\nu_s(CH_2)$. These values are in the borderline between the two states, indicating that the acyl chains of the DMPC molecules are generally in *trans* conformation but have a number of

melted chains and *gauche* conformations [3]. The FWHM for the DMPC bilayer in Figure 4.8 are equal to 26.3 cm^{-1} and 13.3 cm^{-1} for the $\nu_{as}(CH_2)$ and $\nu_s(CH_2)$ modes, respectively.

The positions of the methylene stretching modes of DMPE, DMPS and CL are shown in Figure 4.8. The band positions for these molecules are shifted to lower wavenumbers, indicating that the hydrocarbon chains exist in the gel phase. This phase is characterized by the presence of well-ordered acyl chains in the lipid molecule with predominantly all-*trans* conformations. The high wavenumber associated with the $\nu_s(CH_2)$ indicates that the bilayers contain a few *gauche* kinks. Table 4.2 indicates the exact positions of $\nu_{as}(CH_2)$ and $\nu_s(CH_2)$ vibrational modes for DMPE, DMPS and CL bilayers on Au.

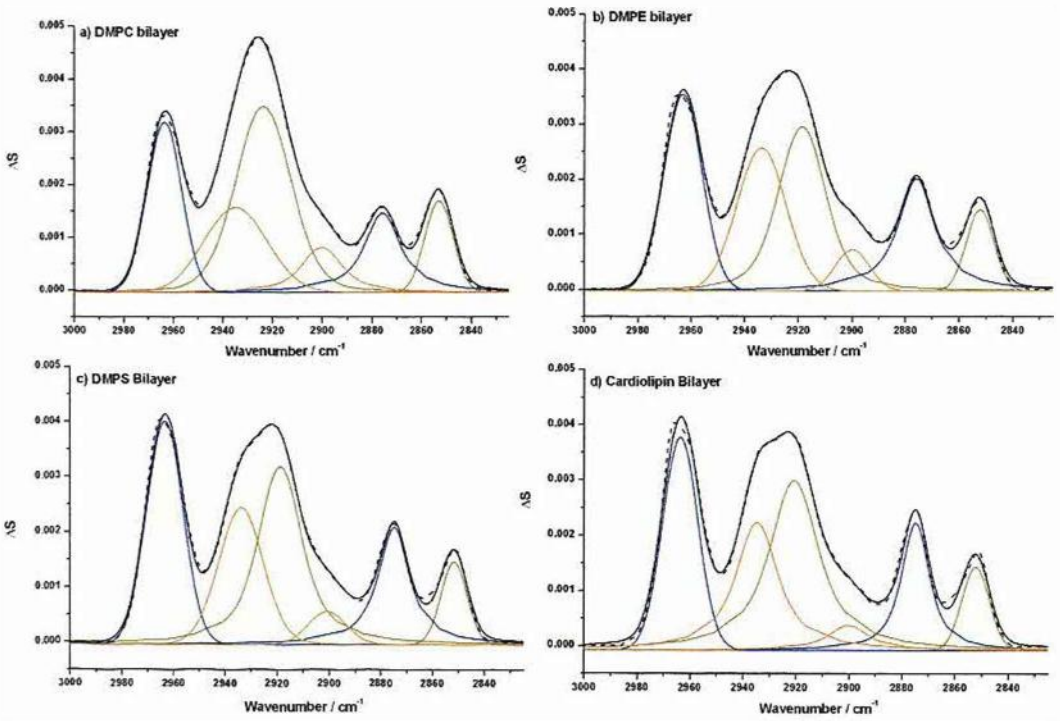

Figure 4.8: *Ex situ* PM-IRRA spectra in the C-H stretching mode region of the phospholipid bilayer transferred onto Au substrates; a) DMPC (π = 40 mN m^{-1}) b) DMPE (π = 50 mN m^{-1}) c) DMPS (π = 50 mN m^{-1}) d) CL (π = 40 mN m^{-1}).

Table 4.2: Frequencies and FWHM of the asymmetric and symmetric stretching mode of the CH_2 group.

	DMPE	*DMPS*	*CL*
$\nu_{as}(CH_2)$-*FWHM* / cm^{-1}	2918.8 / 20.9	2918.9 / 19.9	2920.8 / 22.1
$\nu_{s}(CH_2)$-*FWHM* / cm^{-1}	2852.2 / 12.1	2851.8 / 11.7	2852.3 / 12.1

The calculation of the tilt angle of the hydrocarbon chains was carried out with the knowledge of the integral intensity of a given vibration, as described in Chapter 3. The *ex situ* PM-IRRA spectra of the bilayers for randomly distributed molecules was calculated using the optical constants of DMPE and DMPS and the thicknesses of the bilayers which were obtained previously in ellipsometry experiments. This procedure was described in section 3.8 of this thesis.

Figure 4.9 and Figure 4.10 show the *ex situ* PM-IRRA spectra of DMPE and DMPS bilayers along with the simulated spectra of the randomly oriented molecules.

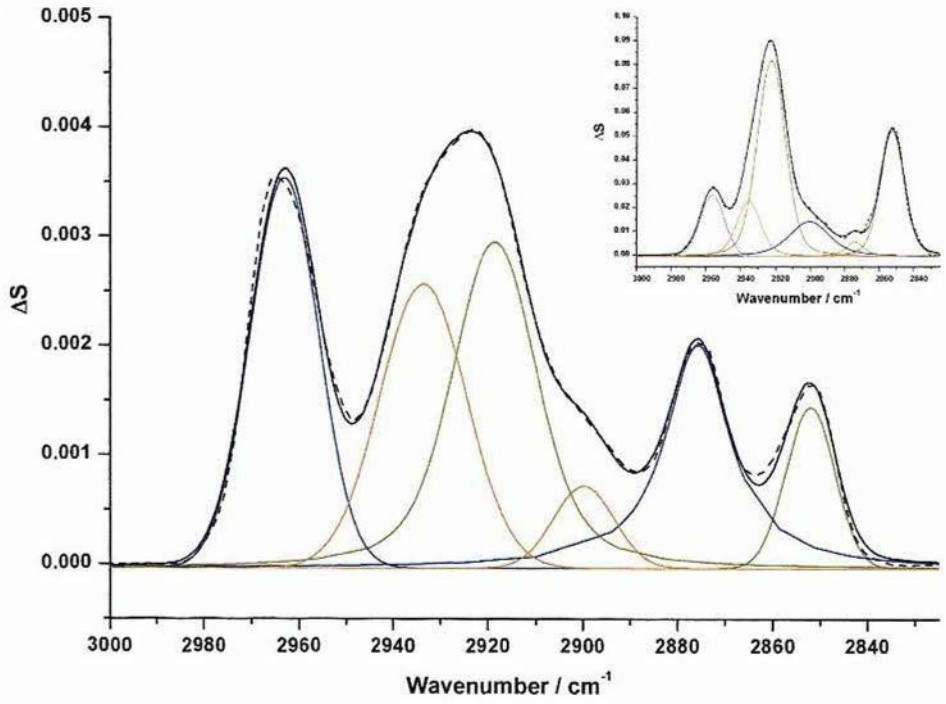

Figure 4.9: Deconvoluted *ex situ* PM-IRRA spectrum of DMPE bilayer transferred onto Au substrate at 50 mN m^{-1}. Insert: the respective simulated *ex situ* PM-IRRAS.

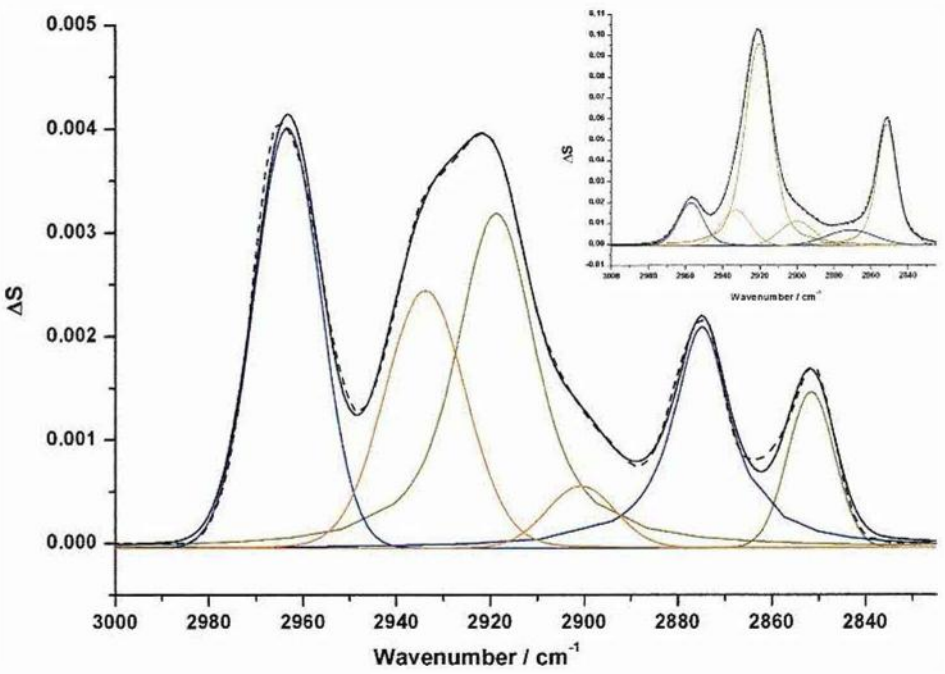

Figure 4.10: Deconvoluted *ex situ* PM-IRRA spectrum of DMPS bilayer transferred onto Au substrate at 50 mN m^{-1}. Insert: the respective simulated *ex situ* PM-IRRAS.

The calculated tilt angles of the hydrocarbon chains in the DMPE and DMPS bilayer on Au substrate at a surface pressure of 50 mN m^{-1} are equal to 8.3° with respect to the surface normal in both cases; this manifests the similarity between these two molecules. The tilt of the hydrocarbon chains for DMPC cannot be provided quantitatively since the acyl chains contain many gauche conformations; however, the integral intensities of the methylene stretching modes are used as an approximation to estimate the value of the chain tilt angle. Figure 4.11 shows the *ex situ* PM-IRRAS spectrum of a DMPC bilayer along with the simulated spectrum of the randomly oriented molecules. The chain tilt angle is calculated using the same methodology as previously; the obtained value is 21.8°. The expected tilt angle of the DMPC hydrocarbon chain in a monolayer compressed at 40 mN m^{-1} at the air/water interface can be determined by using Eq. 4.1 [22,23] :

$$A_{DMPC}\cos\theta_{tilt} = 2\Sigma$$

Eq. 4.1

where A_{DMPC} is the limiting area per DMPC molecule in the monolayer and Σ is the cross-sectional area of a single hydrocarbon chain which, in the gel phase, is equal to Σ_{gel}=0.195 nm^2. Using A_{DMPC}= 0.49 nm^2, the tilt angle of DMPC molecules at the air/solution interface is 37°. The tilt angle for the DMPC bilayer at the gold surface is smaller than at the air/water interface. If the same procedure is used to calculate the area per molecule of the DMPC molecules at the gold surface considering Σ_{liquid}=0.244 nm^2 [24], the A_{DMPC}= 0.53 nm^2, indicating as is expected that there is a different molecular packing depending on the molecular state.

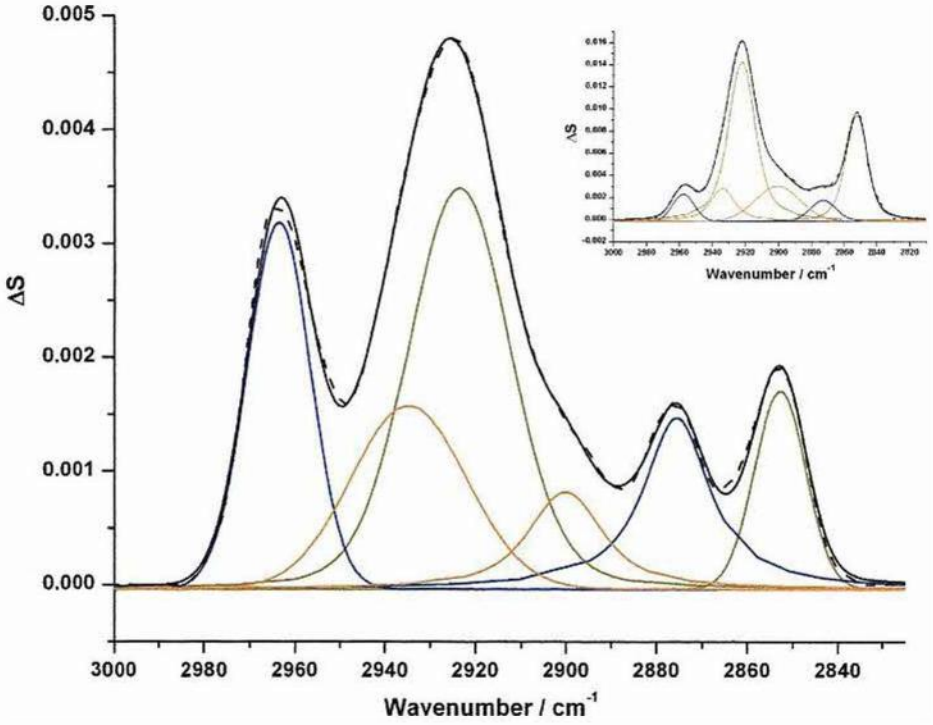

Figure 4.11: Deconvoluted *ex situ* PM-IRRA spectrum of DMPC bilayer transferred onto Au substrate at 40 mN m^{-1}. Insert: the respective simulated *ex situ* PM-IRRAS.

The ν(C=O) stretching band is associated with the ester carbonyl group of the fatty acyl chains. It is considered the most useful of the bands originating from the polar group; it is sensitive to both conformational and environmental factors. The ν(C=O) stretching band is centered at $\approx$ 1735 cm^{-1} but the position and width is dependent on the type of phospholipid and the hydration of the ester groups. Figure 4.12 shows the comparison of the ν(C=O) stretching band for DMPC, DMPE, DMPS and CL bilayers on a Au substrate. The position of the band maximum is very similar

but changes slightly to higher wavenumbers for DMPC and DMPE. The shape of the absorption band for these phospholipids is sharper than for DMPS and CL, which show more intense and broader bands.

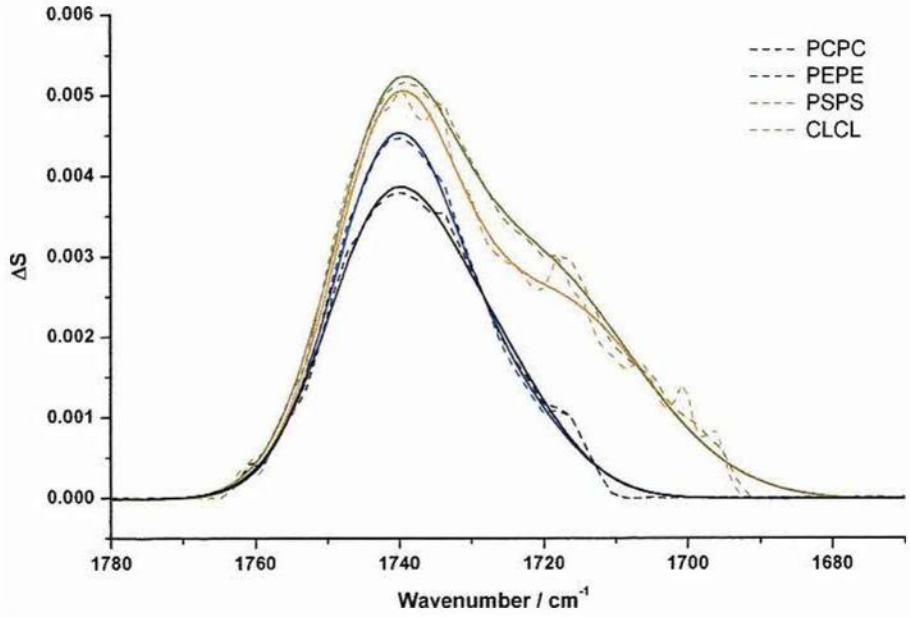

Figure 4.12: PM-IRRA spectra in the C=O stretching mode region of the DMPC, DMPE, DMPS and CL bilayers transferred onto Au substrates.

This band is a superposition of at least two major components that are usually centred near 1742-1738 cm^{-1} and near 1724-1729 cm^{-1}. It has been suggested that these two bands are caused by the conformational non-equivalence of the ester groups of the *sn-1* and *sn-2* chains [21] but more recent work has shown that the difference arises from the degree of hydration and/or hydrogen bonding to the ester carbonyl groups [25, 26]. In general, the higher-wavenumber component band is assigned to the non-hydrogen bonded carbonyl group or dry ester group and the lower- wavenumber component is characteristic of the hydrated ester moieties.

Figure 4.13 shows the deconvolution of the band for each of the different phospholipids. DMPC shows a higher intensity than DMPE for the lower-wavenumber component. The explanation for this agrees with the results in the studies of the C-H stretching region, which indicated that the DMPC molecules were in a ripple state. The fluidity of this state increases the number of hydrogen bonding interactions to both C=O groups with adjacent molecules or with water, thus an

increase in the intensity of the lower-wavenumber component can be observed. The position of this band is centred at 1727.9 cm^{-1} and 1725.0 cm^{-1} for DMPC and DMPE, respectively. The very sharp shape for the ν(C=O) absorption band for DMPE seems to be similar to that reported for a highly ordered crystalline form [27], suggesting that DMPE forms a very compact bilayer where the carbonyl groups are immobilized and that they are not hydrogen bonded to any hydrogen-bonding donor groups.

It is noticeable how the ν(C=O) absorption band is broader and more intense for phospholipids with negatively charged headgroups, which might be due to the stabilization of the charged headgroup by solvation. Characteristic band positions of the gel state are observed for the CL bilayer [28]. A slightly higher intensity in the lower-wavenumber component for DMPS agrees with the notion that DMPS is able to form more easily hydrogen bonds with adjacent molecules or residual water than CL, which is considered mobility-restricted.

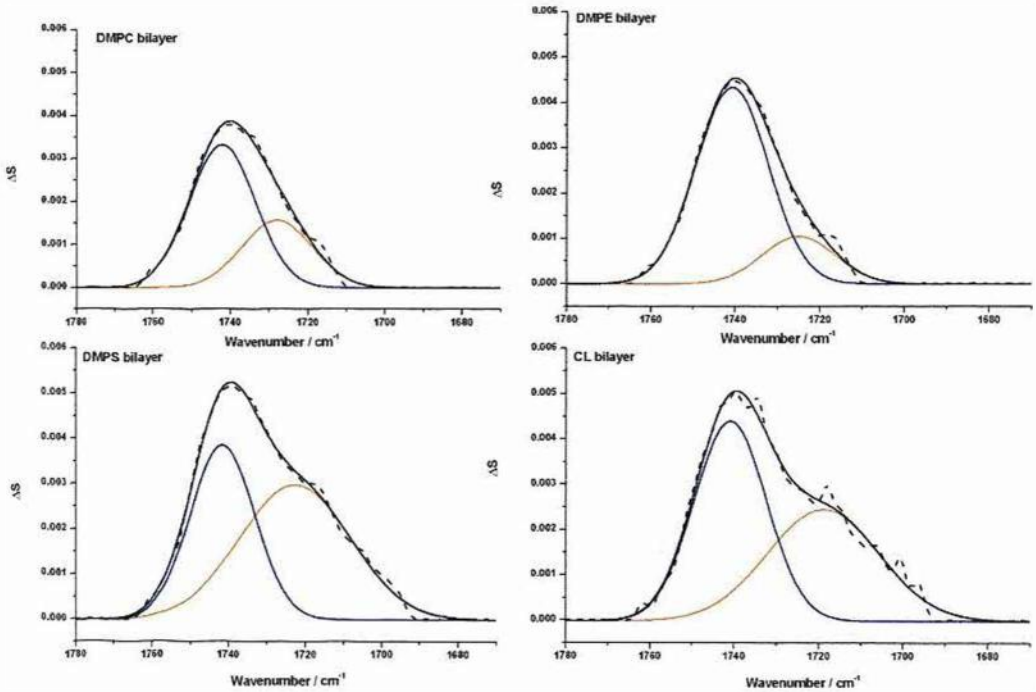

Figure 4.13: Deconvoluted *ex situ* PM-IRRA spectra in the C=O stretching mode region of the DMPC, DMPE, DMPS and CL bilayers transferred onto Au substrates.

Further *in situ* PM-IRRAS studies will reveal the trend in the degree of hydration of the ester groups when different potentials are applied.

References:

1. I. Zawisza, X. M. Bin and J. Lipkowski, *Langmuir*, 2007, **23**, 5180-5194.

2. N. Garcia-Araez, C. L. Brosseau, P. Rodriguez and J. Lipkowski, *Langmuir*, 2006, **22**, 10365-10371.

3. T. Heimburg, *Biophys. J.*, 2000, **78**, 1154-1165.

4. K. A. Riske, R. P. Barroso, C. C. Vequi-Suplicy, R. Germano, V. B. Henriques and M. T. Lamy, *Biochim. Biophys. Acta, Biomembr.*, 2009, **1788**, 954-963.

5. T. Heimburg, *Biochim. Biophys. Acta, Biomembr.*, 1998, **1415**, 147-162.

6. J. Li, R. Miller and H. Mohwald, *Colloids Surf., A*, 1996, **114**, 123-130.

7. J. T. Mason and T. J. O'Leary, *Biophys. J.*, 1990, **58**, 277-281.

8. M. C. Petty, *Langmuir-Blodgett Films-An Introduction*, Cambridge University Press, Cambridge, 1996.

9. S. Marcelja, *Biochim. Biophys. Acta, Biomembr.*, 1974, **367**, 165-176.

10. C. Luna, K. M. Stroka, H. Bermudez and H. Aranda-Espinoza, *Colloids Surf., B*, **85**, 293-300.

11. H. I. Petrache, S. Tristram-Nagle, K. Gawrisch, D. Harries, V. A. Parsegian and J. F. Nagle, *Biophys. J.*, 2004, **86**, 1574-1586.

12. R. A. Demel, F. Paltauf and H. Hauser, *Biochemistry*, 1987, **26**, 8659-8665.

13. U. R. Pedersen, C. Leidy, P. Westh and G. H. Peters, *Biochim. Biophys. Acta, Biomembr.*, 2006, **1758**, 573-582.

14. F. Etienne, Y. Roche, P. Peretti and S. Bernard, *Chem. Phys. Lipids*, 2008, **152**, 13-23.

15. A. Houle, F. Techy, J. Aghion and R. M. Leblanc, *J. Lipid Res.*, 1982, **23**, 496-502.

16. A. Alessandrini and U. Muscatello, *J. Phys. Chem. B*, 2009, **113**, 3437-3444.

17. M. Li, M. Chen, E. Sheepwash, C. L. Brosseau, H. Li, B. Pettinger, H. Gruler and J. Lipkowski, *Langmuir*, 2008, **24**, 10313-10323.

18. R. A. Dluhy, S. M. Stephens, S. Widayati and A. D. Williams, *Spec. Acta A: Mol. Biomol. Spec.*, 1995, **51**, 1413-1447.

19. M. L. Mitchell and R. A. Dluhy, *J. Am. Chem. Soc.*, 1988, **110**, 712-718.

20. H. L. Casal and H. H. Mantsch, *Biochim. Biophys. Acta, Rev. Biomembr.*, 1984, **779**, 381-401.

21. H. H. Mantsch and R. N. McElhaney, *Chem. Phys. Lipids*, 1991, **57**, 213-226.

22. H. Hauser, I. Pascher, R. H. Pearson and S. Sundell, *Biochim. Biophys. Acta, Rev. Biomembr.*, 1981, **650**, 21-51.

23. F. Sun, *Biophys. J.*, 2002, **82**, 2511-2519.

24. I. Pascher, M. Lundmark, N. Per-Georg and S. Sundell, *Biochim. Biophys. Acta, Rev. Biomembr.*, 1992, **1113**, 339-373.

25. R. N. A. H. Lewis and R. N. McElhaney, *Chem. Phys. Lipids*, 1998, **96**, 9-21.

26. A. Blume, W. Huebner and G. Messner, *Biochemistry*, 1988, **27**, 8239-8249.

27. R. N. A. H. Lewis and R. N. McElhaney, *Biophys. J.*, 1993, **64**, 1081-1096.

28. R. N. A. H. Lewis, D. Zweytick, G. Pabst, K. Lohner and R. N. McElhaney, *Biophys. J.*, 2007, **92**, 3166-3177.

CHAPTER 5: ELECTROCHEMICAL MEASUREMENTS

5.1 Introduction

A detailed electrochemical study of symmetric and asymmetric phospholipid bilayers on Au(111) is presented in this chapter. The electrochemical measurements provided information on the average properties of the bilayer membrane. Differential capacitance (DC) and chronocoulometry were combined in order to gain a complete description of the structure of the interface at supported phospholipid bilayers.

5.2 Electrochemistry of Bare Au(111) Electrode

At the beginning of all the electrochemical experiments, the Au(111) was flame annealed for several minutes as described in section 3.6 of this thesis. The electrolyte solution was de-oxygenated prior to recording any cyclic voltammograms to assess its purity and cleanliness.

A typical differential capacity curve for the supporting electrolyte is shown in Figure 5.1. At positive potentials (E≈ 0.4 V), the range is limited by the oxidation of the gold and the limit for the negative potential is determined by the desorption of the lipid bilayer from the gold at E≈ -0.8 V and the hydrogen evolution at E≈ -1.2 V. Hysteresis in the capacitance is observed in Figure 5.1 due to the different kinetics of the gold surface reconstruction towards the reduction or oxidation direction.

Differential capacitance provided useful information relating to the compactness and the defect level in supported lipids bilayers for many years [1]. To understand DC measurements, the simple Helmholtz model of the interface is used because the metal/solution interface behaves as an ideal capacitor within the potential range applied. This model relates the capacitance to the thickness (*d*) of the bilayer by the following equation:

$$C_m \propto \frac{\varepsilon_0 \varepsilon_m}{d}$$

Eq. 5.1

Equation 5.1, indicates that when the value of the capacitance is low, the thicker and more defect-free the membrane is. Sometimes a high value of the capacitance is determined by changes of permittivity, indicating a swelling in the bilayer and the incorporation of solution within the bilayer.

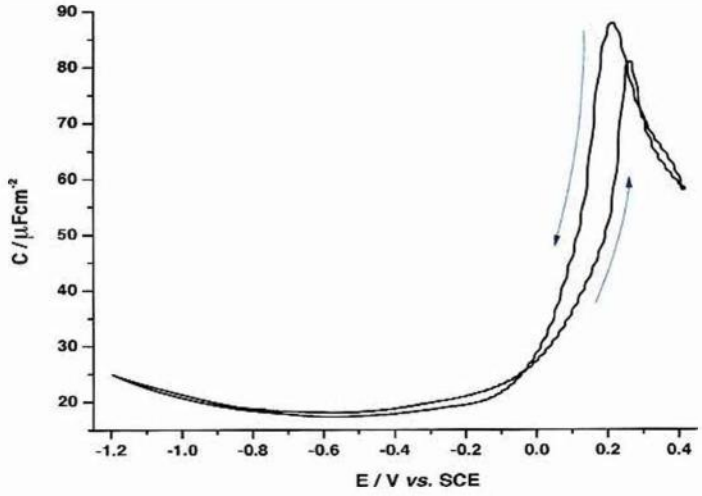

Figure 5.1: Differential capacitance plot of a bare Au(111) electrode in 0.1 M NaF electrolyte solution at 20°C.

5.3 Electrochemistry of Symmetric Bilayers

5.3.1 Differential Capacitance

Capacitance in the reduction direction of the symmetric bilayer deposited on Au(111) is shown in Figure 5.2. At the most negative potentials (E< -1 V), the capacity in the presence of the bilayer merges with that of the pure electrolyte indicating that phospholipid bilayers are not adsorbed at the gold surface at these negative potentials. It is important to consider that the hydrogen evolution reaction and/or the bilayer detachment at around E=-1.2 V could destroy the integrity of the bilayer at these negative potentials; however, this does not appear to have occurred in these experiments because stability was observed in the values of the differential capacitance over some cycles. Due to the difficulty in the repeatability of the meniscus height in the working electrode after bilayer deposition, slight changes in the differential capacity curve in this region can be found.

Neutron reflectivity experiments on DMPC/cholesterol vesicles fused onto a Au(111) electrode demonstrated that in the range of -1 V < E < -0.5 V the lifted

bilayer remained in close proximity to the electrode by an approximately 1 nm thick water cushion [2].

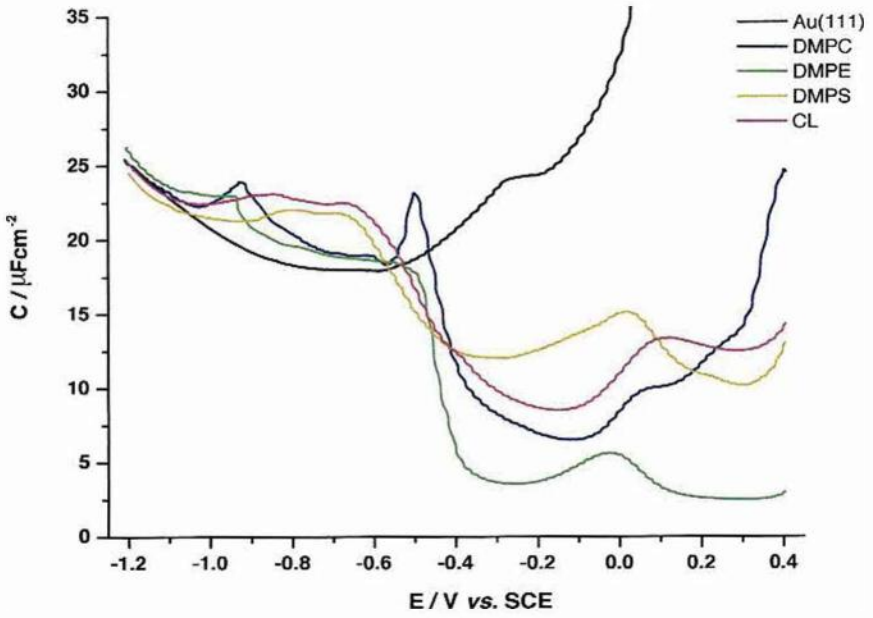

Figure 5.2: Comparison of DC curves for symmetric bilayers on Au(111) electrode in 0.1 M NaF electrolyte solution at 20°C.

The beginning of the bilayer adsorption is observed by a pseudo-capacity peak at E≈ -0.9 V for DMPC and DMPE films. This peak is shown to be more intense in the onset of DMPC adsorption. These characteristic peaks are broader for CL and DMPS and have a maximum capacitance at E≈ -0.65 V, just before lessening to their minimum value.

Previous work carried out on DMPC indicated that, at E≈ -0.5 V there was a phase transition which involved direct adsorption of DMPC onto the gold surface, accompanied by a reorientation of the acyl chains, decreasing their tilt angle [3, 4]. This phase transition is also seen in Figure 5.2 for DMPE. Towards positive potentials, the value of the capacity decreases slowly for DMPC and rapidly for DMPE. The minimum capacitance for all the bilayers was achieved at E> -0.4 V denoting the formation of a compact film on the surface electrode within the potential range of -0.4 to 0.4 V. The minimum values of the capacity in this region are shown in table 5.1. These minima values are higher than the value of the capacity of a metal electrode surface covered by a defect free phospholipid bilayer that was reported to be ≈0.8 μF cm^{-2} [5]. This implies the presence of some kind of defects in the film.

Table 5.1: Minimum capacitance observed for the adsorbed bilayer

Symmetric Bilayer	$C_{minimum}$ / μF cm^{-2}
DMPC	6.5
DMPE	2.5
DMPS	10
CL	8.5

Figure 5.3 shows the differential capacitance of a DMPC bilayer on Au(111) in 0.1 M NaF electrolyte solution. A detailed study of the electrochemistry of DMPC bilayer on Au(111) was carried out by Lipkowski's group and will only be briefly discussed here [2-4, 6-8].

In the region in which the DMPC bilayer is adsorbed, the polar head, especially the phosphate group, has its maximum contact with the metal; this increases the area per molecule causing the chains to tilt and be less densely packed. The change in the packing allows the ingress of water into the bilayer, which raises the capacitance towards positive potentials. At very positive potentials, IR and AFM studies suggested that the ester groups of DMPC were well hydrated increasing the thickness of the bilayer [7, 9]. Changes in the capacitance at E> 0.2 V are caused by changes in the permittivity.

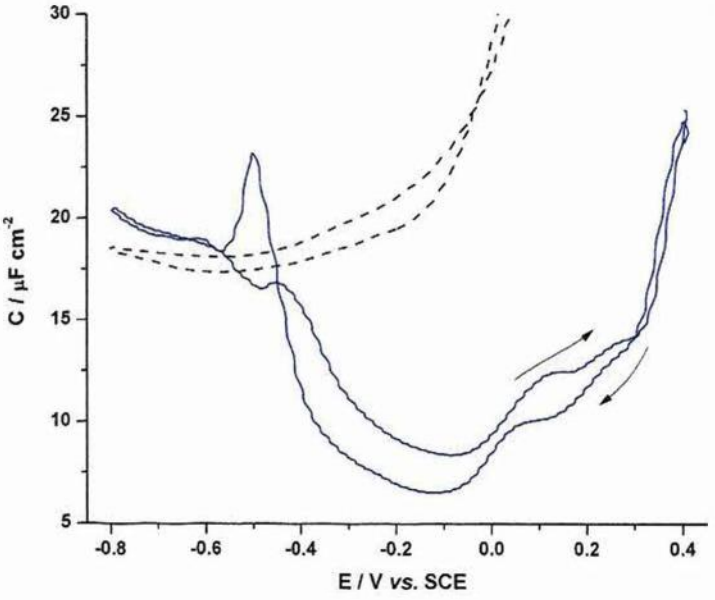

Figure 5.3: Differential capacity *vs.* potential curve of a DMPC bilayer at the Au(111) electrode in 0.1 M NaF electrolyte solution at 20°C.

In the studies of DMPE bilayer on gold (Figure 5.4), an improvement in the quality of the supported bilayer is seen due to a decrease in the capacitance to a minimum value of 2.5 $\mu F\ cm^{-2}$. Previous studies in Chapter 3 using isotherms showed that the area per molecule of DMPE (43 $Å^2$) was smaller than for DMPC (49 $Å^2$) in agreement with the literature [10]. This small DMPE headgroup allows the molecules to pack more tightly than other phospholipids such as DMPC, creating a very compact and stable arrangement of bilayers. This agrees with reported articles that suggested this stability due to the direct hydrogen bonding between DMPE headgroups [11]. A phase transition is seen by a peak in the capacitance at $E \approx 0$ V.

Water organization and dielectric permittivity varied within the different regions of the solid/liquid interface depending on the phospholipid headgroup structure and its nett charge. In phospholipids with a negatively charged headgroup such as DMPS and CL, a higher dielectric permittivity seems to explain the behaviour of the capacity curves.

For DMPS bilayers, the differential capacitance curve in Figure 5.5 shows the highest capacitance between the range of $-0.4\ V < E < 0.2\ V$, suggesting the association of DMPS headgroups with protons or a bilayer with a high solvent content. DMPS carbonyl groups were reported as being easily accessible from the aqueous phase [10] thus, large and well hydrated ions could bind with DMPS effectively, increasing the permittivity and, in consequence, the capacitance.

A phase transition previously seen for DMPE is also observed at $E \approx 0$ V.

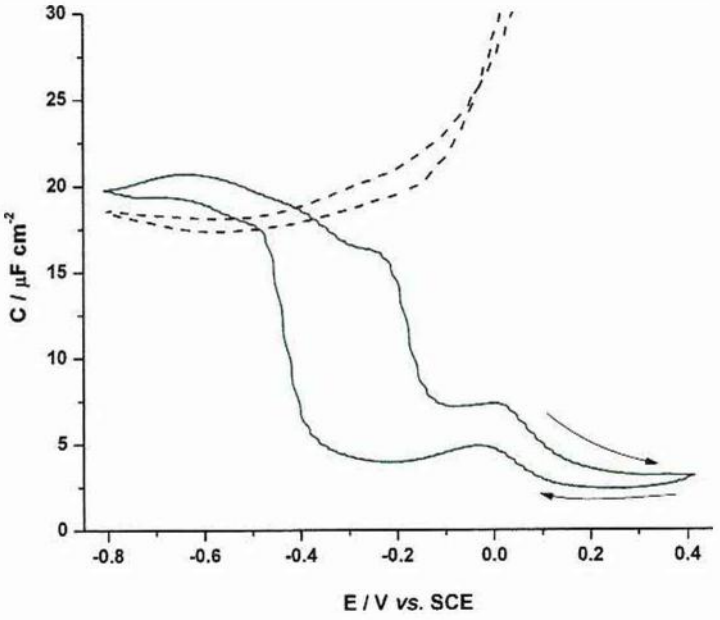

Figure 5.4: Differential capacity *vs.* potential curve of a DMPE bilayer at the Au(111) electrode in 0.1 M NaF electrolyte solution at 20°C.

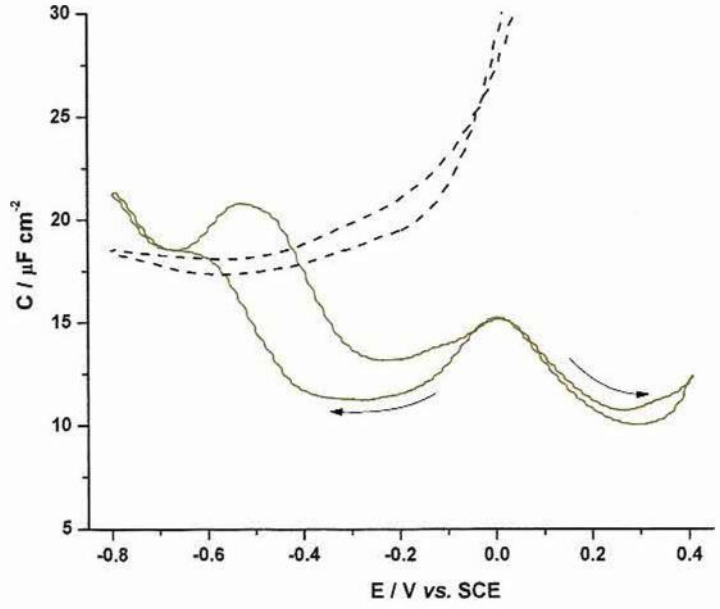

Figure 5.5: Differential capacity *vs.* potential curve of a DMPS bilayer at the Au(111) electrode in 0.1 M NaF electrolyte solution at 20°C.

Due to the relatively small headgroup, cardiolipin is expected to have a great cohesion between the hydrocarbon chains in its bilayer. The high cohesion between molecules restrict the mobility and flexibility of the headgroup alcohol from intra-molecular interactions [12], thus when the bilayer is adsorbed on the electrode, the molecules are expected to be perpendicular to the gold surface, decreasing the capacitance below DMPC values due to the higher bilayer thickness which is reported in Chapter 4.

The presence in the CL of two negatively charged phosphate groups and carbonyl groups shows the ability for interaction with ions that are dissolved in the solution [13]. This interaction with ions results in an increase of the capacity. At E> 0 V there is a slow increase in the capacitance; similar behaviour was observed for DMPC bilayers and explained by the incorporation of ions and solvent into the bilayer. A similar argument could be advanced for CL, although, with the negative charge there could also be a rearrangement of headgroups as the surface tends towards neutral and positive charge.

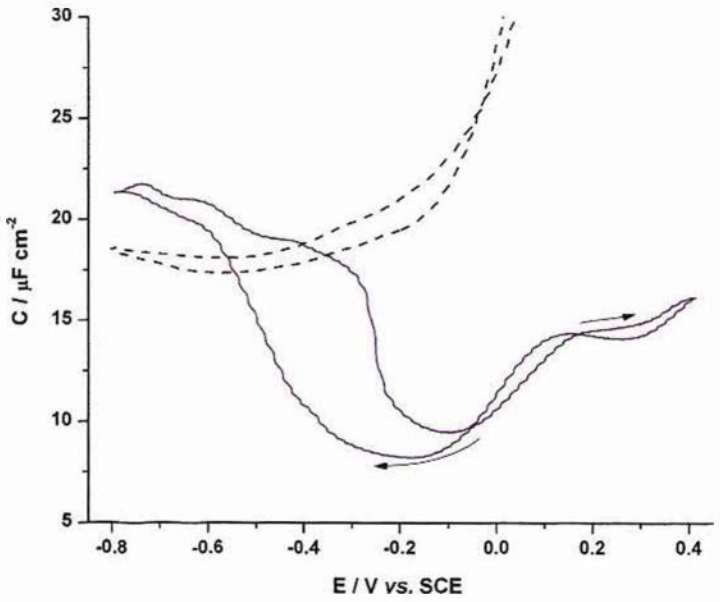

Figure 5.6: Differential capacity *vs.* potential curve of CL bilayer at the Au(111) electrode in 0.1 M NaF electrolyte solution at 20°C.

5.3.2 Chronocoulometry of Symmetric Membranes

The charge density on the metal surface, σ_M, was measured using the chronocoulometry method [14]. Figure 5.7 shows charge density plotted versus potential of the gold electrode in the absence and in the presence of phospholipid bilayer in 0.1 M NaF supporting electrolyte at 20°C.

The charge density curves exhibit distinct regions. From -1.2 V < E < -0.9 V the curves initially coincide with the curve for the pure electrolyte, indicating that the bilayer does not adsorb at these negative potentials, in agreement with DC experiments. At E≥ -0.9 V where the $\sigma_M \geq$ -30 μC cm^{-2}, a sigmoidal increase in σ_M indicates the starting point in the bilayer adsorption onto the gold electrode, this step coincides with the peak in DC curve but is not subject to kinetics. A well-defined step for symmetric DMPE bilayers is observed at E≈ -0.65 V. This step is also seen, less pronounced, for DMPC bilayers.

A third region formed from -0.4 V < E < +0.2 V is characterized by a linear rise in σ_M with increasingly positive potentials. This section corresponded to the formation of the compact film at the electrode surface. In this potential region, the σ_M of the gold covered by the bilayer changes from ≈ -10 μC cm^{-2} to more positive values depending on the adsorbed bilayer.

The fourth region at E> 0.2 V shows a rapid increase in the σ_M towards positive potentials. Between -0.01 V < E < 0.1 V the σ_M is negative for DMPC and DMPE, and positive for DMPS and CL bilayers. This behaviour is most likely due to the presence of the negatively charged headgroup.

The potential of zero charge of the Au(111) electrode, E_{pzc} is equal to +0.275 V *vs.* SCE. For all the bilayers, the adsorption of the bilayer on the electrode surface causes a negative shift of the E_{pzc}. This is observed more clearly in Figure 5.8, where the films are plotted together with the error bar omitted for more clarity. The E_{pzc} for zwitterionic phospholipids is similar, E_{pzc}≈ +0.12 V and this becomes more negative for charged phospholipids, E_{pzc}≈ -0.01 V. Differences in the potential of zero charge (E_N) for DMPC and DMPE bilayers gives a E_N≈ -155 mV and E_N≈ -285 mV for DMPS and CL. The shift in the pzc is described by the following equation [15]:

$$E_N = \frac{\Gamma\left(\mu_\perp^{org} - n\mu_\perp^{w}\right)}{\varepsilon}$$

Eq. 5.2

where Γ is the surface concentration of molecules, ε is the permittivity and, $\mu_\perp^{org}$ and $\mu_\perp^{w}$ are the components of the permanent dipole of organic and water molecules in the direction normal to the surface. *n* is the number of water molecules displaced from the surface by one organic molecule.

At the pzc of the Au/solution interface, water molecules are expected to have a small preferential orientation with the water oxygen atoms towards the metal, and hence $\mu_\perp^{w}$ should be very small and negative [16]. Therefore, $\mu_\perp^{w}$ is expected to bring a small positive contribution to E_N. The dipole potential in phospholipids $\mu_\perp^{org}$ arises from the functional group dipoles of the terminal methyl groups of aliphatic chains, the glycerol-ester region and the hydrated polar head groups. The absolute value of the dipole potential due to the orientation of permanent dipoles of the phospholipid molecules should be somewhat higher than 155 mV for DMPC and DMPE bilayers and higher than 285 mV for CL and DMPS.

For saturated phosphatidylcholine membranes, the value estimated for the dipole potential ranges from 300 to 400 mV, [17] which agrees with the higher values obtained for DMPS and CL bilayers. Presumably the negative charge of the serine and the hydroxyl groups of the glycerol are buried inside the polar head region so that they do not significantly attract ions that could decrease the dipole potential [18].

A reduction in the permanent dipole for DMPE may be due to the influence of its conformation and orientation. Changes in the tilt angle of the dipole P^--N^+ can cause different magnitudes in the dipole potential. If the dipole is tilted this contributes to a reduction in the phospholipid dipole potential. Reported studies in vesicles formed by DMPC and DMPE have shown an increase in the dipole potential due to the parallel orientation of the DMPE molecules within the vesicles [17].

The shift of the pzc for LBLS DMPC bilayers has been reported to be quite similar to ours ($E_N \approx$ 127 mV). At the E_{pzc} the polar heads of DMPC molecules are reported to be located flat to the interface or parallel to the substrate [4, 19], therefore the dipole P^--N^+ does not contribute to the reduction of the overall dipole potential

of DMPC bilayers, the reduction could be due the effective screening of charges from the solution and/or some small asymmetry between both leaflets of the bilayer.

We can conclude that differences in the E_{pzc} suggests different orientation of the zwitterionic and the negatively charged headgroups in the bilayer.

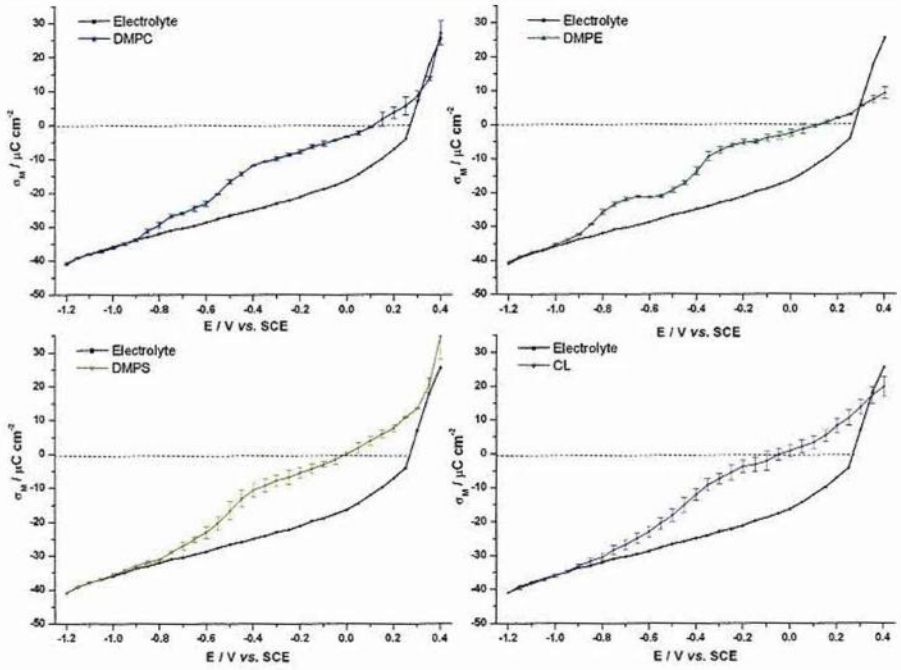

Figure 5.7: Surface charge density for a bare Au(111) electrode and symmetric bilayers supported on a Au(111) electrode in 0.1 M NaF supporting electrolyte.

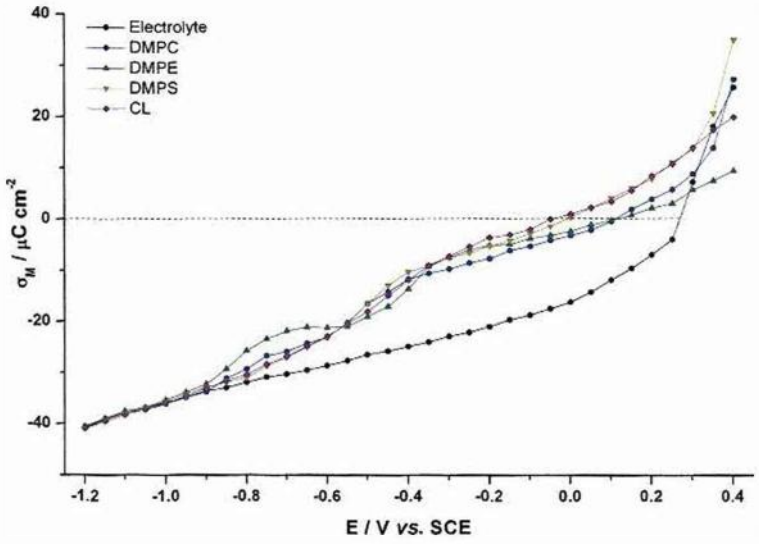

Figure 5.8: Comparison of surface charge density for symmetric bilayers supported on a Au(111) electrode in 0.1 M NaF supporting electrolyte at 20°C.

The surface pressure of the bilayer, π, corresponds to the area between the charge density curve for the supporting electrolyte and that of the bilayer-coated surface. The surface pressure was therefore calculated by the integration of these curves using the equation described in chapter 2 (Eq. 2.20) and given below:

$$\pi = \int_{E_{f=-1.2}}^{E_{i=0.4}} \left(\sigma_{M_\theta} - \sigma_{M_{\theta=0}}\right) dE$$

Eq. 5.3

Figure 5.9 shows π for the different symmetric bilayers against the applied potential. The π decreases from positive potentials in a parabola shaped curve due to the bilayer detachment from the gold surface. The maximum π is observable close to the E_{pzc} of Au(111) and its value is similar for the DMPS and CL bilayers, this suggests that the anionic molecules can be attracted to the very positively charged surface. A decrease of π is observed for DMPC and DMPE at E> 0.4 V indicating that the bilayers are detaching from the electrode surface. The lateral interaction between the negatively charged phopholipids and hydrogen bonding interactions between DMPE headgroups are reflected in the plot by a very high surface pressure at E< 0.1 V.

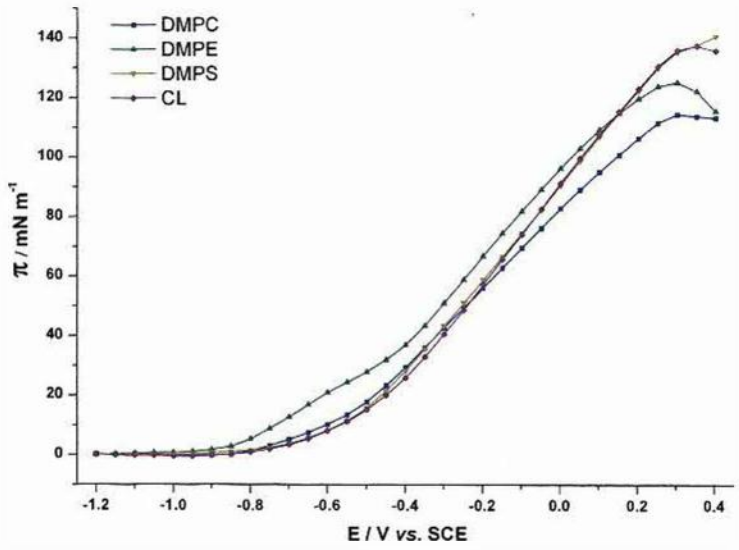

Figure 5.9: Comparison of surface pressure for asymmetric bilayer supported on a Au(111) electrode in 0.1 M NaF supporting electrolyte at 20°C.

5.4 Electrochemistry of Asymmetric Bilayers

More realistic films based on the heterogeneous distribution of phospholipids in biological membranes are described in this section. Differential capacitance and chronocoulometry studies show how the asymmetry between each leaflet may affect the electrochemical bilayer response.

5.4.1 Asymmetric Bilayers Between DMPC and DMPE

5.4.1.1 Differential capacitance of asymmetric bilayer (DMPC-DMPE)

Differential capacitance of asymmetric bilayers formed by the combination of DMPC and DMPE monolayers were compared. In the Au_DMPC-DMPE system, a DMPC monolayer was deposited by the LB method and was in direct contact with the gold electrode; DMPE was deposited using the LS method and was the outer layer of the asymmetric bilayer. In the second model, Au_DMPE-DMPC, the phospholipids were inversely deposited.

Figure 5.10 shows the DC of these two systems. The beginning of the bilayer adsorption starts at E≈ -0.9 V. Moving towards positive potentials, a phase-transition is observed at E≈ -0.5 V, which was previously seen for DMPC symmetric bilayers as a result of a removal of the water content from beneath of the layer which changes the tilt angle of the lipid acyl chains and adsorbs the headgroups onto the surface. The intensity of this phase-transition is more noticeable for the Au_DMPC-DMPE bilayer.

At potentials more positive than -0.4 V, the bilayer is adsorbed on the electrode surface as a compact film and the differential capacity decreases to 6 $\mu F\ cm^{-2}$.

A second phase transition takes place at E≈ 0 V. The studies of symmetric bilayers such as DMPE and DMPS showed this similar transition at around the same potential (section 5.3.1). In the Au_DMPE-DMPC system, the differential capacity is very similar prior to and after this phase transition, indicating a more compact system when DMPE is adjacent to the gold surface. This asymmetric bilayer is able to maintain its structure due to the flexibility of the external DMPC monolayer. This monolayer can assume its spontaneous curvature decreasing the defects within the bilayer and avoiding disruption by solvent. There is a similar tendency for a symmetric DMPE bilayer, this bilayer maintains its structure after this phase transition

due to the strong network of hydrogen bonds between molecules which is not disrupted by solvent.

An increase in the capacitance after this second phase transition for the Au_DMPC-DMPE system indicates a film of higher solvent content. To explain this behaviour it is necessary to understand that DMPC adjacent to the electrode forms borderlines from different domains in which the direction of the tilt differs. These borderlines open spaces for the penetration of the solution, increasing the permittivity of the bilayer. The defects within this film influence the formation of the DMPE on top, resulting in a film of overall higher solvent.

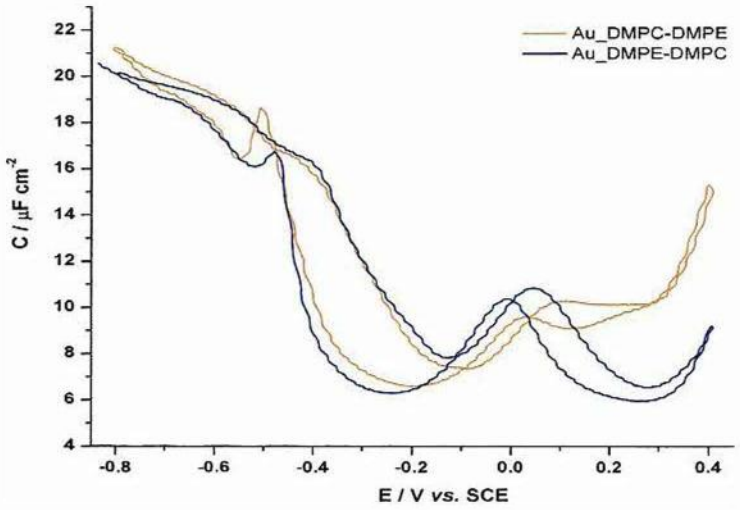

Figure 5.10: Comparison of the differential capacity curves for asymmetric bilayers formed with DMPC and DMPE on Au(111) electrode in 0.1 M NaF electrolyte solution at 20°C.

IR bands from these asymmetric bilayers are also shown in Figure 5.11. The layer adjacent to the gold appears to dominate the overall bilayer structure.

The position of the methylene stretching modes $\nu_{as}(CH_2)$ and $\nu_s(CH_2)$ are shifted to higher wavenumbers for Au_DMPC-DMPE bilayer, indicating more hydrocarbon chain conformational disorder for this asymmetric film. These values are very close to comment on them in any depth but the higher width associated at these absorption bands shows higher dynamics of this system, indicating an increase in the disorder. Table 5.2 indicates the exact positions of $\nu_{as}(CH_2)$ and $\nu_s(CH_2)$ vibrational modes for both systems.

Table 5.2: Wavenumber and FWHM of the methylene stretching modes in asymmetric bilayers formed between DMPC and DMPE.

	Au_DMPC-DMPE	*Au_DMPE-DMPC*
$\nu_{as}(CH_2)$-*FWHM* / cm^{-1}	2921.8 / 25.1	2919.3 / 18.0
$\nu_{s}(CH_2)$-*FWHM* / cm^{-1}	2852.0 / 14.9	2851.8 / 13.6

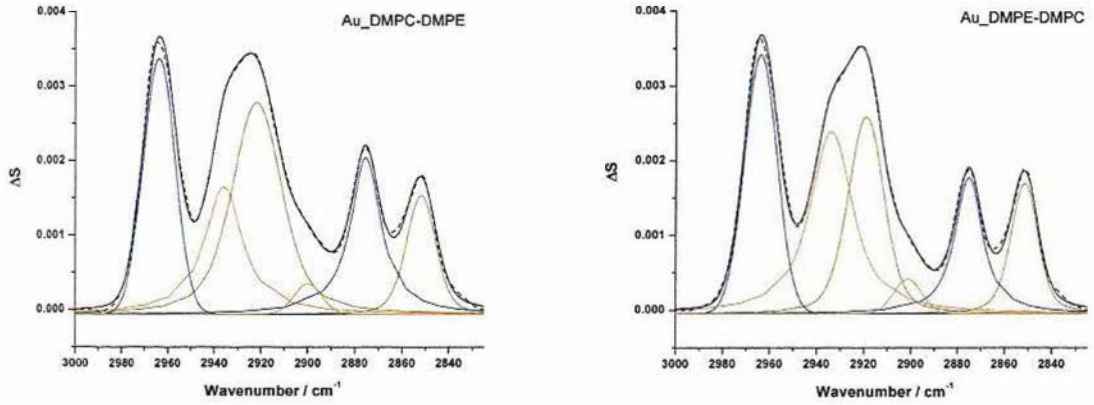

Figure 5.11: Deconvoluted *ex situ* PM-IRRA spectra for C-H stretching bands of Au_DMPC-DMPE (left) and Au_DMPE-DMPC (right) bilayers on a gold substrate.

5.4.1.2 Chronocoulometry of asymmetric bilayer (DMPC-DMPE)

Chronocoulometry curves of Au_DMPC-DMPE and Au_DMPE-DMPC bilayers are shown in Figure 5.12. At negative potentials the bilayers are not adsorbed on the electrode surface and the graphs coincide with the curve for the pure electrolyte.

At around E≈ -0.95 V, σ_M starts increasing as the bilayer begins to adsorb. Around E≈ -0.5 V a well-defined step is observed. The major difference in the σ_M between these two systems occurs in this region. Another important region that differed in the value of σ_M is at E> +0.3 V. In these both cases the σ_M is shallower when DMPE is the inner layer. These results are in agreement with DC studies, which showed smaller capacity in the same region where σ_M differed.

The formation of the compact film on the electrode takes place at potential between -0.3 V < E < 0.3 V. In this region the chronocoulometry shows similar tendencies, some differences in this region from DC studies indicate that somehow the bilayer is affected by the kinetics, perhaps due to a faster water ingress in the DMPC leaflet.

Surface pressure graphs of these systems are presented in the insets to Figure 5.12. At E< -0.5 V the surface pressure of both bilayers merges indicating that the bilayers start to detach from the electrode and the interaction with water is more favourable. At E> -0.5 V the surface pressure of Au_DMPC-DMPE bilayer is higher suggesting more molecular interaction in this system.

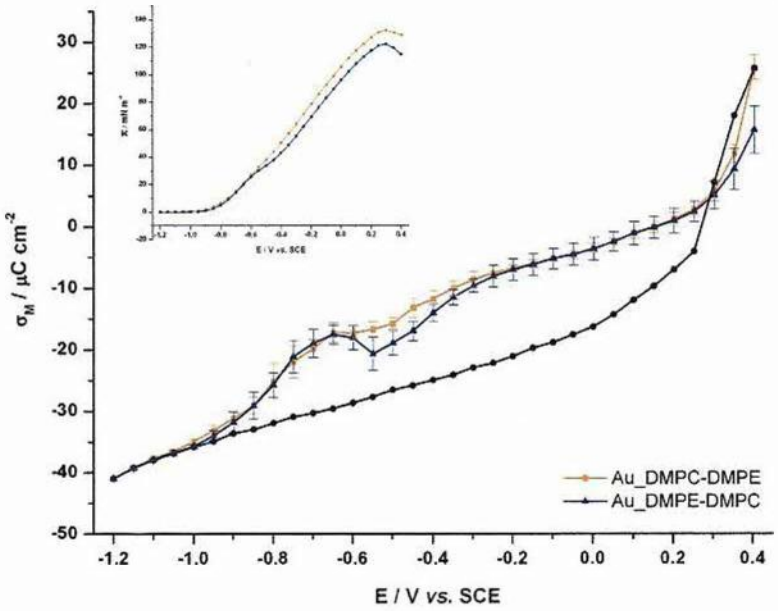

Figure 5.12: Surface charge density for a bare Au(111) electrode and Au_DMPC-DMPE and Au_DMPE-DMPC films supported on a Au(111) electrode in 0.1 M NaF electrolyte solution at 20°C. Insert: Surface pressure of these films in the same experimental conditions.

In order to study the possibility of translocation of the lipids from the outer to the inner leaflet or vice versa during the desorption potential in chronocoulometry experiments, a solution of DMPC and DMPE (1:1) was used for the deposition of a mixed bilayer on the gold electrode at a surface pressure of 40 mN m^{-1}. Any translocation through the lipid bilayer would be interpreted by the comparison with chronocoulometry experiments for Au_DMPC-DMPE and Au_DMPE-DMPC films. Figure 5.13 shows σ_M of the mixed bilayer (Au_PCPE$_{MIX}$) *vs.* applied potential.

It has been shown that electrochemical properties of asymmetric bilayers were dominated by the inner layer, thus any change in the profile of the inner monolayer of Au_PCPE$_{MIX}$ bilayer can be detected by the tendency of this change towards the

charge density of Au_DMPE-DMPC or Au_DMPC-DMPE bilayers, respectively. In Figure 5.12 there is a comparison of the Au_PCPE$_{MIX}$ bilayer with the respective asymmetric bilayers. The mixed bilayer shows a behaviour between Au_DMPE-DMPC and Au_DMPC-DMPE. This distinct behaviour might indicate that there is no translocation or this translocation might not affect the overall bilayer response.

The E_{pzc} in these bilayer had an identical value of E_{pzc} = 0.15 V indicating that the permanent dipole of these bilayers did not change as a result of the asymmetry of this bilayer.

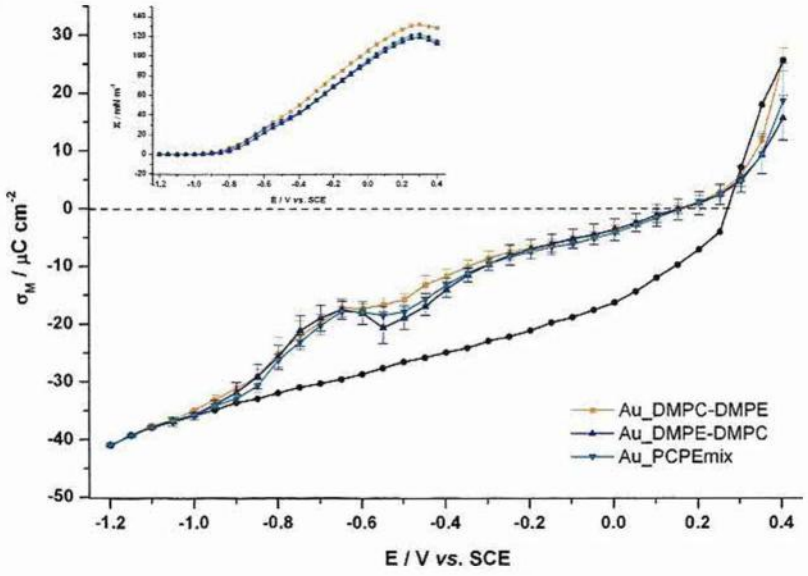

Figure 5.12: Comparison of the surface charge density for Au_DMPC-DMPE, Au_DMPE-DMPC and Au_PCPE$_{MIX}$ films supported on a Au(111) electrode in 0.1 M NaF electrolyte solution at 20°C. Insert: Surface pressure of these films in the same experimental conditions.

A new set of experiments was performed in which the bilayer was remade for a range of potential steps. Figure 5.13 shows the charge density data as a function of the applied potential for these bilayers. As a result of this careful measurement process, the charge density data are remarkably similar and within the error bars of the corresponding asymmetric bilayers and demonstrate that no significant transmembrane migration of DMPC or DMPE occurs.

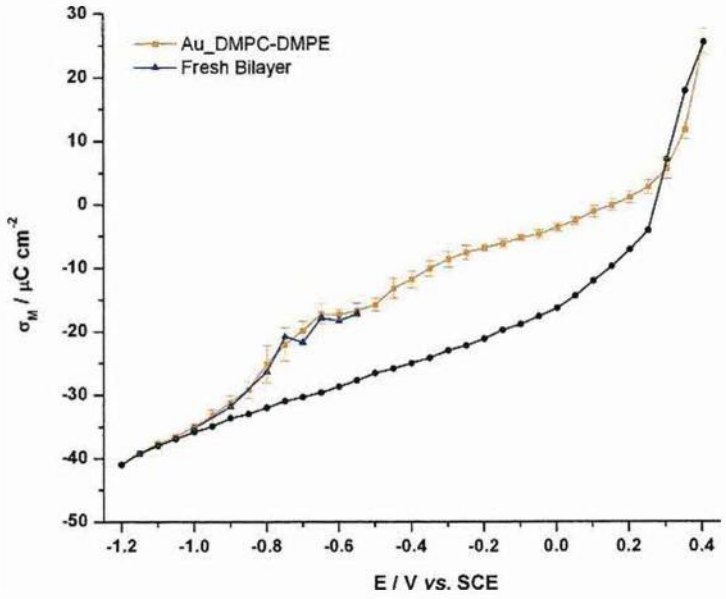

Figure 5.13: Surface charge density for a bare Au(111) electrode, asymmetric bilayer of Au_DMPC-DMPE and point by point freshly prepared Au_DMPC-DMPE on a Au(111) electrode in 0.1 M NaF electrolyte solution at 20°C.

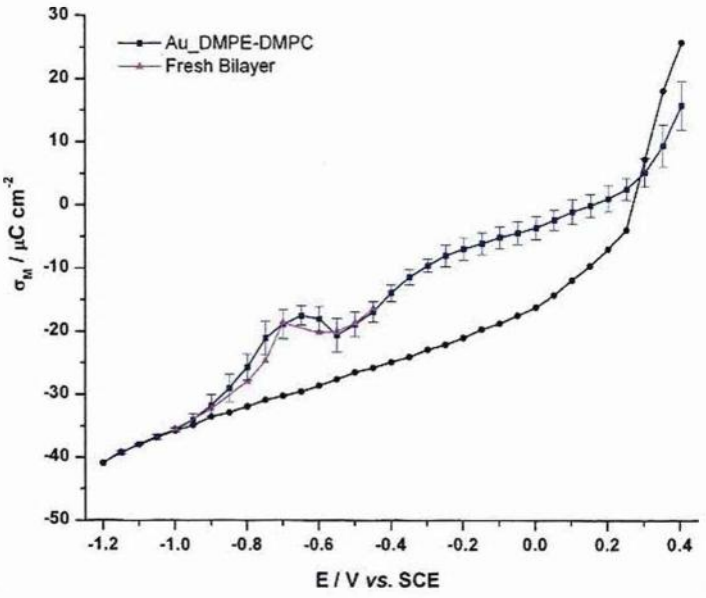

Figure 5.14: Surface charge density for a bare Au(111) electrode, asymmetric bilayer of Au_DMPE-DMPC and point by point freshly prepared Au_DMPE-DMPC supported on a Au(111) electrode in 0.1 M NaF electrolyte solution at 20°C.

5.4.2 Asymmetric Bilayers Between DMPS and DMPE

In the following study of asymmetric bilayers, phospholipids with similar headgroup size but different nett charge were used. Three different asymmetric bilayers are compared in Figure 5.15: Au_DMPE-DMPS, Au_DMPS-DMPE and Au_PSPE$_{MIX}$. In the first film, DMPE was the inner leaflet and DMPS was the monolayer in contact with the electrolyte solution. The second asymmetric bilayer was deposited in the opposite way with respect to the first mentioned film. For the third film, DMPE and DMPS were mixed in a 1:1 ratio to deposit a mixed bilayer on the gold electrode at a surface pressure of 50 mN m^{-1}. The methodology used for the deposition of all the bilayers was the LB-LS technique.

Chronocoulometry studies of these different systems show a similar trend in the charge density on the metal surface. The adsorption of Au_DMPE-DMPS and Au_DMPS-DMPE bilayers start at around the same potential, E≈ -0.9 V. At E > -0.9 V, σ_M became more positive for Au_DMPS-DMPE but parallel for each asymmetric bilayer, indicating that the position of the phospholipid affects the electrochemical behaviour of the bilayer. At a very positive potentials σ_M tended to merge. Au_PSPE$_{MIX}$ bilayer had unexpected behaviour, very similar to Au_DMPE-DMPS film except that the film adsorption started at a few mV earlier than the respective asymmetric films.

A negative shift of the E_{pzc} is caused by the adsorption of the bilayer on the electrode. The E_{pzc} for Au_DMPE-DMPS and Au_PSPE$_{MIX}$ is similar $E_{pzc} \approx +0.03$ V and this became more negative for Au_DMPS-DMPE $E_{pzc} \approx -0.04$ V. This change in the pzc could indicate an increase in the permanent dipole of the bilayer when DMPS is in the inner leaflet. This change in the dipole might be induced by a change in the headgroup orientation to more parallel orientation.

The surface pressure plot shows higher values of π when DMPS is in the inner leaflet. If the inner leaflet changes the orientation of the headgroups, the negative charge of the DMPS, which is lying on the metal, is effectively screened by the positive charge on the metal of approximately the same absolute magnitude. The DMPE leaflet is also screened by counterions from the solution. The film would be stabilized by van der Waals forces between closely packed hydrocarbon tails increasing π [20]. These graphs can be seen in the inserts to Figure 5.15.

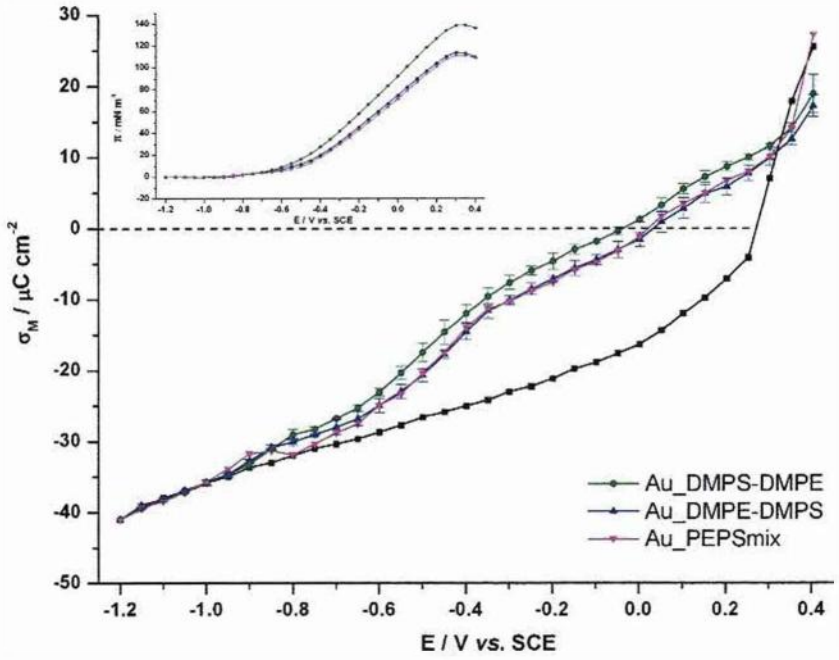

Figure 5.15: Comparison of the surface charge density for Au_DMPS-DMPE, Au_DMPE-DMPS and Au_PSPE$_{MIX}$ films supported on a Au(111) electrode in 0.1 M NaF electrolyte solution at 20°C. Insert: Surface pressure of these films in the same experimental conditions.

Freshly prepared Au_DMPS-DMPE bilayers were used for a few potential steps in order to study the possibility of translocation of the lipids. The surface charge on the electrode for the Au_DMPS-DMPE film is negative at E< -0.05 V; this repulsive charge density might force the movement of the negatively charge phospholipids from the inside leaflet to the outside leaflet. Figure 5.16 shows the surface charge density for four different step potentials in which the bilayer has been freshly made for each potential. All the results were within the error bar for the chronocolumetry measurement of the Au_DMPS-DMPE film, indicating that DMPS is not forced to migrate by the repulsion of the negative density charge on the electrode.

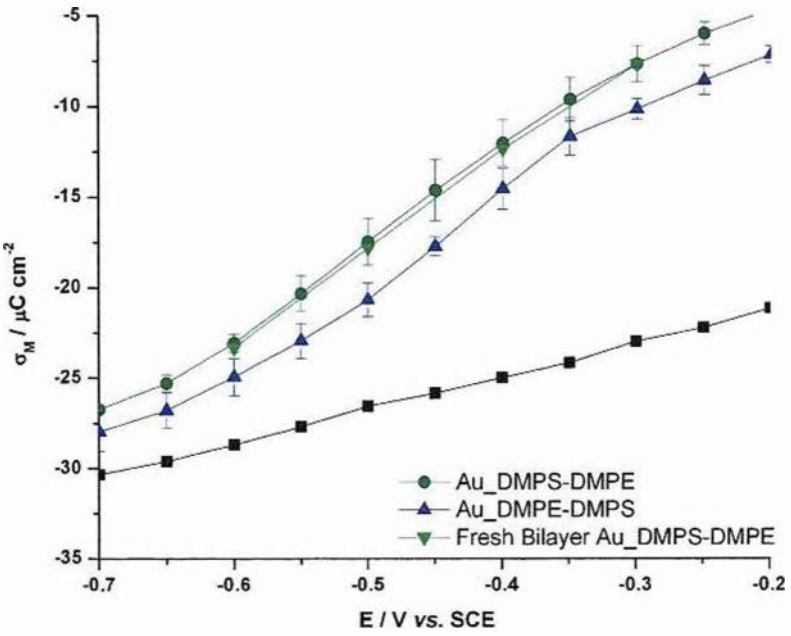

Figure 5.16: Comparision of the surface charge density for a bare Au(111) electrode and Au_DMPS-DMPE, Au_DMPE-DMPS and point by point freshly prepared Au_DMPS-DMPE on a Au(111) electrode in 0.1 M NaF electrolyte solution at 20°C.

5.4.3 Asymmetric Bilayers Between DMPC and DMPS

The last electrochemical study of asymmetric bilayers was carried out with DMPC and DMPS. In this kind of bilayer, size and nett charge of the headgroup were studied. As previously, three different asymmetric bilayers were compared and the results are presented in Figure 5.17: Au_DMPC-DMPS, Au_DMPS-DMPC and Au_PSPC$_{MIX}$.

Within the error bars, there is not a significant difference between the three curves at a potential between -1.2 V < E < -0.5 V, indicating that the onset of the adsorption is independent of the asymmetry. For bilayers adsorbed on the electrode surface at potentials -0.55 V < E < 0.5 V, σ_M was slightly more negative for Au_DMPS-DMPC. Around E= 0 V and towards positive potentials the σ_M merged.

The E_{pzc} was shifted to negative potentials for the different films, a difference of 0.05 V was found between Au_DMPS-DMPC and Au_DMPC-DMPS. For the Au_PSPC$_{MIX}$ film the E_{pzc} = 0.075 V. These three different E_{pzc} can be related to the

different asymmetry of each bilayer but more details about how the electric field affects their structure and orientation should be completed by additional studies such as *in situ* PM-IRRAS or *in situ* neutron reflectivity.

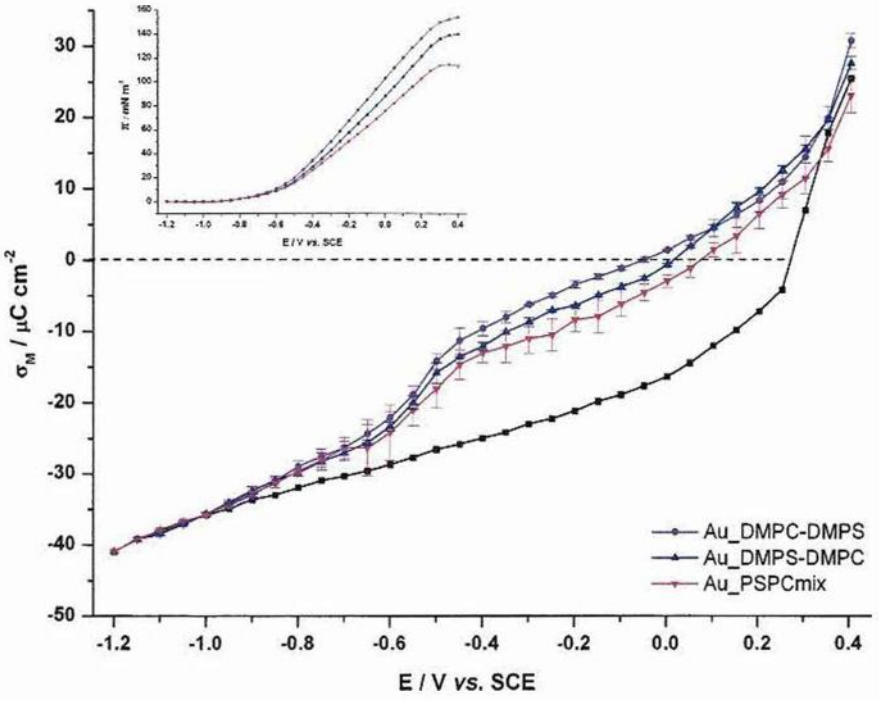

Figure 5.17: Comparison of the surface charge density for Au_DMPC-DMPS, Au_DMPS-DMPC and Au_PSPC$_{MIX}$ films supported on a Au(111) electrode in 0.1 M NaF electrolyte solution at 20°C. Insert: Surface pressure of these films in the same experimental conditions

In summary, we have compared the asymmetry of different LBLS phospholipid bilayers at Au(111) electrode by electrochemical techniques. The characterization of these bilayers provide information concerning the adsorption/desorption behaviour and phase transitions of the lipids. It has been shown that the response of the bilayer is dependent on the asymmetry and the phospholipids used.

References:

1. A. Nelson, *Curr. Opin. Colloid Interface Sci.*, 2010, **15**, 455-466.
2. I. Burgess, M. Li, S. L. Horswell, G. Szymanski, J. Lipkowski, J. Majewski and S. Satija, *Biophys. J.*, 2004, **86**, 1763-1776.
3. X. Bin, S. L. Horswell and J. Lipkowski, *Biophys. J.*, 2005, **89**, 592-604.
4. I. Zawisza, X. M. Bin and J. Lipkowski, *Langmuir*, 2007, **23**, 5180-5194.
5. F. T. Buoninsegni, R. Herrero and M. R. Moncelli, *J. Electroanal. Chem.*, 1998, **452**, 33-42.
6. S. L. Horswell, V. Zamlynny, H.-Q. Li, A. R. Merrill and J. Lipkowski, *Faraday Discuss.*, 2002, **121**, 405-422.
7. X. Bin, I. Zawisza, J. D. Goddard and J. Lipkowski, *Langmuir*, 2005, **21**, 330-347.
8. X. Bin and J. Lipkowski, *J. Phys. Chem. B*, 2006, **110**, 26430-26441.
9. M. Li, M. Chen, E. Sheepwash, C. L. Brosseau, H. Li, B. Pettinger, H. Gruler and J. Lipkowski, *Langmuir*, 2008, **24**, 10313-10323.
10. H. I. Petrache, S. Tristram-Nagle, K. Gawrisch, D. Harries, V. A. Parsegian and J. F. Nagle, *Biophys. J.*, 2004, **86**, 1574-1586.
11. R. N. A. H. Lewis and R. N. McElhaney, *Biophys. J.*, 1993, **64**, 1081-1096.
12. R. N. A. H. Lewis, D. Zweytick, G. Pabst, K. Lohner and R. N. McElhaney, *Biophys. J.*, 2007, **92**, 3166-3177.
13. R. N. A. H. Lewis and R. N. McElhaney, *Biochim. Biophys. Acta, Biomembr.*, 2009, **1788**, 2069-2079.
14. J. Lipkowski and L. Stolberg, *Adsorption of molecules at metal electrodes*, Wiley-VCH, New York, 1992.
15. L. Becucci, M. R. Moncelli, R. Herrero and R. Guidelli, *Langmuir*, 2000, **16**, 7694-7700.
16. J. Lipkowski, C. Nguyen Van Huong, C. Hinnen, R. Parsons and J. Chevalet, *J. Electroanal. Chem. Interfac.*, 1983, **143**, 375-396.
17. T. Starke-Peterkovic and R. Clarke, *Eur. Biophys. J.*, 2009, **39**, 103-110.
18. R. Guidelli, G. Aloisi, L. Becucci, A. Dolfi, M. Rosa Moncelli and F. Tadini Buoninsegni, *J. Electroanal. Chem.*, 2001, **504**, 1-28.

19. I. Zawisza, X. Bin and J. Lipkowski, *Bioelectrochem.*, 2004, **63**, 137-147.

20. I. Burgess, V. Zamlynny, G. Szymanski, J. Lipkowski, J. Majewski, G. Smith, S. Satija and R. Ivkov, *Langmuir*, 2001, **17**, 3355-3367.

CHAPTER 6: *IN SITU* PM-IRRRAS OF DMPS BILAYER

6.1. Introduction

The creation of phospholipid bilayers on metal supports provides the advantage of applying voltages to create an electric field across the lipid films which can be compared with those occurring in natural cell membranes. Our aim is to study the influence of the electric field on the structure and organization of phospholipid bilayers supported on Au(111).

In this chapter, determination of the orientation and conformation of DMPS films is carried out with *in situ* PM-IRRAS. This chapter is divided into four sections: First at all, the determination and utilization of the optical constants for DMPS; secondly, C-H stretching region is studied in order to determine the tilt angle and the conformation of the hydrocarbon chain; thirdly, the hydration of the interfacial region of the DMPS molecules is shown by studying the carbonyl stretching vibrations; finally, the study of the asymmetric and symmetric phosphate stretching vibrations, which gives information on the degree of hydration of the headgroup.

6.2. Optical constants

The optical constants were determined from transmittance spectra using the optical matrix approach described in Chapter 3. The optical constants of the DMPS bilayer in D_2O (3000 - 2800 cm^{-1} and 1800 - 1425 cm^{-1}) and H_2O (1270 - 1170 cm^{-1}) are shown in Figure 6.1.

In the C-H stretching region four overlapping bands are seen. These correspond respectively to methyl asymmetric $\nu_{as}(CH_3)$ at 2956.8 cm^{-1}, methylene asymmetric $\nu_{as}(CH_2)$ at 2917.8 cm^{-1}, methyl symmetric $\nu_s(CH_3)$ at 2872.4 cm^{-1} and methylene symmetric $\nu_s(CH_2)$ stretches at 2850.5 cm^{-1} [1] The shoulders at ≈2929 and 2898.5 cm^{-1} correspond to Fermi resonances between the overtones of the symmetric bending mode and the symmetric methyl and methylene stretching modes [1]. Figure 6.1b shows the optical constants of DMPS in the range between 1800 and 1425 cm^{-1}. A peak is observed at ≈1739 cm^{-1} which corresponds to the C=O stretching vibration band; as shown it can be deconvoluted into two superimposed bands. The band at higher-wavenumber (1741 cm^{-1}) corresponds to

less hydrated C=O groups and the shoulder at lower-wavenumber (1727 cm^{-1}) is characteristic of the hydrated ester carbonyl group [2, 3]. At around 1622 cm^{-1} the asymmetric vibration band of C-O-O^- appears at the expected wavenumber for D_2O solution [4]. The methylene scissoring mode, $\gamma(CH_2)$ occurs at 1468 cm^{-1} with a small shoulder at 1462 cm^{-1} which corresponds to the asymmetric bending band, $\delta_{as}(CH_2)$ [1, 5]. Figure 6.1c shows the asymmetric stretching vibration of the phosphate group $\nu_{as}(PO_2^-)$ in H_2O in the range between 1270 and 1170 cm^{-1}. This band overlaps with the band at ≈1210 cm^{-1}, which originates from the C-O-C asymmetric stretching mode in the ester groups of the DMPS molecule [6].

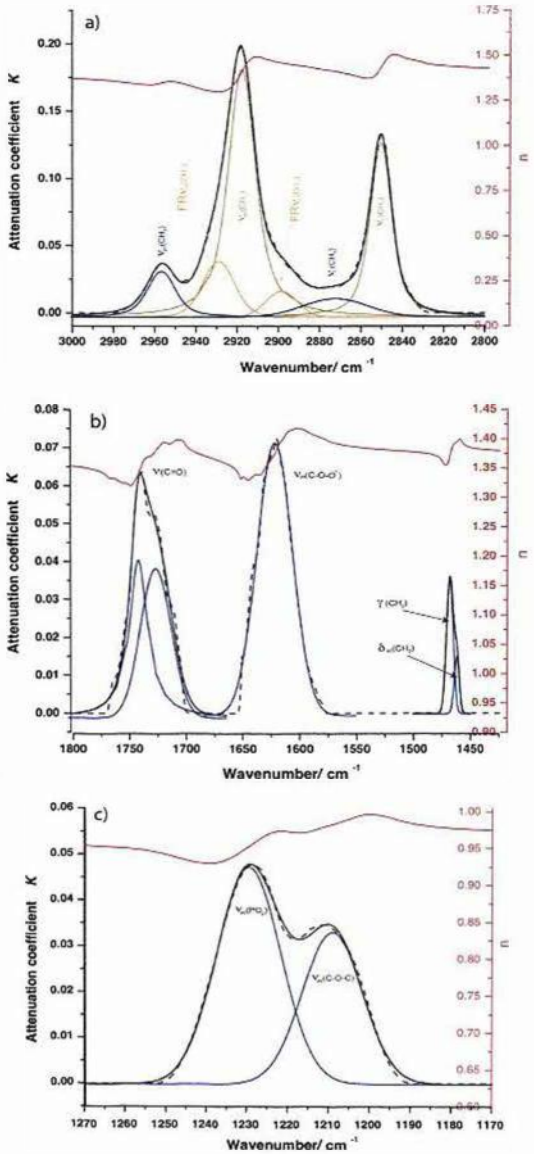

Figure 6.1: Isotropic optical constants of DMPS calculated from the transmittance of its 0.575 % v/v for D_2O (a, b) and 0.532 % v/v for H_2O solution (c).

6.3. Acyl Chain Region. Acyl C-H Stretching Modes

DMPS contains a total of 27 methylene groups. 24 of them are divided between its two acyl chains; there are two methylene groups in the glycerol part and another in the headgroup. The majority of the CH_2 groups are located in the acyl chains, thus any change in the methylene bands can be associated to the CH_2 groups from the lipid acyl chains.

To determine the conformation, physical state and the tilt angle of the acyl chains within the DMPS bilayer, the PEM was set at 2900 cm^{-1} for the study of the C-H stretching vibration bands. These bands are considered conformationally sensitive and respond to changes in the state (from *trans* to *gauche*) of the lipid acyl chain. Phase transitions of the acyl chains are accompanied by changes in the peak position and bandwidth of the methylene stretching vibrations thus, $\nu_{as}(CH_2)$ and $\nu_s(CH_2)$ can be used to detect and monitor phase transitions [7].

The deposition of the DMPS bilayer onto a Au(111) electrode and the optimization of the spectroelectrochemical cell was described in detail in Chapter 3. Figure 6.2 shows the comparison of the experimental and calculated reflectivity spectra. A good agreement between these two spectra takes place at an angle of $\theta = 51.1°$ and a gap thickness (the electrolyte thickness between the working electrode and the prism) of 2.1 μm. Once the spectroelectrochemical was set to the optimum incident angle and the thin cavity thickness the spectra were recorded for electrochemical study of DMPS bilayer. The potential was set initially to $E_i = 0.4$ V *vs.* Ag/AgCl and was stepped in the cathodic direction by 0.1 V increments until the final potential $E_f = -1$ V was applied.

The experimental spectra were corrected to remove the artefact imposed by the PEM and to eliminate the difference in throughput of the optical bench for s- and p-polarized radiation. To eliminate the background, a baseline was created using spline interpolation and subtracted from the corrected spectra. The processed spectra were then employed for determination of the tilt angles of the transition dipoles.

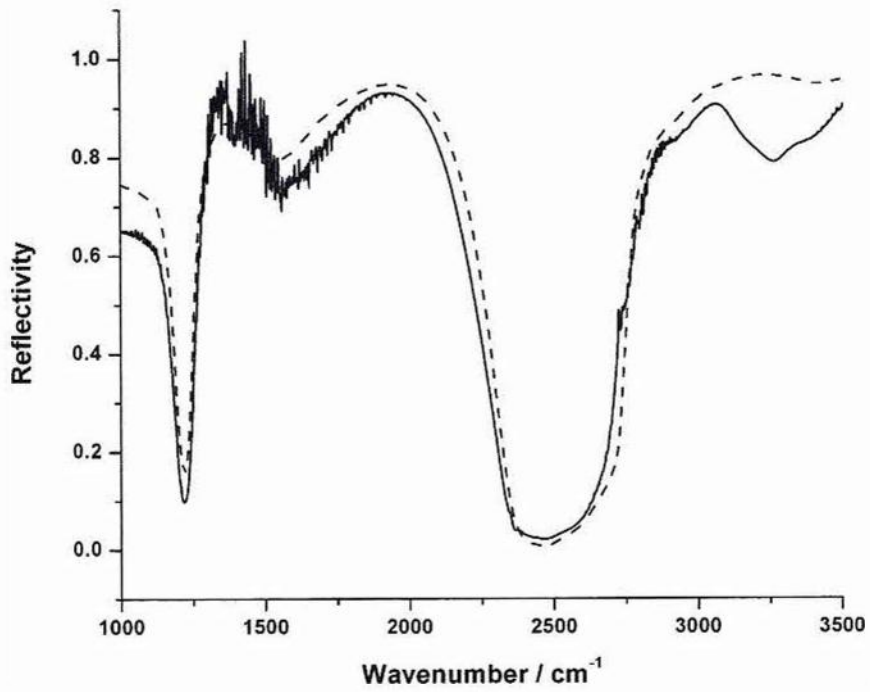

Figure 6.2: Reflectivity spectra for a thin layer cavity spectroelectrochemical cell ($BaF_2/D_2O/Au$). The experimental spectrum is represented by a solid line and the dashed line represents the calculated spectrum (θ = 51.1° and d = 2.1 μm).

Figure 6.3 shows the *in situ* PM-IRRA spectra of a DMPS bilayer recorded at progressively negative electrode potentials. The positions of the bands are basically the same as reported in the literature for multilayers of DMPS on Ge substrates [4]. It can be seen that the intensities of the methylene stretching bands are dependent on the applied potential, indicating that the electric field induces reorientation of the acyl chains. Major changes in the plots are observed at E< -0.2 V, where increases in the intensity of the methylene bands are easily identified. The intensities of the methyl bands are very similar in the whole range of potentials. Deconvolution of the spectra is necessary to determine accurately the changes in position and intensity of the bands, especially the methylene bands due to the superposition with the Fermi resonance bands. The Voigt function was used to fit the different peaks in the experimental spectra. The positions and full-widths at half-maximum (FWHM) of the methylene stretching bands against the applied potential are shown in Figure 6.4.

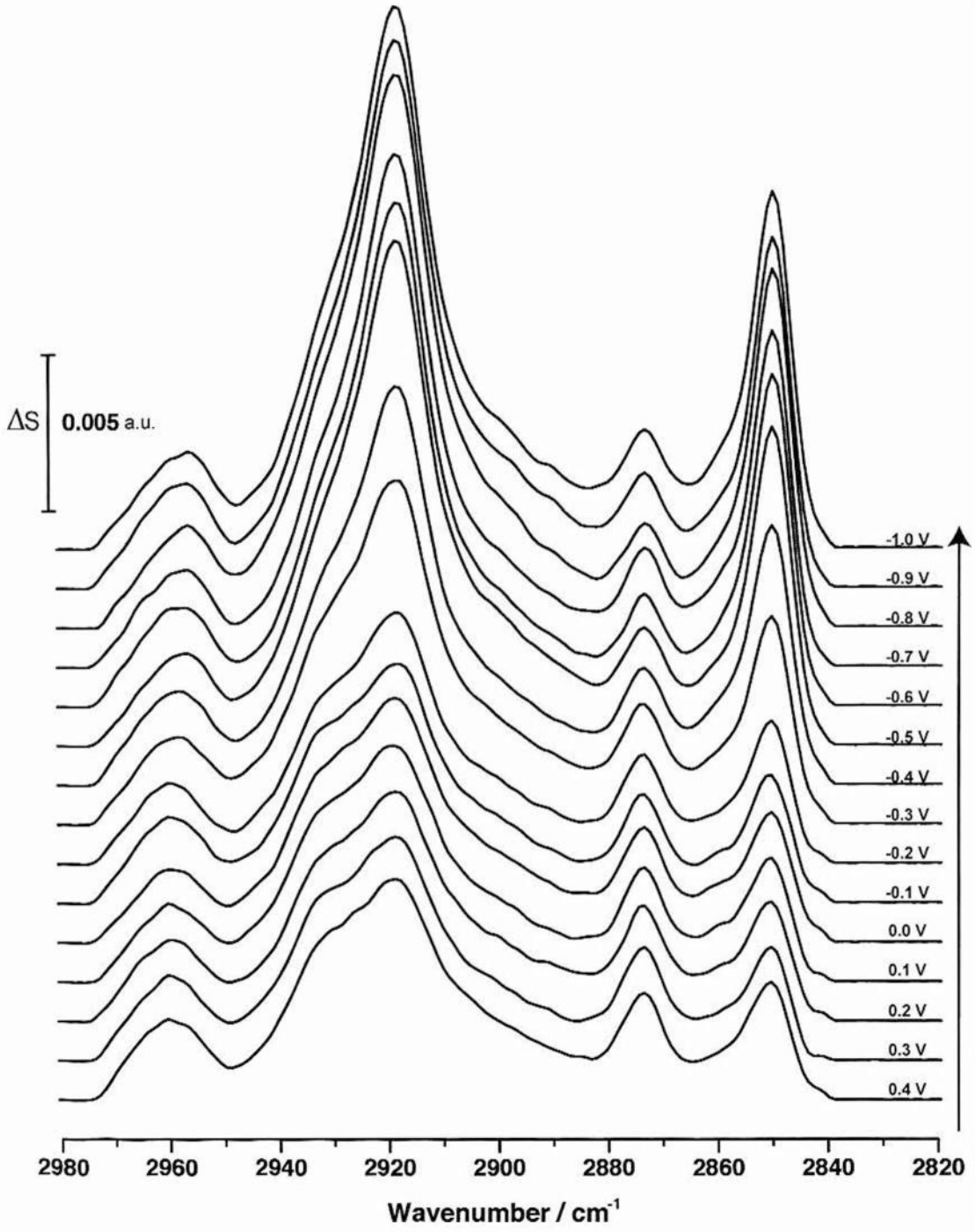

Figure 6.3: *In situ* PM-IRRA spectra for the C-H stretching region of a DMPS bilayer on a Au(111) electrode in a 0.1 M NaF/D_2O solution at the indicated potentials.

The $\nu_{as}(CH_2)$ band is the strongest band in the spectra; its position and FWHM depends on the electrode potential as shown in Figure 6.4. At E> -0.2 V the graph shows that the centre of the $\nu_{as}(CH_2)$ band has the lowest wavenumber values

indicating that the bilayer is more ordered when it is adsorbed on the electrode surface. As the potential becomes more negative, the wavenumber increases, indicating that the order of the adsorbed bilayer is slightly altered. It reaches a stable conformation at E< -0.4 V where it shows a constant position indicating that at very negative potentials the arrangement of the DMPS film is not further altered. The FWHM and the area of the $\nu_{as}(CH_2)$ band shows that towards negative potentials, the band progressively become narrower and more intense (Figure 6.5).

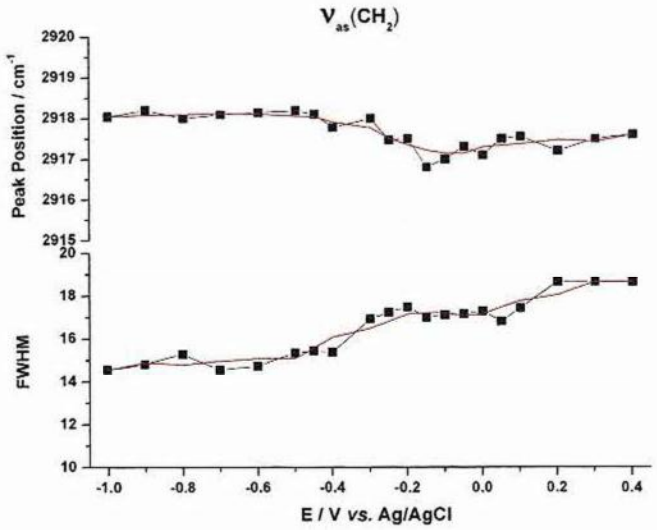

Figure 6.4: Plot of the position and FWHM of $\nu_{as}(CH_2)$ stretching bands *vs.* potential for an *in situ* PM-IRRAS of DMPS bilayer in D_2O.

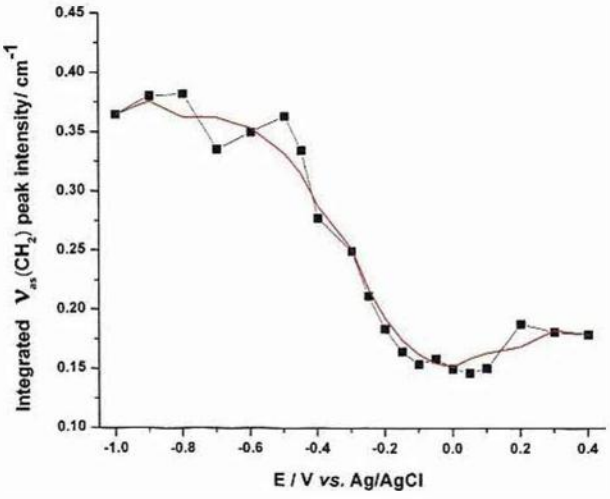

Figure 6.5: Plot of the integrated $\nu_{as}(CH_2)$ peak intensity *vs.* potential for *in situ* PM-IRRAS of a DMPS bilayer in D_2O.

A simulated spectrum of randomly distributed DMPS molecules in a 7.4 nm thick film in D_2O ($\theta = 51.1°$ and $d = 2.1$ μm) is shown in Figure 6.7. This spectrum was obtained using the equation (Eq. 3.9) and the procedure described in Chapter 3. The position of the methylene bands from this spectrum are used to compare with our experimental results (Figure 6.6). The molecules of DMPS randomly distributed in the bilayer showed a wavenumber for $\nu_{as}(CH_2)$ of 2920.9 cm^{-1} and for $\nu_s(CH_2)$ of 2851.8 cm^{-1}. The values of the methylene positions for a bilayer with randomly distributed DMPS are higher than the experimental positions, which indicates that the DMPS molecules are highly ordered within the experimental bilayer.

The position of the methylene bands for acyl chains in the gel state are reported to be centred lower than 2920 cm^{-1} for $\nu_{as}(CH_2)$ and 2850 cm^{-1} for $\nu_s(CH_2)$ [8-10]. In Figure 6.6, the positions of a DMPS bilayer supported on Au(111) over a range of potentials shows that for the $\nu_{as}(CH_2)$ and the $\nu_s(CH_2)$ are lower than 2918 cm^{-1} and 2851.4 cm^{-1}, respectively. This indicates that the experimental DMPS film has stretched acyl chains with a very few *gauche* conformations at potentials in which the bilayer is adsorbed on the gold electrode.

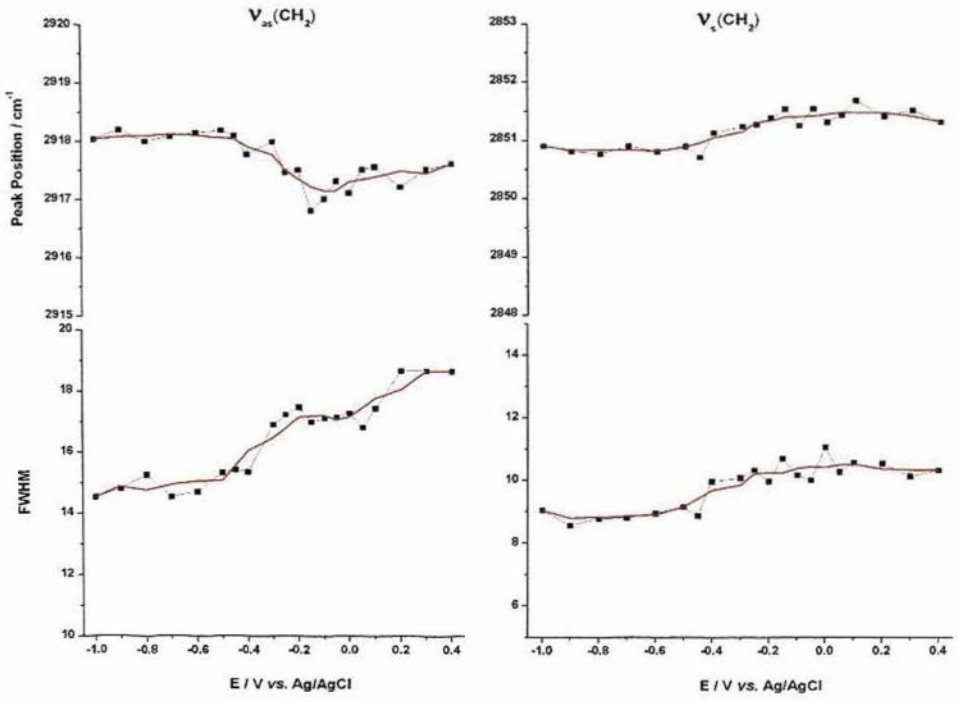

Figure 6.6: Plot of the position and FWHM of $\nu_{as}(CH_2)$ and $\nu_s(CH_2)$ stretching bands *vs.* potential for *in situ* PM-IRRAS of DMPS bilayer in D_2O.

Towards negative potentials the position of the asymmetric vibration band seem to have different trend, which might be due the influence of the Fermi resonance overtones vibrations. More precise information arises from the symmetric vibration band, which is not affected by the contribution from other bands thus, this band will be the marker for the state of the acyl chains in the DMPS bilayer.

The rate of motion of the molecular vibration is determined by the bandwidth of the IR bands; if the bandwidth increases, the motional rate increases [9]. In general, *in situ* PM-IRRAS of DMPS shows that C-H bands are narrower in comparison with the simulated spectra [FWHM of 19.1 for $\nu_{as}(CH_2)$ and 13.4 for $\nu_s(CH_2)$], thus the experimental bilayer has lower mobility, indicating that the acyl chains have a conformationally restricted structure towards negative potentials, where no major changes in the tilt angle are observed.

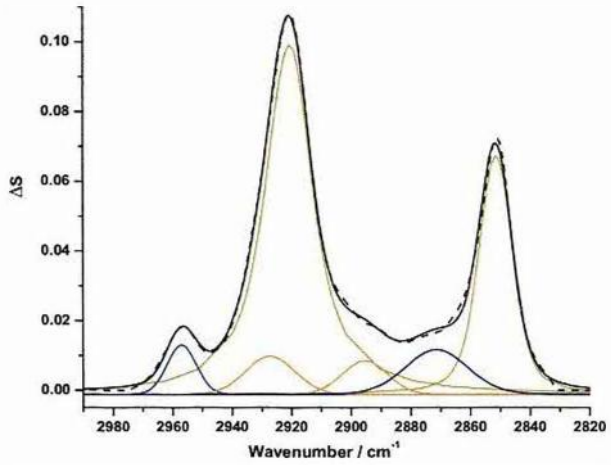

Figure 6.7: Simulated spectra of randomly distributed DMPS molecules of thickness 7.4 nm on a Au substrate in D_2O.

In spite of the existence of a few *gauche* conformers, the tilt angle of DMPS molecules can be calculated precisely following the procedure that was previously explained in Chapter 3. Determination of the orientation of the DMPS molecules involves the comparison of the experimental spectra with the simulated spectra of DMPS in D_2O. The calculation was carried out using the experimental integrated band intensity from the corrected spectra and the calculated integrated band intensity from the simulated spectra determined (from the optical constants) for randomly

oriented DMPS. The values are shown in Figure 6.8.

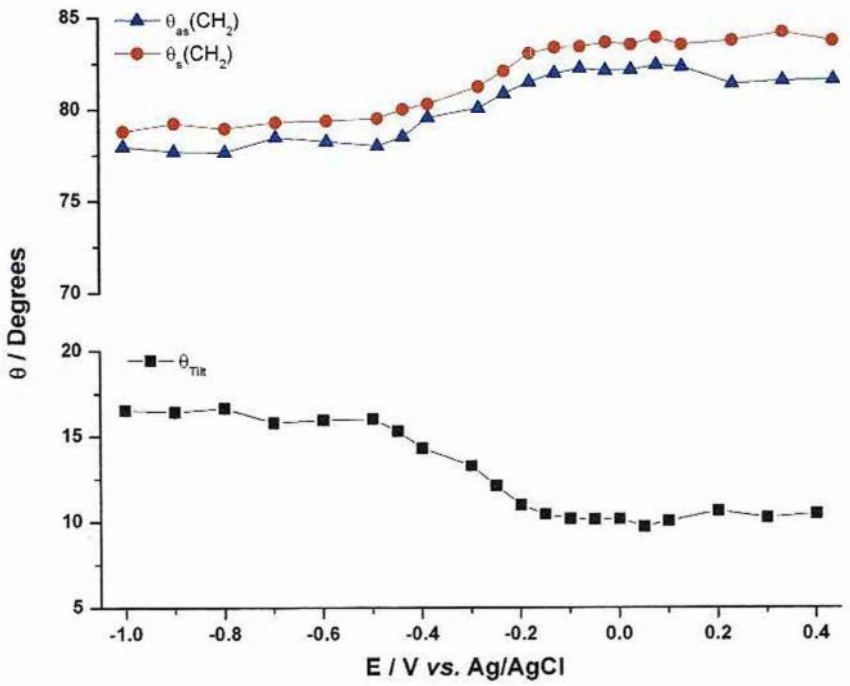

Figure 6.8: Potential dependence of the angle (θ) between the direction of the transition dipole moment and the surface normal for the acyl chain of a DMPS film at the Au(111) surface, $\nu_{as}(CH_2)$ and $\nu_s(CH_2)$ and of the angle between the chain and the surface normal.

At potentials between -0.4 V < E < 0.4 V electrochemical studies demonstrated that the DMPS film is adsorbed on the gold surface (Figure 6.9). A compact and stable bilayer is formed on the electrode at -0.1 V < E < 0.4 V: within this range the chains have an average tilt angle of 10.2°±0.3, which means that DMPS acyl chains are oriented upright, more upright than those reported for LBLS DMPC films (25°) [11]. The tilt angle starts to increase in the range of -0.4 V < E < -0.1 V, showing that before starting to desorb, the acyl chains slightly tilt (from ≈10° to ≈16°). The increase in the chain tilt angle could be due to swelling of the bilayer which forces the chain to tilt or due to structural changes occurring when higher electric fields corresponding to potentials negative of -0.15 V were applied, which open spaces for the penetration of the solvent. It could also arise if the headgroups reorient at applied fields in order to align the P^--N^+ dipoles with the field; such a change would also force the rest of the

molecule, including the hydrocarbon chains, to change orientation.

A decrease in the σ_M was observed in chronocoulometry experiments at E< -0.4 V. At these potentials, the bilayer starts to desorb and a constant tilt angle is observed. The acyl chains are oriented with respect to the metal surface normal at an average angle of 16.2°±0.3, which is comparable with a value of 17°±3 reported for LBLS DMPC films[11]. This indicates in our case a decrease in the packing density when the bilayer is desorbed, in contrast with DMPC where an increase was reported. The detached films have similar tilt angle so the difference in trend observed is mainly due to the difference in structure of the directly adsorbed films.

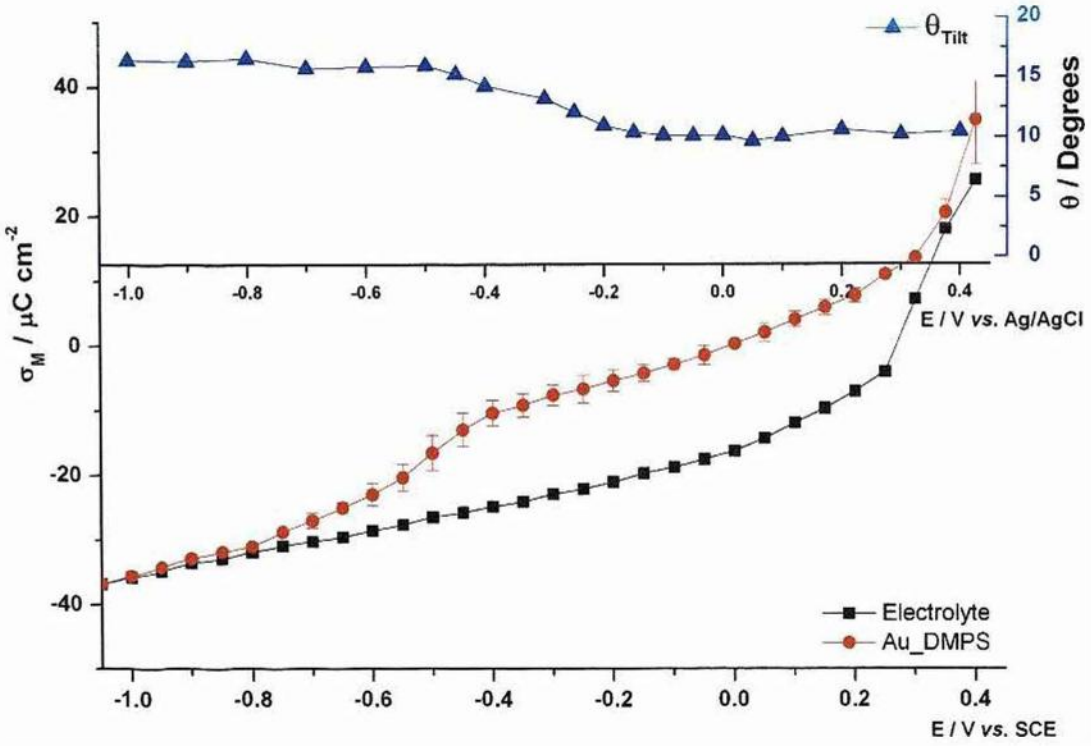

Figure 6.9: Comparison plot of the charge density (σ_M) and tilt angle of the acyl chains (θ) *vs.* potential.

In summary, from positive to negative potentials, a DMPS bilayer shows an increase in the chain tilt angle and decrease in the bandwidth and the position of the $\nu_s(CH_2)$ band. Studies on LBLS DMPC bilayers have shown a decrease in tilt angle,

peak position and bandwidth suggesting that the different molecular structure between DMPC and DMPS gives rise to the difference in the trend for the tilt angle. The shape of the DMPS molecule is smaller than DMPC; if the headgroups are oriented in a similar way, its cylindrical shape would result in fairly upright acyl chains, which is observed for the adsorbed state: chains are upright compared with DMPC. At this state, the DMPS bilayer is well-packed with long, stretched chains, indicated by the low peak position. Towards negative potentials, the negative charge on the electrode may force away the phosphate group, which would then force the whole molecule to tilt, decreasing film thickness and increasing its capacitance. For the chains to keep their intermolecular interactions, they have to tilt more. Another possible situation can be new rearrangement within the headgroups after the phase transition at E≈ 0.0 V in DC experiments which may increase the chain angle. Somehow, this new configuration reduces its mobility, as indicated by a decrease in the bandwidth, and would also increase the capacitance of the bilayer-coated surface.

6.4. Interfacial Region. Carbonyl Stretching Vibrations.

The carbonyl ester band is composed of two bands, one centred at ≈1740 cm^{-1} which corresponds to the ν(C=O) stretching vibration band and the second, ν_{as}(O-C-O), centred at ≈1180 cm^{-1}.

The ν(C=O) stretching absorption band is investigated in this thesis for DMPS in D_2O because is sensitive to the to the degree of hydration of the glycerol moiety upon hydrogen bonding by water (or other hydrogen donor) to the ester C=O group [9, 12]. Changes in this band are also observed in the literature due to phase transitions of the acyl chains: the hydration of the band is increased when they are in the gel state and decreased when in the liquid-state [7].

This band is usually a superposition of two underlying bands. The higher-wavenumber band has been reported to be due to the non-hydrogen bonded carbonyl group and the lower-wavenumber band is characteristic of a higher degree of hydration of ester moieties. Reported FT-IR studies using ^{13}C labelled *sn-1* or *sn-2* acyl chains in phospholipids have shown that the differentiation between the two ester carbonyls is also possible for the hydrogen-bonded and non-hydrogen-bonded

situations [2, 9].

In order to obtain the IR absorption spectra of ν(C=O) bands, the PEM was set up at 1600 cm^{-1}. The optimum conditions used for this experiment were given by the agreement between the experimental and the calculated reflectivity at this chosen wavenumber (θ = 60.6° and d = 4 μm).

After the spectroelectrochemical cell was optimized the spectra were recorded as mentioned previously in the spectroelectrochemical studies of C-H stretching bands. A baseline created using the spline interpolation was subtracted from the corrected spectra; the subtracted data are plotted in Figure 6.10.

The first spectrum recorded was at an applied potential of E_i = 0.4 V. This spectrum shows a peak centred at ≈1740 cm^{-1} with a shoulder at 1726 cm^{-1}. A small vibrational band with frequency down to ≈1709 cm^{-1} is also seen; a similar band has been reported be the result of one of C=O groups forming hydrogen bonds with two molecules of water [13]. The intensity and position of these peaks do not show any important change in their intensity in the range of potentials in which the film is adsorbed onto the electrode (-0.15 V < E < 0.4 V). Towards negative potentials the intensity of the shoulder peak at 1726 cm^{-1} and the vibrational band at ≈1709 cm^{-1} increase and superimpose on each other to form one broader vibrational band which is centred at ≈1717 cm^{-1}.

Between -1.0 V < E < -0.15 V, only two broad bands are observed, one centred at ≈1740 cm^{-1} which is associated to the non-hydrogen bonded carbonyl group (dry band) and, the other that is centred at ≈1726 cm^{-1} assigned to the hydrogen bonded carbonyl group (hydrated band). Deconvolution of the spectra in this potential range shows that these bands are formed by two underlying bands which arise for the conformational differences between stretching vibrations of *sn*1- and *sn*2- ester carbonyl groups. The band at lower wavenumber (the hydrated band), consists of three underlying bands if the vibrational band seen at positive potentials at a frequency down to ≈1709 cm^{-1} is taken into account.

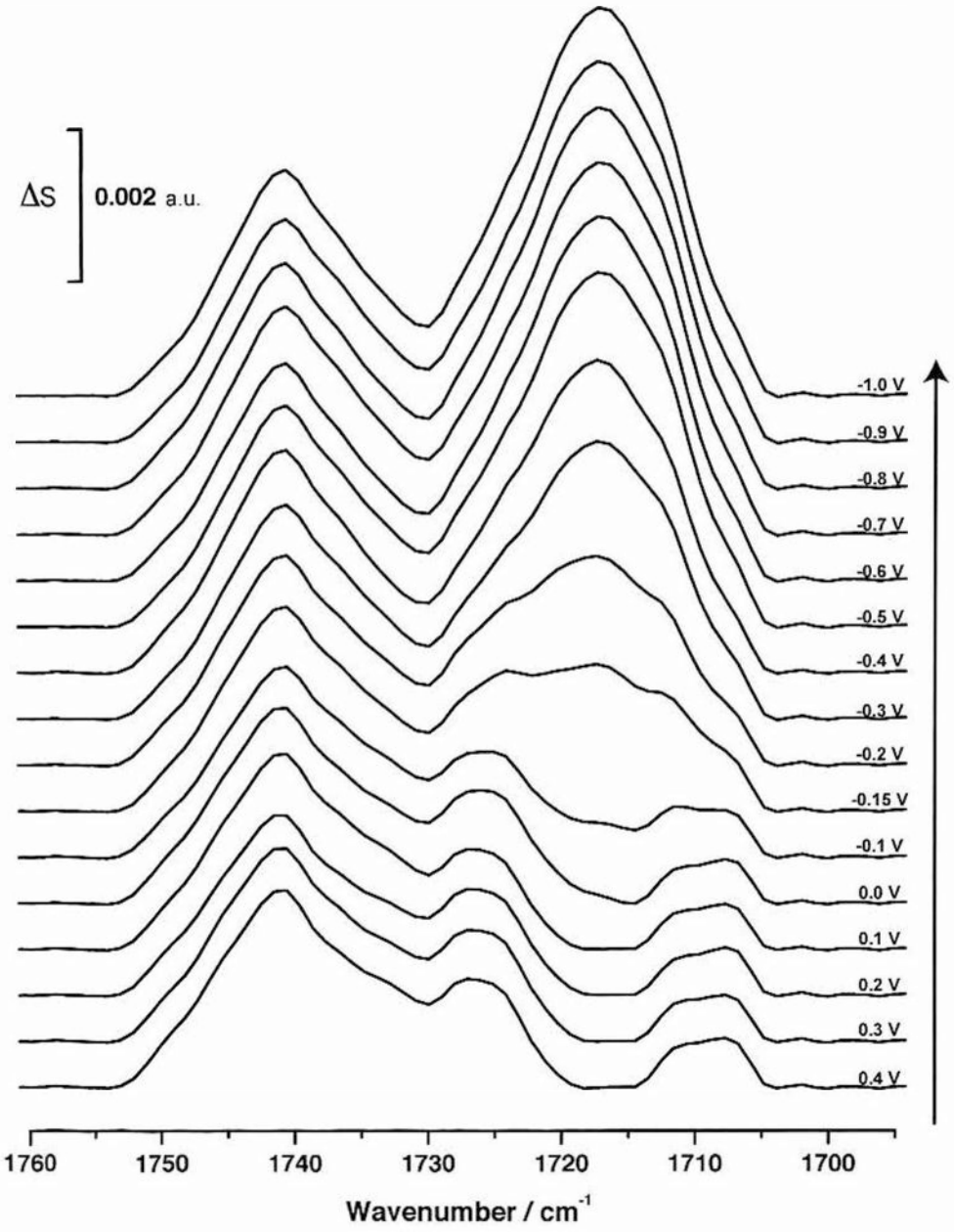

Figure 6.10: *In situ* PM-IRRA spectra for the C=O stretching region of a DMPS bilayer on a Au(111) electrode in a 0.1 M NaF/D_2O solution at the indicated potentials.

Using the Voigt function in the deconvolution of the bands, more accuracy in the position is obtained; this information is plotted in Figure 6.11.

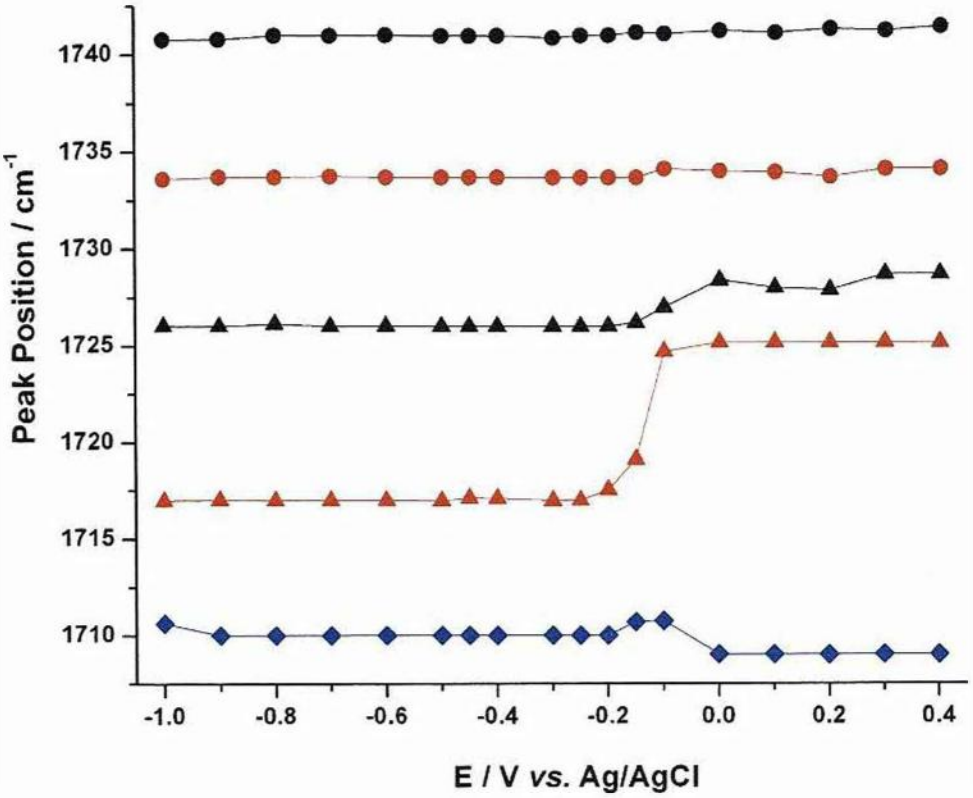

Figure 6.11: Plot of the position of the deconvolution of ν(C=O) vibration bands *vs.* potential for *in situ* PM-IRRAS of DMPS bilayer in D_2O. From top to bottom: Dry-*sn1*, Dry-*sn2*, Hydrated-*sn1*, Hydrated-*sn2* and C=O::H_2O.

At positive potentials in which the bilayer is adsorbed on the electrode surface the position of the bands seems not to change, showing the same behaviour as for the C-H vibration bands. The positions for the dry bands are constant through the whole range of potentials. After the phase transition observed at E≈0.0 V in DC experiments, the wavenumbers for the hydrated bands *sn*-1 and *sn*-2 decrease. Towards negative potentials (E< -0.2 V), a constant position of the hydrated bands *sn*-1 and *sn*-2 are observed, nevertheless the intensity increases as shown in Figure 6.12, dramatically in the case for the hydrated *sn*-2 band and slightly for the hydrated *sn*-1 band. The overall behaviour of the third band in the whole range of potentials seems not to have much influence in the global hydration of the bilayer. The difference in the bands (hydrated *sn*-1 and hydrated *sn*-2) intensity indicates a kind of asymmetric distribution of the solvent content. The *sn*-2 group is close in position to the headgroup region and so is more accessible to solvent.

Our previous studies of the DMPS in C-H stretching bands has shown a reorganization of the acyl chains which increases their tilt angle, by tilting their chains, new spaces might be opened and more solvent might penetrate into the bilayer reaching the carbonyl groups.

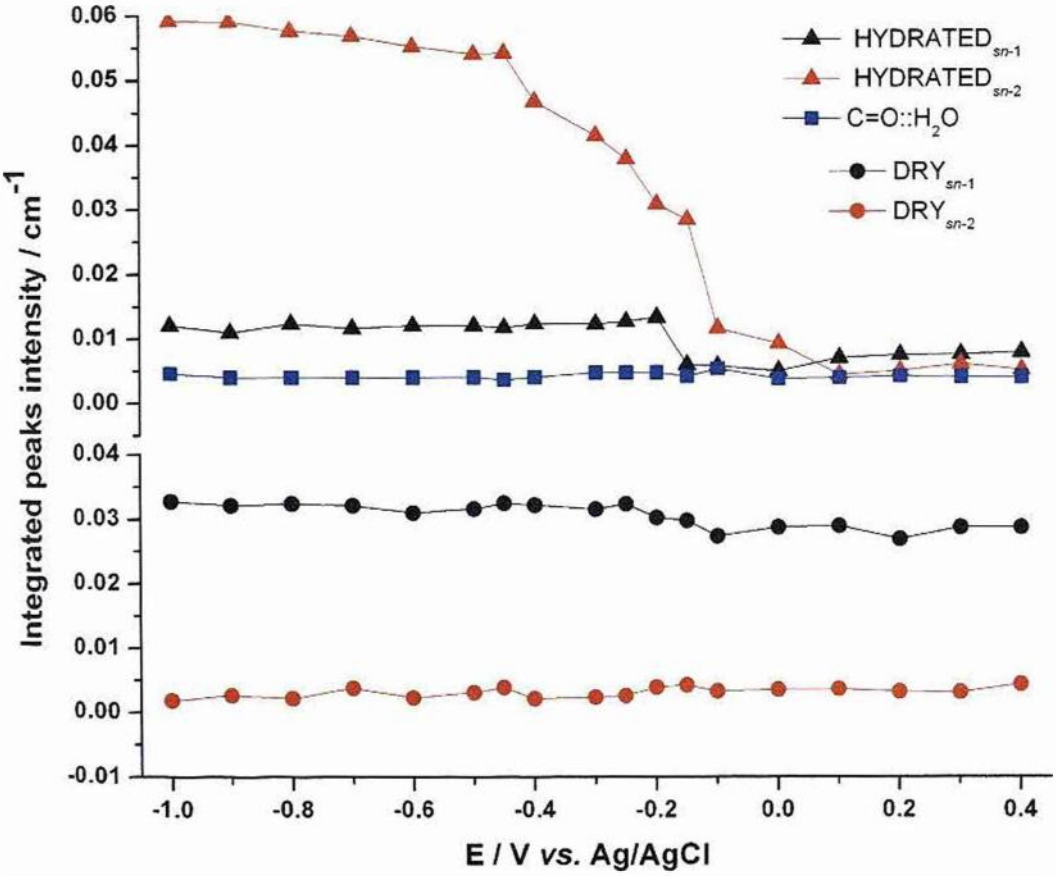

Figure 6.12: Plot of the integrated $\nu(C{=}O_{Dry})$, $\nu(C{=}O_{hydrated})$ and $\nu(C{=}O{::}H_2O)$ peaks intensity *vs.* potential for *in situ* PM-IRRAS of DMPS bilayer in D_2O.

In situ experiments of DMPS in D_2O show the influence of applied electric field under the formation of hydrogen bonds on the molecules' interfacial region. At potentials, where the bilayer is adsorbed, there is no increase in the hydration level within the film but a massive increase in the hydration is observed as the potential becomes more negative and the bilayer is desorbed from the electrode surface.

6.5. Polar Group Region. Phosphate Group Vibrations

In the study of the $\nu_{as}(PO_2^-)$ stretching band, the PEM was set up at 1100 cm^{-1} and electrolyte solution used was 0.1 M NaF in H_2O. The optimum conditions used for this experiment were θ=56.5° and d=3.5 μm. The spectra recorded were processed and background subtracted (Figure 6.13) showing that the $\nu_{as}(PO_2^-)$ vibration band is centred at ≈1231 cm^{-1} during the whole range of potentials. The bandwidth changes progressively and it becomes broader and slightly more intense towards negative potential.

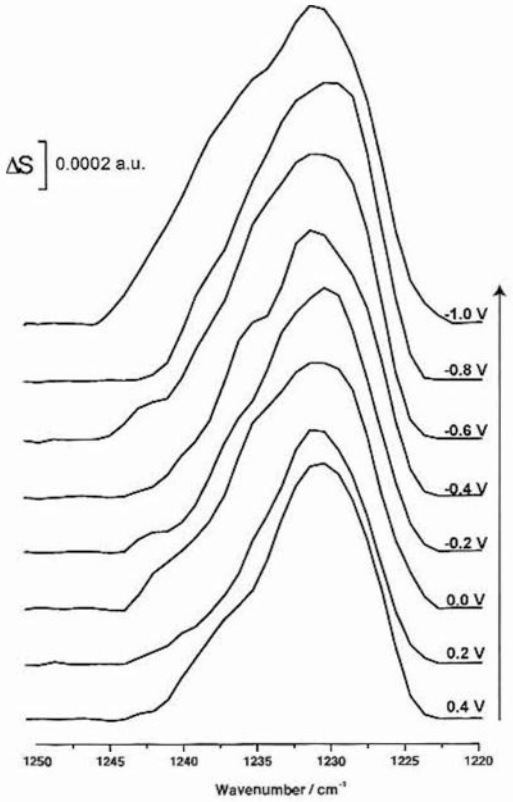

Figure 6.13: *In situ* PM-IRRA spectra for the PO_2^- asymmetric stretching band region of a DMPS bilayer on a Au(111) electrode in 0.1 M NaF/H_2O solution at the indicated potentials.

In general, the intensity of this band is not very strong and during the deconvolution, ν_{as}(O-C-O) band seems to be separated enough (≈1215 cm^{-1}) to not overlap with the $\nu_{as}(PO_2^-)$ band. Due to no major changes in the ν_{as}(O-C-O) band, we will restrict the analysis of this region of the spectrum to the discussion of the non-esterified P-O stretching bands.

The deconvolution of this band shows that $\nu_{as}(PO_2^-)$ is composed by two components, a hydrogen-bonded component and non-hydrogen bonded component as is shown in Figure 6.14. For a simulated spectrum of a DMPS bilayer in $CDCl_3$ with 10% CD_3OD, the non-hydrogen bonded component is very intense and shifts the overall band to higher wavenumbers ≈1240 cm^{-1}. The spectra of an *in situ* DMPS bilayer in H_2O show a very intense hydrogen-bonded component which makes a constant position of the band at ≈1231 cm^{-1}, indicating that phosphate groups are hydrogen bonded during all the experiment.

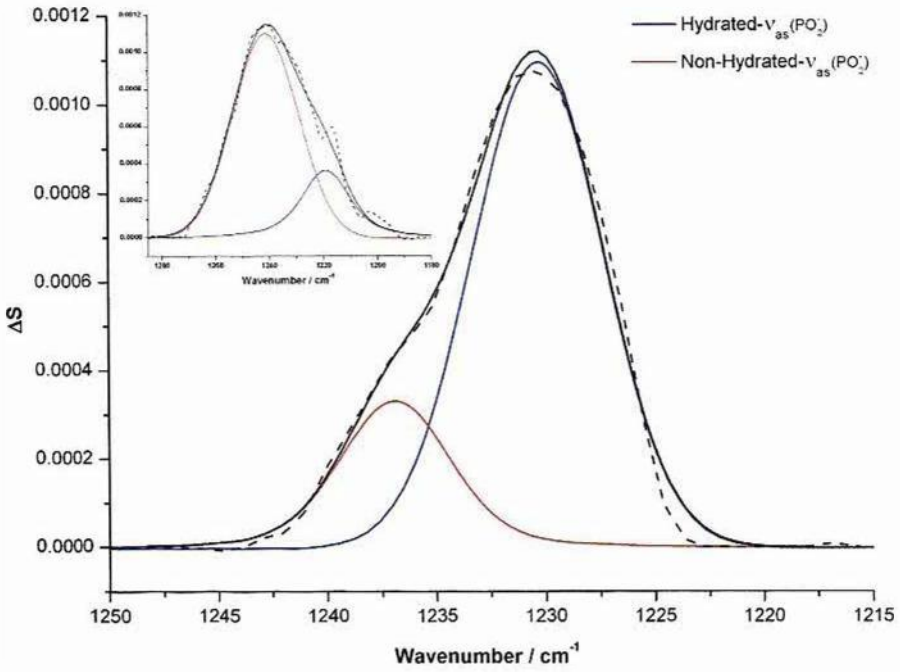

Figure 6.14: Deconvoluted asymmetric PO_2^- stretching band for a DMPS bilayer on a Au(111) electrode in 0.1 M NaF/H_2O solution at E=0.4 V. Inserted: Deconvoluted simulated spectra of DMPS bilayer supported in Au in $CDCl_3$ with 10% CD_3OD solution.

The background of spectra recorded at this settings were processed in the spectral region between 1130 and 1070 cm^{-1} to study the $\nu_s(PO_2^-)$. Figure 6.15 shows the spectra at different potentials. The dependence of this band with the applied potential is not very strong, the position remains constant and just slight changes in the intensity and bandwidth are observed.

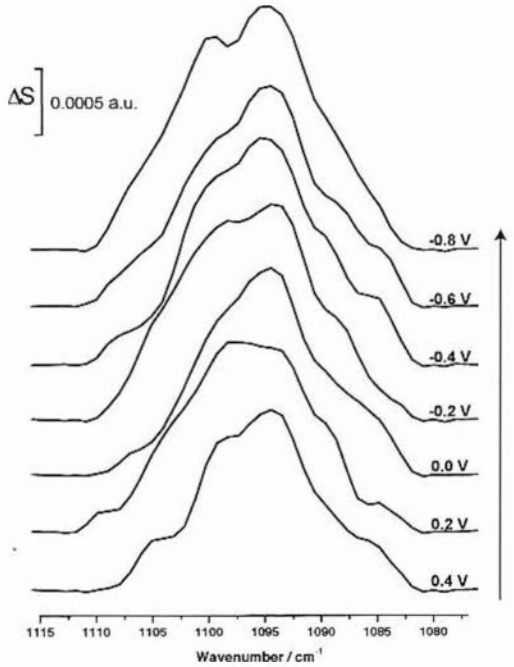

Figure 6.14: *In situ* PM-IRRA spectra for the PO_2^- symmetric stretching band region of a DMPS bilayer on a Au(111) electrode in 0.1 M NaF/H_2O solution at the indicated potentials.

The observed band is deconvoluted for a deeper analysis. The deconvolution shows the overlapping of three bands similar to DMPC vesicles [14]. The absorption band is formed by the symmetric phosphate group stretch $\nu_s(PO_2^-)$ at ≈1094 cm^{-1} and two asymmetric ν_s(C-O[P]) stretching bands at ≈1100 and ≈1088 cm^{-1} as Figure 6.15 shows.

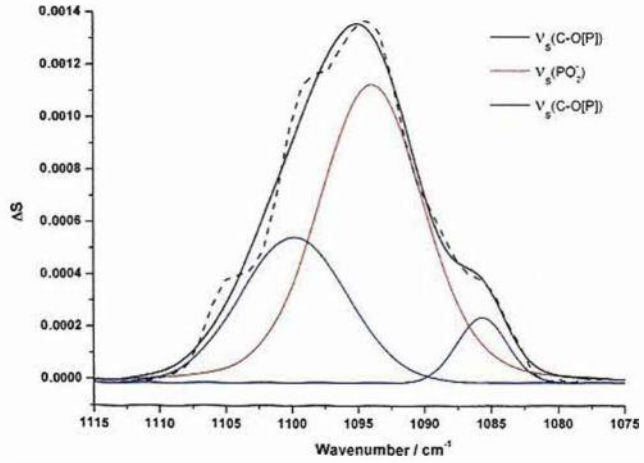

Figure 6.15: Deconvoluted symmetric PO_2^- stretching band for a DMPS bilayer on a Au(111) electrode in 0.1 M NaF/H_2O solution at E=0.4 V.

For the bands: $\nu_s(PO_2^-)$ and higher-frequency component ν_s(C-O[P]), the position does not change with potential. However the lower-frequency component ν_s(C-O[P]) changes from 1085 to 1088 cm^{-1} at positive potentials, indicating a possible small increase in the hydration towards negative potentials.

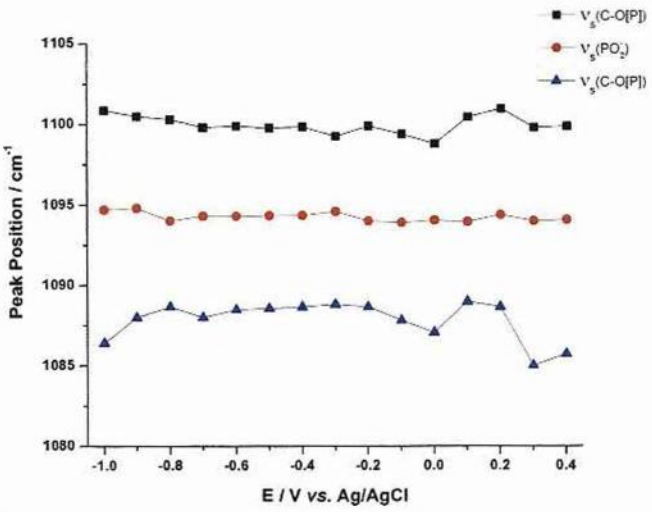

Figure 6.16: Plot of the overlapping bands at peak *vs.* potential for *in situ* PM-IRRAS of a DMPS bilayer in H_2O.

The intensity of the $\nu_s(PO_2^-)$ is not altered by the electric field applied but the FWHM decreases from 0.4 V < E < 0.1 V; at higher potentials the tendency shows an almost constant bandwidth of ≈7 cm^{-1}.

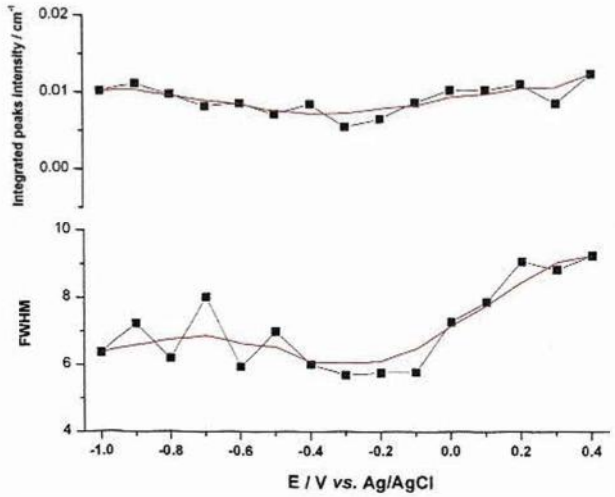

Figure 6.17: Plot of the integrated intensity and the FWHM of the $\nu_s(PO_2^-)$ peak *vs.* potential for *in situ* PM-IRRAS of a DMPS bilayer in H_2O.

In conclusion, we could say in agreement with Meijer *et al.* that, DMPS headgroups are tilted towards the solution (at least the headgroups in the outlet layer). This configuration allows the counter ions to penetrate and hydrate the phosphate groups constantly, in agreement with PO_2^- bands and the higher capacitance observed in DC experiments. The headgroups are somehow insensitive to the ionic strength which is observed in the high value of the differential potential zero charge ($E_N \approx$ -285 mV)[15].

Towards negative potentials, the molecules start tilting the acyl chains. This movement produces the bilayer to swallow solvent, which penetrates the bilayer reaching the carbonyl groups and increasing their hydration (C=O bands).

References:

1. G. Socrates, *Infrared and Raman Characteristic Group Frequencies*, John Wiley & Sons, Chichester, 2004.
2. A. Blume, W. Huebner and G. Messner, *Biochemistry*, 1988, **27**, 8239-8249.
3. R. N. A. H. Lewis and R. N. McElhaney, *Biophys. J.*, 1992, **61**, 63-77.
4. I. R. Miller and E. Wachtel, *Bioelectrochem. Bioenerg.*, 1998, **45**, 203-214.
5. R. G. Snyder, *J. Chem. Phys.*, 1967, **47**, 1316-1360.
6. U. P. Fringeli, *Z. Naturforsch C*, 1977, **32**, 20-45.
7. R. N. A. H. Lewis and R. N. McElhaney, *Chem. Phys. Lipids*, 1998, **96**, 9-21.
8. H. L. Casal and H. H. Mantsch, *Biochim. Biophys. Acta, Rev. Biomembr.*, 1984, **779**, 381-401.
9. H. H. Mantsch and R. N. McElhaney, *Chem. Phys. Lipids*, 1991, **57**, 213-226.
10. M. L. Mitchell and R. A. Dluhy, *J. Am. Chem. Soc.*, 1988, **110**, 712-718.
11. I. Zawisza, X. M. Bin and J. Lipkowski, *Langmuir*, 2007, **23**, 5180-5194.
12. W. Hubner and A. Blume, *Chem. Phys. Lipids*, 1998, **96**, 99-123.
13. J. Clavilier, R. Faure, G. Guinet and R. Durand, *J. Electroanal. Chem.*, 1980, **107**, 205-209.
14. X. Bin, S. L. Horswell and J. Lipkowski, *Biophys. J.*, 2005, **89**, 592-604.
15. L. A. Meijer, F. A. M. Leermakers and J. Lyklema, *Recueil des Travaux Chimiques des Pays-Bas*, 1994, **113**, 167-175.

CHAPTER 7: *IN SITU* PM-IRRRAS OF DMPE BILAYER

7.1 Introduction

The last chapter in this thesis is based on a complete *in situ* PM-IRRAS study of the DMPE bilayer to observe differences regarding the bilayer packing and hydration in comparison with DMPS bilayers.

The study is divided into two parts: the fist part provides details on the average properties of the DMPE bilayer and gives information concerning the tail packing [ν(C-H) stretching vibration bands] and the hydrogen-bonding [ν(C=O) and $\nu_{as}(PO_2^-)$]. The second part describes the effect of the asymmetric environment on the structure of each leaflet of the DMPE bilayer. Bilayers containing deuterated DMPE molecules at specific positions, such as the methylene groups, allow the selective calculation of the orientation of the acyl chains in the leaflet where normal DMPE ($DMPE_H$) is used. The basis of this selectivity is the difference in vibrational frequency between the C-H stretching modes (≈3000 cm^{-1}) and C-D stretching modes (≈2200 cm^{-1}).

7.2 Acyl Chain Region. Acyl C-H Stretching Modes

The majority of the CH_2 groups are located in the acyl chains of the DMPE molecules. In order to determine the conformation, physical state and the tilt angle of the acyl chains within the DMPE bilayer, the IR absorption of the C-H stretching mode is investigated.

The DMPE bilayer was deposited onto Au(111) and inserted in the spectroelectrochemical cell. A calculated angle of θ = 51.4°, a gap thickness of d = 1.9 μm and the PEM set at 2900 cm^{-1} were the settings used for the *in situ* PM-IRRAS experiment (the fitted reflectivity is provided in Figure 7.1). As previously with DMPS bilayers, the spectra were recorded with an initial potential of E_i = 0.4 V *vs.* Ag/AgCl, which was then stepped in the cathodic direction by 0.1 V increments, reaching the final applied potential at E_f = -1 V. Figure 7.2 shows a few (due to invariability of the peaks) of the corrected spectra obtained at different potentials. From the C-H stretching vibrations, four peaks are seen: at higher wavenumbers $\nu_{as}(CH_3)$ is centred at ≈2961 cm^{-1}, followed by the $\nu_{as}(CH_2)$ band at ≈2918 cm^{-1}, which has a secondary peak and a pronounced shoulder due the overlapping with

the Fermi resonance bands at ≈2930 and 2901 cm^{-1}. At ≈2874 and ≈2852 cm^{-1} are centred the $\nu_s(CH_3)$ and the $\nu_s(CH_2)$ stretching bands, respectively.

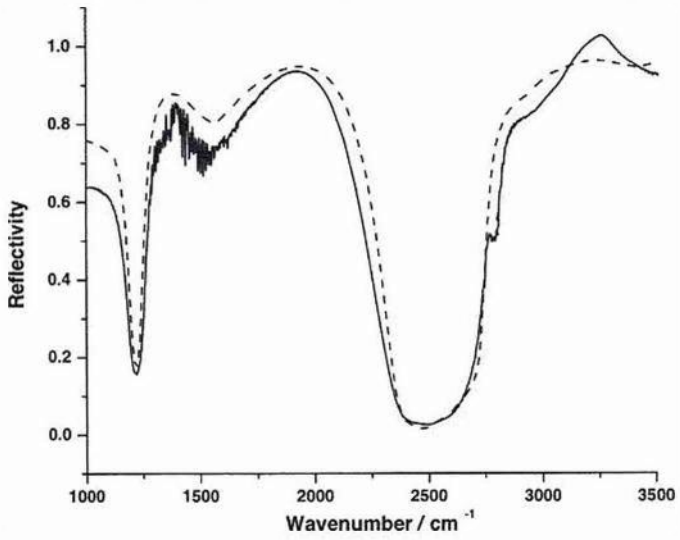

Figure 7.1: Reflectivity spectra for a thin layer cavity spectroelectrochemical cell (BaF_2/D_2O/Au). The experimental spectrum is represented by a solid line and the dashed line represents the calculated spectrum (θ = 51.4° and d = 1.9 μm).

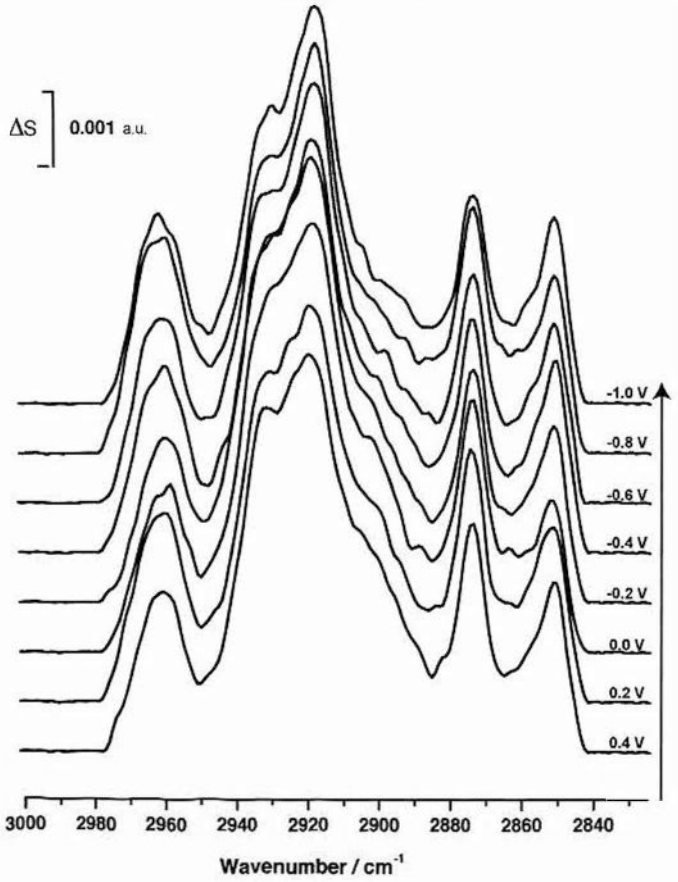

Figure 7.2: *In situ* PM-IRRA spectra for C-H stretching region of a DMPE bilayer on a Au(111) electrode in a 0.1 M NaF/D_2O solution at the indicated potentials.

The exact characteristics of the bands were obtained after the deconvolution of the spectra using the Voigt function. Figure 7.3 shows that the positions of the bands are < 2918 cm^{-1} for $\nu_{as}(CH_2)$ and around 2852.5 cm^{-1} for $\nu_s(CH_2)$, indicating that, the DMPE film has stretched acyl chains with a very few *gauche* conformations in the whole range of potentials. These values are very similar to those mentioned for *ex situ* DMPE bilayers, suggesting that there is only a slight effect of electric field on the acyl chain conformation.

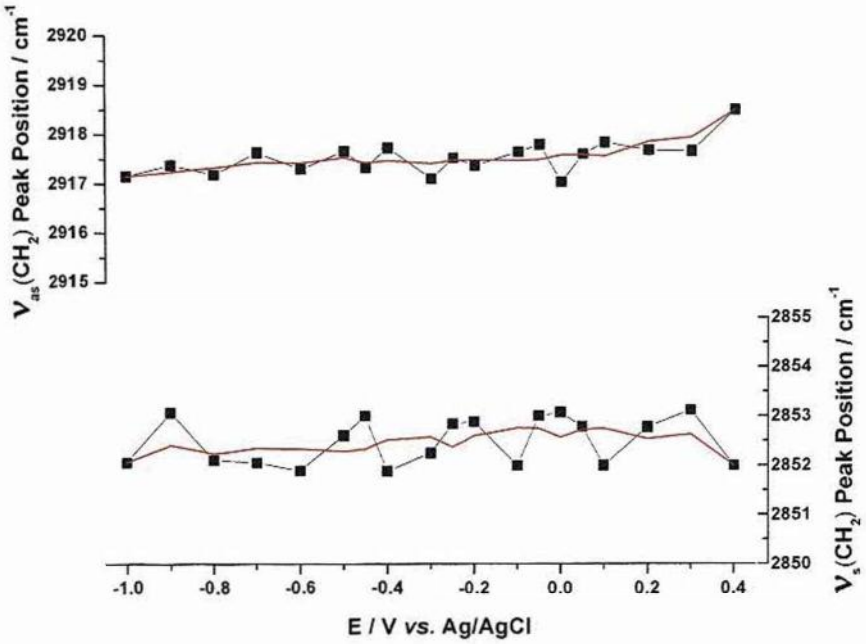

Figure 7.3: Plot of the position of $\nu_{as}(CH_2)$ and $\nu_s(CH_2)$ stretching bands *vs.* potential for *in situ* PM-IRRAS of DMPE bilayer in D_2O.

The width of the $\nu_{as}(CH_2)$ bands are plotted as a function of applied potential in Figure 7.4. This graph compares the FWHM from *in situ* PM-IRRAS of DMPS with DMPE bilayers. Towards negative potentials, there is a similar decreasing tendency indicating a very low movement of the bilayer when it detaches from the gold surface. The FWHM of the $\nu_{as}(CH_2)$ band for a DMPE bilayer is narrower than that for a DMPS bilayer, suggesting that DMPE forms a more compact bilayer. This could happen if a more dense hydrogen bonding network between the phosphate and the NH_3^+ units of neighbouring PE molecules is formed.

The potential of zero charge for DMPE bilayers was calculated to be

$E_{pzc} \approx +0.12$ V which means that, at negative potentials the electric fields are strongest than at positive potentials, these strong fields could rearrange the DMPE headgroups, aligning the P^--N^+ dipole with the field, lowering the bilayer mobility.

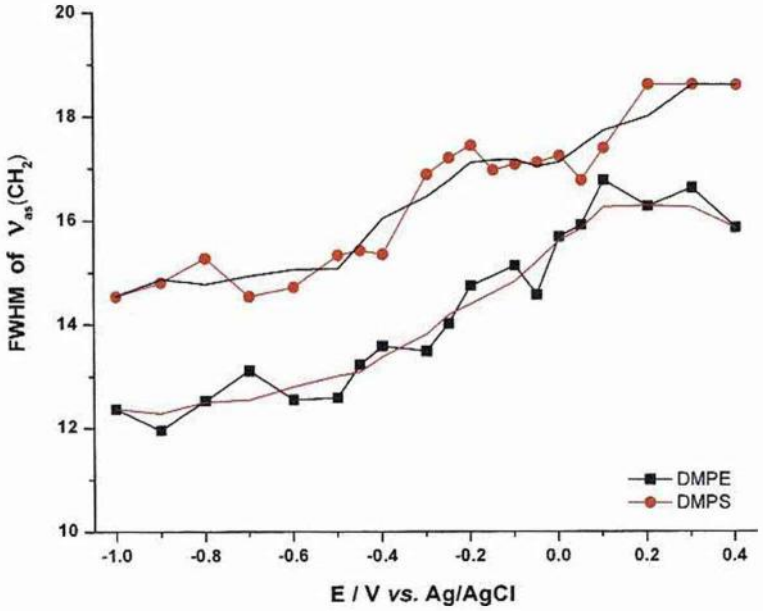

Figure 7.4:Comparison of the FWHM of $\nu_{as}(CH_2)$ and $\nu_s(CH_2)$ stretching bands *vs.* potential for *in situ* PM-IRRAS of DMPS and DMPE bilayers in D_2O

The tilt angle of the molecules in a DMPE bilayer is calculated following the procedure that was explained in Chapter 3. The angles between the surface normal and the transition dipoles of $\nu_{as}(CH_2)$ and $\nu_s(CH_2)$ modes were calculated. This calculation was carried out using the experimental integrated band intensity from the corrected spectra and the calculated integrated band intensity from the simulated spectra determined (from the optical constants) for a bilayer of randomly oriented DMPE molecules (given in Figure 7.5). For a fully stretched all *trans* conformation of the acyl chain, $\theta_{as}(CH_2)$, $\theta_s(CH_2)$ and the chain tilt angle (θ_{Chain}) are related by Eq. 3.26, thus the tilt angle of the chain can be calculated.

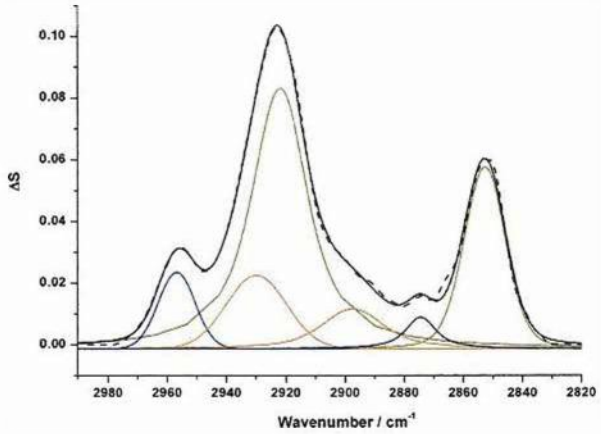

Figure 7.5: Simulated spectra of randomly distributed DMPE molecules of film thickness 7.4 nm on a Au substrate in D_2O (θ = 51.4° and d = 1.9 μm).

The values of the calculated angles are shown in Figure 7.6. These values show an average angle of ≈8° at E> -0.4 V which slightly decreases to ≈7° at E< -0.4 V. The changes are very small and lie within expected experimental error (the estimated error in the determination of θ is ±3° due to the uncertainly of the background correction and band deconvolution procedures [1]) but there is a small trend towards slightly lower tilt angle at negative potentials.

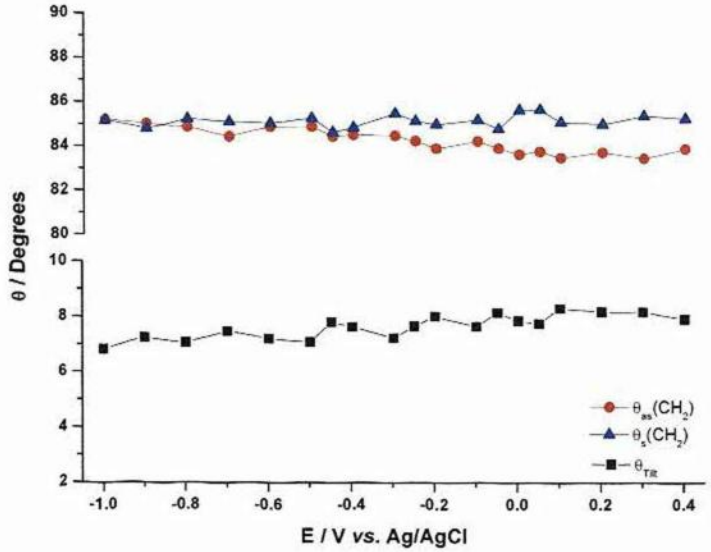

Figure 7.6: Potential dependence of the angle (θ) between the direction of the transition dipole moment and the surface normal for the acyl chain of a DMPE film at the Au(111) surface, $\nu_{as}(CH_2)$ and $\nu_s(CH_2)$ and of the angle between the chain and the surface normal.

These results agree with the observations obtained from π-*A* isotherms, electrochemical measurements (DC) and *ex situ* PM-IRRAS. The area per molecule from the π-*A* isotherm verified small headgroups that pack very tightly, lowering the film capacitance and reducing molecular mobility. The strong headgroup-headgroup and tail-tail interactions mean that the disruption of the DMPE bilayer structure by the electric field is not strong enough for the water to penetrate to a large extent and raise capacitance. Only at negative potentials some slight rearrangements in the head groups may make the acyl chains tilt slightly and increase the strength of the hydrogen bonding. The band positions and FWHM of the $\nu_s(CH_2)$ from DMPE bilayers are very similar to the frequencies and bandwidth of DMPC bilayers in the desorption state at E< -0.5 V (2854 ± 0.3 cm^{-1} / 11.5 ± 0.5 cm^{-1} for a bilayer formed by the LBLS method and 2851.6 ± 0.2 cm^{-1} / 9.0 ± 0.3 cm^{-1} for vesicles [1]) suggesting that the acyl chains pack similarly than DMPC bilayers but since the DMPE headgroups are smaller, it may not need to do the tilting in the same way [2].

7.3 Interfacial Region. Carbonyl Stretching Vibrations.

The ν(C=O) stretching vibration band occurs in the spectral range between 1750 and 1715 cm^{-1}. This band was investigated because of its sensitivity to the degree of hydration of the glycerol moiety.

The optimum conditions used for this experiment were given by the agreement between the experimental and the calculated reflectivity corresponding to an angle of θ = 61.5° and d =10 μm at a wavenumber of 1600 cm^{-1}. The spectra were recorded in the cathodic direction as mentioned for past *in situ* experiments. The corrected and background subtracted spectra are shown in Figure 7.7.

Changes in the overall intensity of the band are not easily apparent; only at E= -0.45 V the intensity of the band starts to increase until it reaches its maximum at E= -0.5 V where the band becomes also broader. After this maximum, the intensity and width decrease, equalling similar values to those at positive potentials. A marked asymmetry in the contours of the C=O stretching band is observed. This asymmetry is due to the overlap of four bands that can be analysed by deconvolution using the Voigt function.

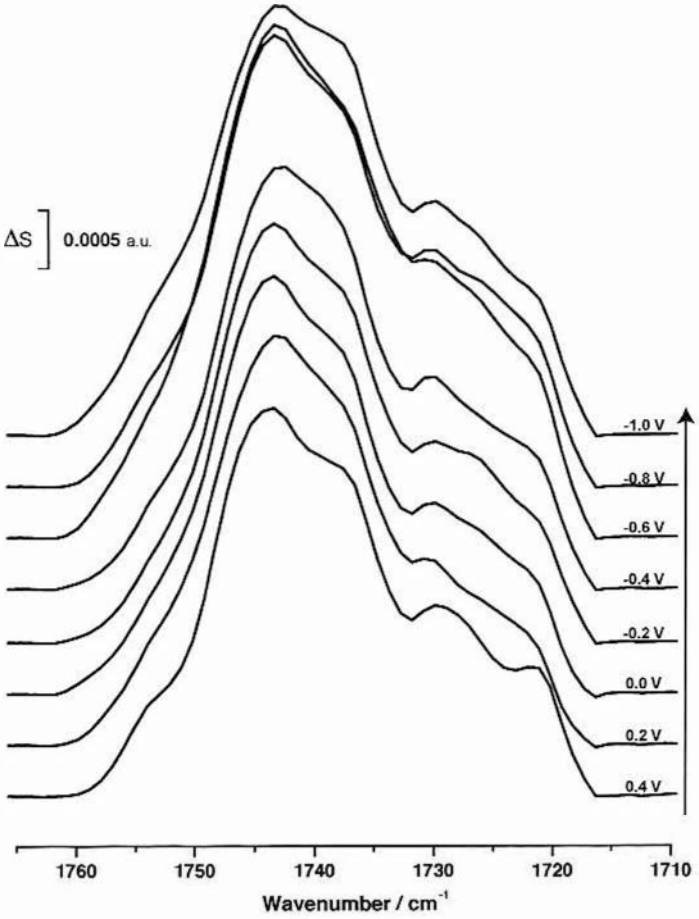

Figure 7.7: *In situ* PM-IRRA spectra for the C=O stretching region of a DMPE bilayer on a Au(111) electrode in a 0.1 M NaF/D_2O solution at the indicated potentials.

An example of a deconvoluted spectrum is shown in Figure 7.8. The higher-wavenumber peak at ≈1740 cm^{-1} is due to the non-hydrogen bonded carbonyl group (this band is hereafter referred to as "Dry band") and is a superposition of two underlying bands that show the non-equivalence between the two ester carbonyls groups (Dry_{sn-1} and Dry_{sn-2}). The lower-wavenumber peak centred at ≈1725 cm^{-1} is sensitive to the hydrogen bonding to the carbonyl groups ("Hydrated band") and is formed as well by two underlying bands (Hydrated $_{sn-1}$ and Hydrated $_{sn-2}$).

The intensities of these bands are plotted in Figure 7.9. As we estimated previously, the bands have constant intensities, 0.06±0.003 cm^{-1} for the dry band and 0.02±0.002 cm^{-1} for a hydrated band at E< -0.4 V. Between the range -0.7 V < E < -0.4 V there is a maximum in the intensity which decreases down to values slightly higher than the initial one for the dry band (0.06±0.002 cm^{-1}) and similar for the hydrated band (0.02±0.003 cm^{-1}). These intensity changes do not

suggest to indicate hydration in the carbonyl groups. An increase in the hydration should be seen as a change in the hydrated band in respect to the dry band. C=O bands for DMPE bilayers have a similar trend, thus the electric field does not appear to have any influence in film swelling properties onto the interfacial region.

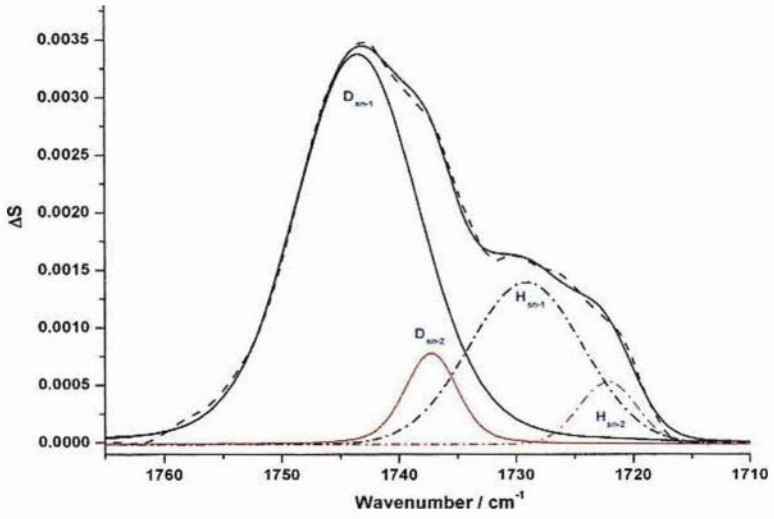

Figure 7.8: Deconvoluted spectrum of the ν(C=O) stretching band of a DMPE bilayer on a Au(111) electrode in a 0.1 M NaF/D_2O solution at E = 0.1 V with band assignment.

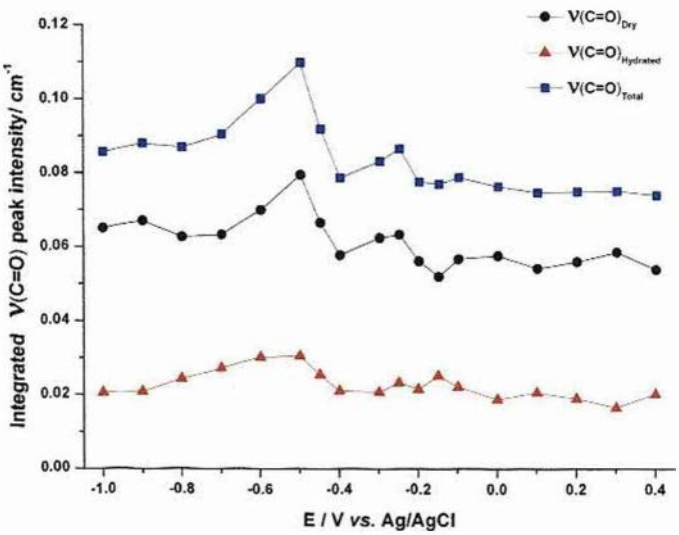

Figure 7.9: Plot of the integrated $\nu(C=O)_{Total}$, $\nu(C=O_{Dry})$ and $\nu(C=O_{hydrated})$ peaks intensity *vs.* potential for *in situ* PM-IRRAS of DMPE bilayer in D_2O.

The positions of the bands (Figure 7.10) seem invariant with the applied electric field indicating that there is no increase in the bilayer disorder due desorption. The FWHM of the bands (plotted *vs.* potential in Figure 7.11) shows for the *sn1*-ester carbonyl group a small increase in the bandwidth and intensity at ≈E=-0.5 V, a similar potential to that at which electrochemical experiments showed a phase transition. This increase can be indicative of the mobility of this carbonyl group. The average position and FWHM of the bands are given in Table 7.1.

Table 7.1: Average position and FWHM of deconvoluted PM-IRRAS of the ν(C=O) stretching band of a DMPE bilayer on a Au(111) electrode in a 0.1 M NaF/D_2O solution

	Dry_{sn1}	Dry_{sn2}	$Hydrated_{sn1}$	$Hydrated_{sn2}$
ν(C=O) / cm^{-1}	1743.6±0.1	1737.3±0.2	1729.1±0.3	1721.8±0.4
FWHM / cm^{-1}	12.9	5.7	10.9	5.2

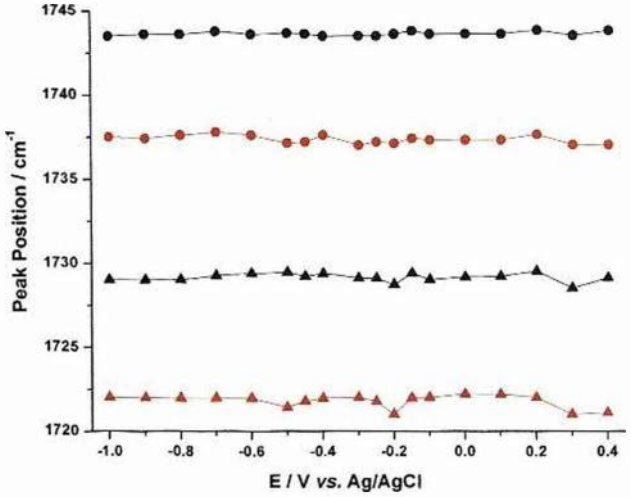

Figure 7.10: Plot of the position of the deconvoluted ν(C=O) vibration bands *vs.* potential for *in situ* PM-IRRAS of DMPE bilayer in D_2O. From top to bottom: Dry_{sn1}, Dry_{sn2}, $Hydrated_{sn1}$ and $Hydrated_{sn2}$.

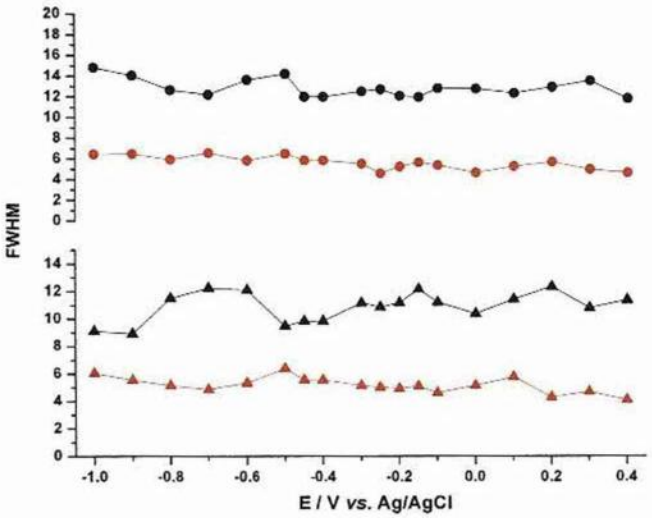

Figure 7.11: Plot of the FWHM of ν(C=0) stretching bands *vs.* potential for an *in situ* PM-IRRAS of DMPE bilayer in D_2O. From top to bottom: Dry_{sn1}, Dry_{sn2}, $Hydrated_{sn1}$ and $Hydrated_{sn2}$.

7.4 Polar Group Region. Phosphate Group Vibrations

The study of the $\nu_{as}(PO_2^-)$ stretching band has been useful in monitoring the hydration state of the polar headgroup. The fact that the phosphate groups bind water molecules more easily than the carbonyl groups makes the study of DMPE bilayers in this region an important area of study.

The optimum conditions used were θ=55° and d = 3.4 μm with the PEM set up at 1100 cm^{-1} and the spectroelectrochemical cell was filled with 0.1 M NaF in H_2O. The spectra were recorded in the cathodic direction and processed as previously. The position of the $\nu_{as}(PO_2^-)$ band is centred at ≈1231 cm^{-1} with a FWHM of ≈7 cm^{-1} and intensity of ≈0.007. The band position, width and intensity are constant during the whole potential range, which is consistent with strong hydrogen bonding with neighbouring amine groups or with water. These results are in agreement with the literature where has been reported no changes in the position of the band due no changes in the frequencies from anhydrous or hydrated DMPE [3, 4]. Some small changes towards negative potentials cannot be considered significant to predict changes in the bilayer.

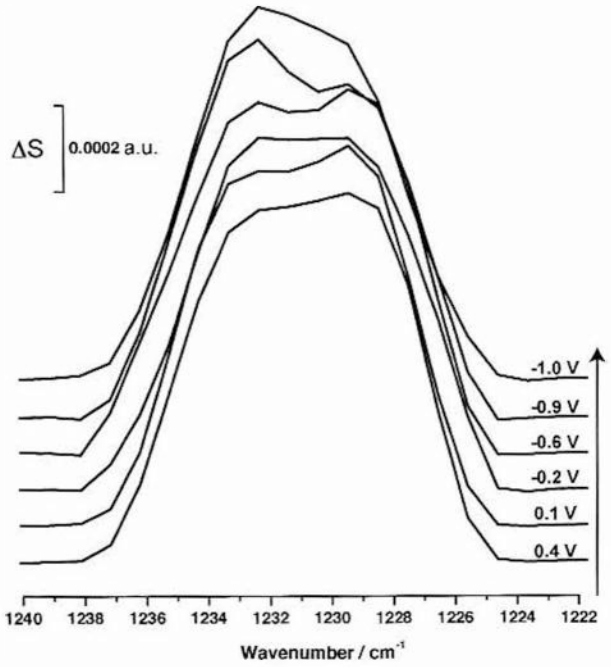

Figure 7.12: *In situ* PM-IRRA spectra for the PO_2^- asymmetric stretching band region of a DMPE bilayer on a Au(111) electrode in 0.1 M NaF/H_2O solution at the indicated potentials.

The simulated spectrum of the DMPE bilayer in H2O allows the calculation of the angle from the asymmetric transition dipole of the $\nu_{as}(PO_2^-)$ band and the surface normal. The results are plotted in Figure 7.13. The graph shows an average angle of 67 °± 0.4. A similar angle has been obtained for DMPC bilayer transferred by the LBLS method and vesicles [1].

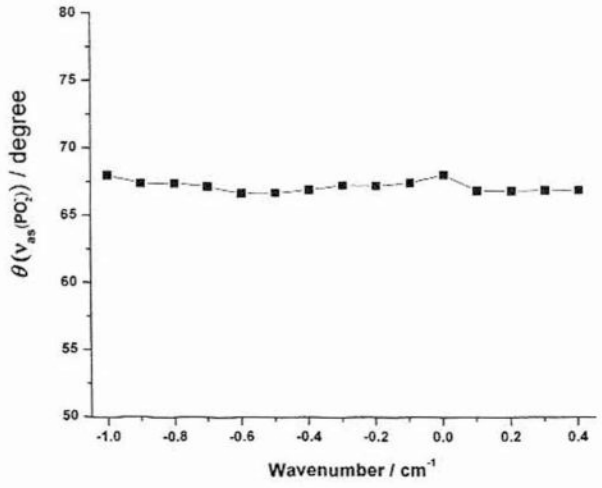

Figure 7.13: Dependence of the angle (θ) between the direction of the transition dipole moment and the surface normal with potential for $\nu_{as}(PO_2^-)$ band.

In summary, these findings can be interpreted in terms of a tight hydrogen bond network between the phosphate and the ammonium group of the DMPE molecules that does not allow the water to penetrate the bilayer or, if so, there is no effect from the water on the corresponding chemical groups because hydrogen bonding with neighbouring molecules and with water will have a similar influence on the band positions. Electrochemical measurements showed a very low capacitance when the bilayer was adsorbed on the electrode, indicating a low permittivity of the bilayer, the capacitance increased as the bilayer detached from the electrode. In this state it is consistent with the possibility that the P-N interaction still remains in fully hydrated PE which is more probable when the bilayer is detached, hindering the hydration as was suggested by Bouchet *et al.* It can be suggested that beyond the first water of adsorption, no more water can be intercalated.

7.5 PM-IRRAS of DMPE Bilayers Containing Deuterated DMPE

The C-H stretching region was studied with bilayers containing in one of the leaflets $DMPE_{D54}$ in order to determine the angle of the tilt angle and orientation of the leaflet containing $DMPE_H$. $DMPE_{D54}$ is selectively deuterated and has all the hydrogen atoms of the acyl chain replaced with deuterium, thus just the C-H vibrations from the leaflet containing $DMPE_H$ are analysed in order to calculate the orientation of that leaflet.

Figure 7.14 shows the spectra for each case, where the $DMPE_H$ leaflet is adjacent to the electrode (Au_PE_H-PE_D) and adjacent to the electrolyte (Au_PE_D-PE_H). The figures show that the methylene stretching bands are dependent on the potential. In the bilayer formed by Au_PE_D-PE_H, the intensities of the bands are more intense than for the Au_PE_H-PE_D. For both bilayers an intensity increase is seen in the $\nu_{as}(CH_2)$ band between -0.6 V< E < 0.0 V in which its maximum is reached at E≈ -0.4 V. Figure 7.15 shows a 3D plot of the Au_PE_D-PE_H bilayer where this change can be observed.

The deconvolution of the bands indicates slight differences in band position (Figure 7.16), the intensity and the FWHM between these two leaflets. The frequencies (>2920 cm^{-1} and ≈2851 cm^{-1} for $\nu_{as}(CH_2)$ and $\nu_s(CH_2)$ respectively) and widths (Figure 7.16) are characteristic of a phase state of the bilayer in which the

majority of the acyl chains are all *trans* although a few chains contain some *gauche* conformers. The bandwidths for $\nu_s(CH_2)$ are $\approx$10 cm^{-1}, this are very similar between the two bilayers in the range of $-0.2V < E < 0.4$ V for both bilayers. At potentials lower than -0.2 V, the bandwidth of the bilayer Au_PE_D-PE_H increases, indicating higher mobility of the external bilayer.

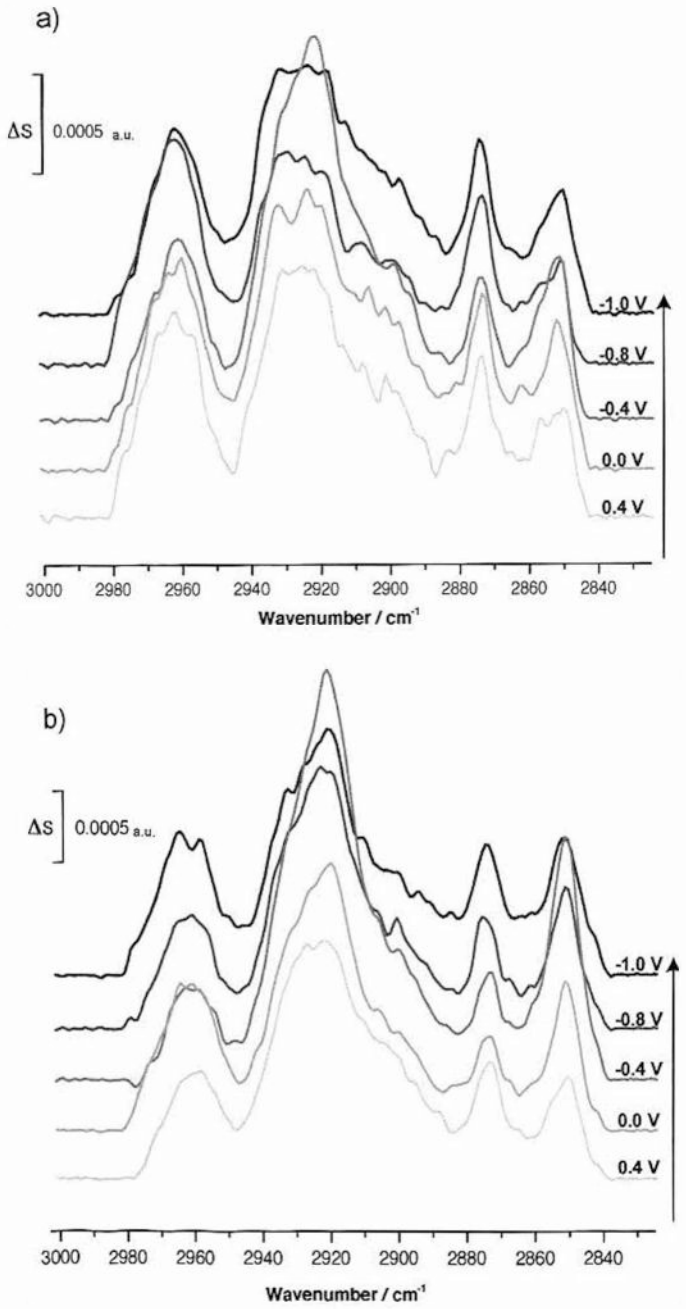

Figure 7.14: PM-IRRA spectra for the C-H stretching region for a DMPE bilayer on a Au(111) electrode; a) Bilayer with the $DMPE_H$ leaflet adjacent to the electrode (θ =51° and d = 2 μm) and b) adjacent to the electrolyte (θ =51° and d = 1.25 μm).

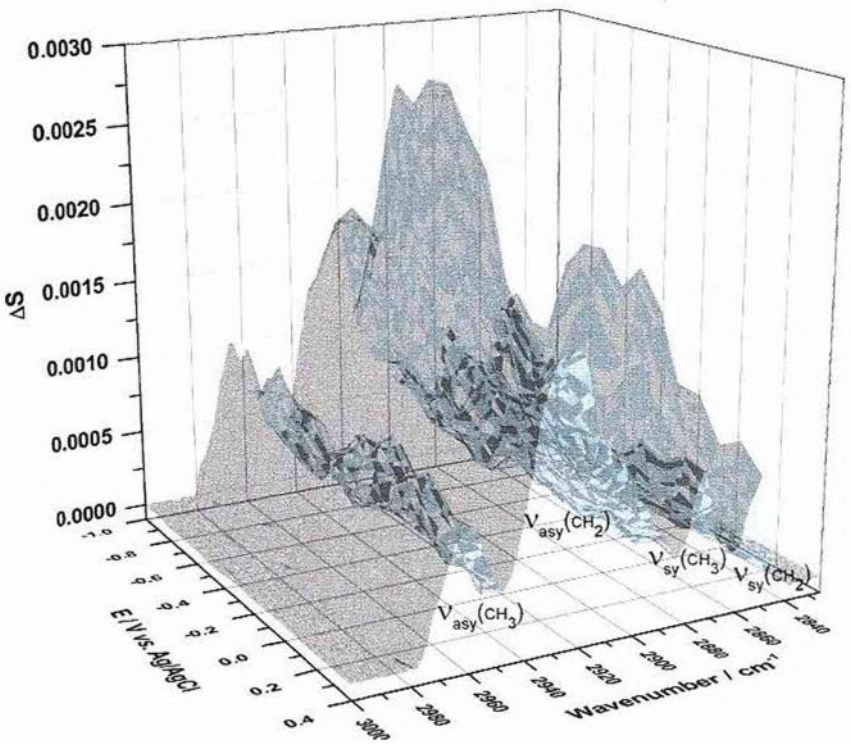

Figure 7.15: 3D Graph of the *in situ* PM-IRRAS for the C-H stretching region for a Au_PE_D-PE_H bilayer on a Au(111) electrode *vs.* potential and wavenumber.

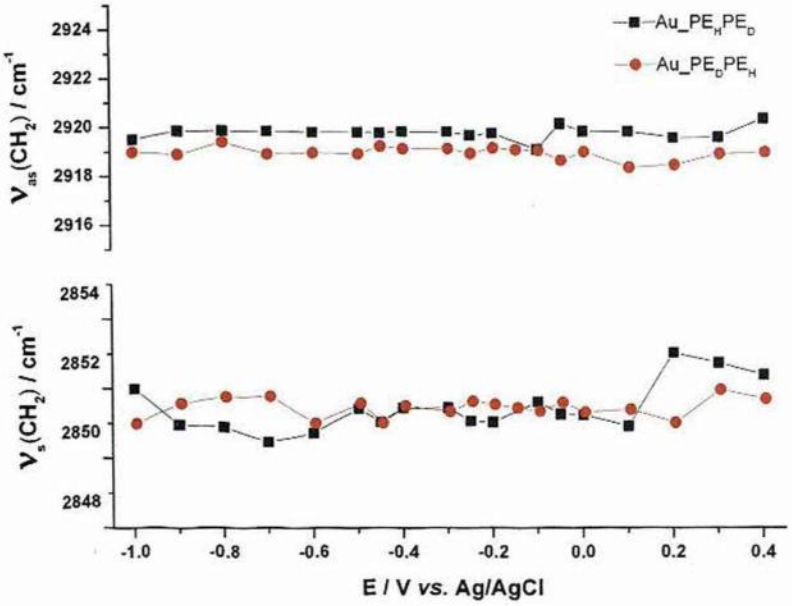

Figure 7.16: Plot of the position of $\nu_{as}(CH_2)$ and $\nu_s(CH_2)$ stretching bands *vs.* potential for *in situ* PM-IRRAS of Au_PE_H-PE_D and Au_PE_D-PE_H bilayers in D_2O.

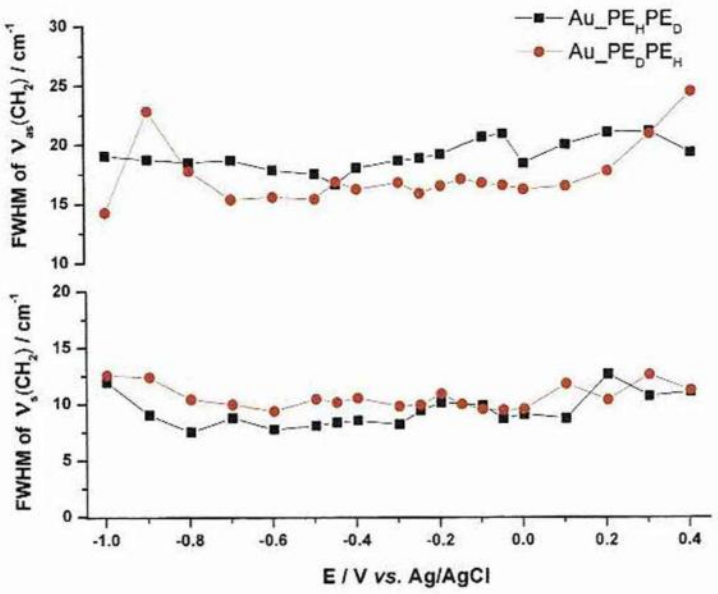

Figure 7.17: Plot of the FWHM of $\nu_{as}(CH_2)$ and $\nu_s(CH_2)$ stretching bands *vs.* potential for *in situ* PM-IRRAS of Au_PE_H-PE_D and Au_PE_D-PE_H bilayers in D_2O.

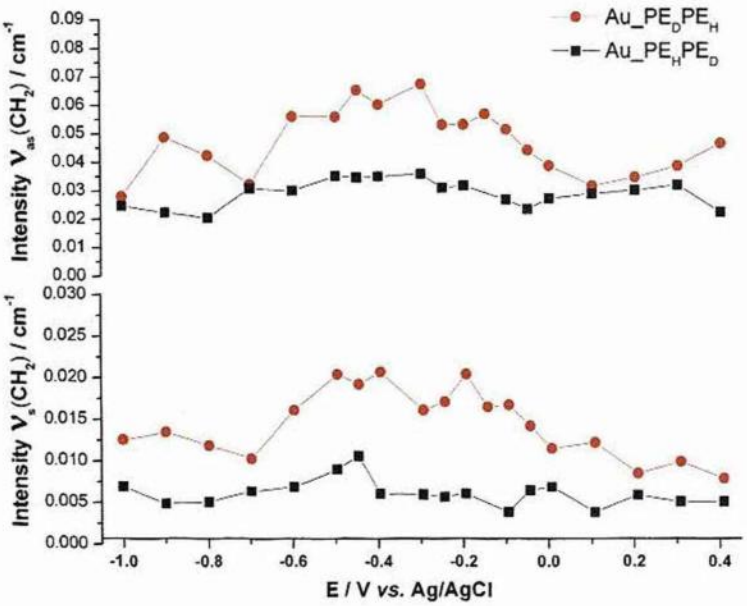

Figure 7.18: Plot of integrated peak intensity for $\nu_{as}(CH_2)$ and $\nu_s(CH_2)$ stretching bands *vs.* potential for *in situ* PM-IRRAS of Au_PE_H-PE_D and Au_PE_D-PE_H bilayers in D_2O.

The tilt angle of the molecules from each leaflet within the DMPE bilayer was calculated as previously. The angles $\theta_{as}(CH_2)$, $\theta_s(CH_2)$ were calculated for each of the two bilayers (Au_PE_H-PE_D and Au_PE_D-PE_H). This calculation was carried out using the experimental integrated band intensities from the corrected spectra and the calculated integrated band intensities from the simulated spectra determined in these systems for a monolayer (2.7 nm thickness) of randomly oriented DMPE molecules. The acyl chains are considered to be in an all *trans* conformation, thus a precise calculation of the chain tilt angle (θ_{Chain}) can be achieved by the use of Eq. 3.26. Figure 7.19 shows the respective angles as a function of applied potential for Au_PE_H-PE_D and Au_PE_D-PE_H bilayers.

At E> -0.4, the bilayer is adsorbed on the electrode surface. Within these potentials, two tendencies can be observed At E> -0.4, the average value of the tilt angle amounts to ≈6.8° in the bottom layer (adjacent to the electrode surface) and ≈9.5° in the top layer (adjacent to the electrolyte); the tilt angle differs by about ≈3° between both leaflets. The difference becomes higher between -0.4 V < E < 0.0 V, where the maximum difference in the angle is ≈5°. At E< -0.4 V where the bilayer is desorbed, the average tilt angle difference can be considered back to ≈3°.

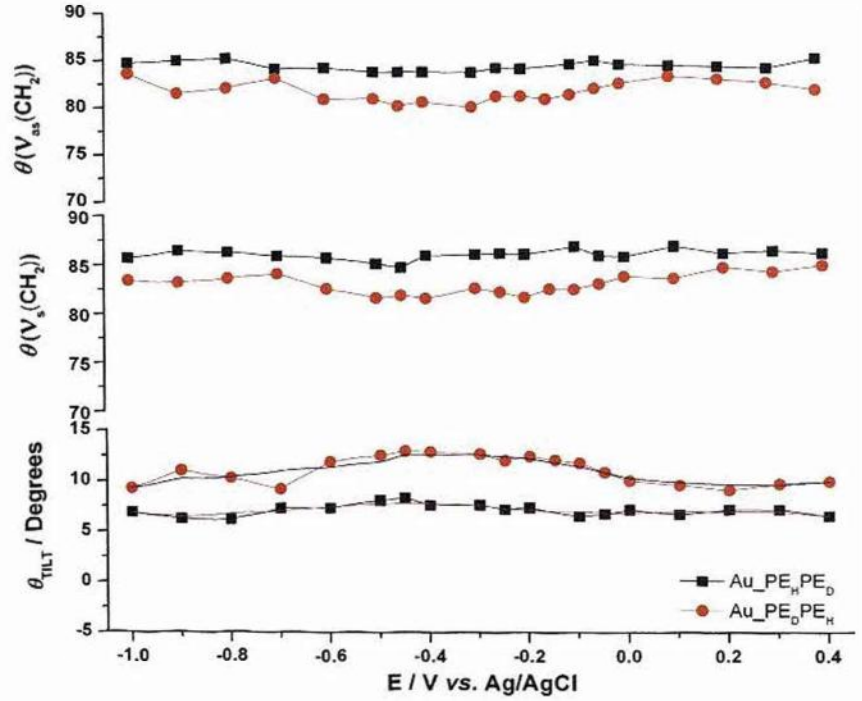

Figure 7.19: Plots of the angles between the direction of the surface normal and the transition dipole moment of the $\nu_{as}(CH_2)$ (top), $\nu_s(CH_2)$ (middle) and the acyl chains (bottom).

This study shows that asymmetry in the environment does not have a major impact on the orientation of the DMPE bilayers. The bilayer is exposed to an asymmetric environment when it is adsorbed, where one leaflet is in contact with the gold and the other leaflet is with the solution. In this region, a ≈3° difference in tilt angle was calculated, which is quite similar to the difference between the tilt angles when the bilayer is detached. If is assumed for DMPE bilayers the same that has been reported for DMPC bilayers (that when the film is detached from the surface it remains in close proximity to the electrode and is suspended on a thin cushion of the electrolyte [5]), the two leaflets will be in contact with the water at these potentials and the bilayer will be in a more symmetric environment, which means that the angle difference is almost the same in the symmetric and asymmetric environment.

The two phase transitions observed in electrochemical experiments (E≈ -0.5 V and E≈ -0.0 V) marked the region where the tilt angle difference is higher, 5° indicating a change within the bilayer that is more intense in the bilayer exposed to the solution. This change could be ascribed to a higher mobility of the top layer or to a difference in solvation between the layers – the top layer is more accessible to possible solvent ingress at higher fields.

References:

1. I. Zawisza, X. M. Bin and J. Lipkowski, *Langmuir*, 2007, **23**, 5180-5194.

2. I. Zawisza, X. Bin and J. Lipkowski, *Bioelectrochem.*, 2004, **63**, 137-147.

3. A. M. Bouchet, M. A. FrÌas, F. Lairion, F. Martini, H. Almaleck, G. Gordillo and E. A. Disalvo, *Biochim. Biophys. Acta, Biomembr.*, 2009, **1788**, 918-925.

4. W. Pohle, C. Selle, H. Fritzsche and M. Bohl, *J. Mol. Struct.*, 1997, **408-409**, 273-277.

5. I. Burgess, M. Li, S. L. Horswell, G. Szymanski, J. Lipkowski, J. Majewski and S. Satija, *Biophys. J.*, 2004, **86**, 1763-1776.

CHAPTER 8: CONCLUSIONS AND FUTURE WORK

8.1 Conclusions

The objective of this work was to investigate the physicochemical properties of phospholipid bilayers formed at the gold electrode surface using PM-IRRAS as a tool to follow structural changes such as orientation and hydration. Phospholipid bilayers supported on electrodes are of widespread interest because their structural similarities to living cell membranes provide the right environment for the study of changes in the presence of electric field.

A combination of different techniques was used for the research presented in this thesis and PM-IRRAS proved to be an excellent tool for the acquisition of high quality spectra and quantitative information.

Phospholipid monolayers formed at the air/water interface were deposited onto gold substrates using the LBLS technique allowing us to form symmetric and asymmetric bilayers at a controlled surface pressure, achieving a well defined physical state in the molecules, which was described by *ex situ* PM-IRRAS experiments. *Ex situ* bilayers formed by DMPS and DMPE molecules (Figure 8.1) have shown well-ordered acyl chains containing a few *gauche* conformations where the tilt of the acyl chains was found to be equal to 8.3° for both bilayers. This agrees with the fact that these molecules have the similar small headgroup area (43 and 41 $Å^2$ for DMPE and DMPS) which allow the acyl chains to pack more upright than the larger DMPC molecules. Similar values for the position of $\nu_{as}(CH_2)$ and $\nu_s(CH_2)$ stretching bands when the bilayers were studied *in situ* to those for *ex situ* suggested that there was not an effect from the electric field on the acyl chain conformation and their *trans* conformation was maintained in a hydrated environment.

The interpretation of the electrochemical response in differential capacitance experiments showed as a generality that all the studied bilayers formed compact films on the electrode surface at $-0.4 < E < 0.4$ V. Within this range of potentials the chains of DMPS bilayers have shown an average tilt angle of ≈10.2° which increased up to ≈16° before the bilayer started to desorb, indicating that the acyl chains slightly tilt and their structure was conformationally restricted. An average tilt angle of ≈8° and the lowest capacitance was obtained for DMPE bilayers in this the same range

of potentials, indicating that water and/or electric field was not able to penetrate or disrupt its compact conformation (the tilt angle in *ex situ* PM-IRRAS is very similar to that of anhydrous DMPE).

Preliminary *ex situ* PM-IRRAS studies gave some information concerning differences in the hydration of the carbonyl group between these two molecules; somehow in anhydrous lipids the carbonyl groups from DMPS were more accessible to residual water than DMPE. *In situ* PM-IRRAS showed at E> -0.15 V that the ν(C=O) band split into 3 peaks for DMPS bilayers. As the potential decreased, the two lower-wavenumber bands increased and superimposed on each other to form one broader vibrational band which indicated a higher level of hydration in its carbonyl group before desorption. This increase in the hydration matched with more tilted acyl chains. A new arrangement within the film (maybe resulting from the negative charge on the electrode) forced the phosphate groups away making the carbonyl group more accessible to hydration and tilting the acyl chains. The study of the hydration of the headgroup was made by the analysis of $\nu_{as}(PO_2^-)$ and $\nu_s(PO_2^-)$ bands. These bands proved to be constantly hydrated with no more increase of water with the electric field, which explains the relatively high capacity of these bilayers.

The study of these bands for DMPE bilayers showed that ν(C=O) and $\nu_{as}(PO_2^-)$ bands seemed not to increase their hydration levels when the electric field was applied or during desorption, which was consistent with strong hydrogen bonding with neighboring amine groups. Some changes in the intensity were associated with small movements in the carbonyl groups.

The effect of the asymmetric environment to which the membrane is exposed was investigated using deuterated DMPE. The vibrations from the leaflet containing $DMPE_H$ were analysed in order to calculate the orientation of that leaflet. This series of investigations showed that asymmetry in the environment does not have a major impact on the orientation of the DMPE leaflets ($\approx$3°). Changes in the tilt are more intense in the leaflet exposed to the solution. This change could be ascribed to a higher mobility of the top layer or to a difference in solvation between the layers - the top layer is more accessible to possible solvent ingress at higher fields.

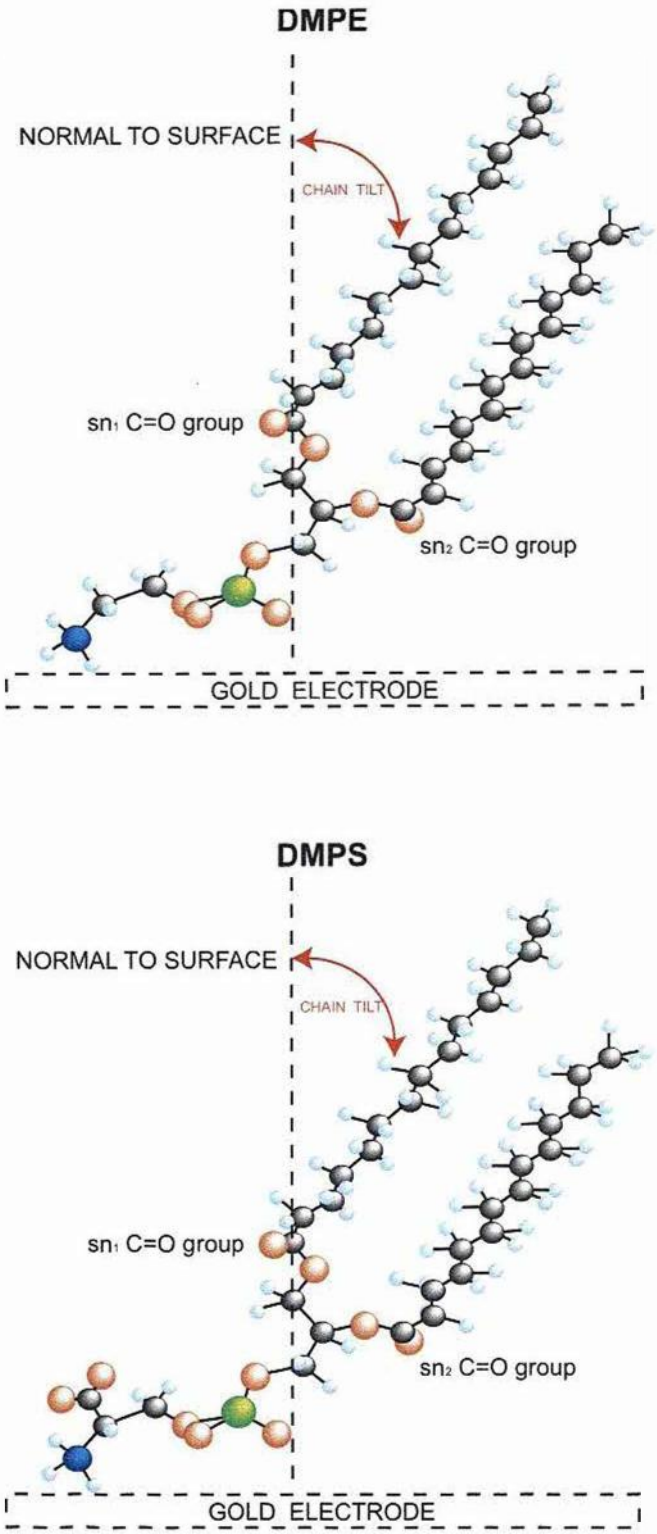

Figure 8.1: Schematic diagram of DMPE and DMPS molecules adsorbed on the electrode surface.

Electrochemical techniques gave information on the quality of the supported film and was used for the first time to study asymmetric films. Usually the first layer deposited by the LB method dominates the electrochemical properties of this asymmetric bilayer. *Ex situ* PM-IRRAS also corroborated this in the study of DMPE/DMPC asymmetric films. The adsorption of the bilayer on the electrode caused a negative shift of $E_{pzc.}$, suggesting different orientation between zwitterionic and the negatively charged headgroups. Freshly prepared bilayers were used to study the translocation of the lipids in asymmetric membranes and the results have shown no significant transmembrane migration of phospholipids to different leaflet.

8.2 Future work

Several directions are suggested to continue and complete the results of this thesis:

1. Study of deuterated DMPS films by PM-IRRAS and neutron reflectivity.

Actually, the knowledge of the increase in the hydration of the DMPS carbonyl group is a fact but the study of each leaflet by using $DMPS_D$ will provide more details on how the water is distributed within the film. Neutron reflectivity on these deuterated bilayers will provide additional information of the hydrocarbon region at different electrode potentials and an effective film thickness.

2. Study of asymmetric bilayers by PM-IRRAS.

An in-depth electrochemical study has been carried out on some asymmetric bilayers to obtain information from more realistic models. This study will be more defined by using PM-IRRAS and selectively deuterated lipids. Atomic Force Microscopy at the solid liquid interface using tapping mode will provide a complete picture of the packing arrangement and domain size of the different phospholipids at the gold electrode surface.

3. Asymmetric bilayers for the study of inserted proteins.

Previous studies mentioned in section 2 will be an advantage to understand the complexity of proteins inserted in an asymmetric bilayer. This study will provide information on the protein functions such as membrane trafficking and biochemical signalling.